



저작자표시-비영리-동일조건변경허락 2.0 대한민국

이용자는 아래의 조건을 따르는 경우에 한하여 자유롭게

- 이 저작물을 복제, 배포, 전송, 전시, 공연 및 방송할 수 있습니다.
- 이차적 저작물을 작성할 수 있습니다.

다음과 같은 조건을 따라야 합니다:



저작자표시. 귀하는 원저작자를 표시하여야 합니다.



비영리. 귀하는 이 저작물을 영리 목적으로 이용할 수 없습니다.



동일조건변경허락. 귀하가 이 저작물을 개작, 변형 또는 가공했을 경우에는, 이 저작물과 동일한 이용허락조건하에서만 배포할 수 있습니다.

- 귀하는, 이 저작물의 재이용이나 배포의 경우, 이 저작물에 적용된 이용허락조건을 명확하게 나타내어야 합니다.
- 저작권자로부터 별도의 허가를 받으면 이러한 조건들은 적용되지 않습니다.

저작권법에 따른 이용자의 권리는 위의 내용에 의하여 영향을 받지 않습니다.

이것은 [이용허락규약\(Legal Code\)](#)을 이해하기 쉽게 요약한 것입니다.

[Disclaimer](#)

공학박사학위논문

**SYNTHESIS AND APPLICATION OF
MAGNETIC COMPOSITES FOR
CONTAMINANT REMOVAL IN AQUEOUS
SOLUTIONS**

수중 오염물질 제거를 위한 자성복합체의
합성과 적용

2014년 2월

서울대학교 대학원
생태조경·지역시스템공학부

지역시스템공학전공

이 창 구

**SYNTHESIS AND APPLICATION OF
MAGNETIC COMPOSITES FOR
CONTAMINANT REMOVAL IN AQUEOUS
SOLUTIONS**

A DISSERTATION
SUBMITTED TO THE DEPARTMENT OF LANDSCAPE
ARCHITECTURE AND RURAL SYSTEMS ENGINEERING
AND THE COMMITTEE ON GRADUATE STUDIES
OF SEOUL NATIONAL UNIVERSITY
IN PARTIAL FULFILLMENT OF THE REQUIREMENTS
FOR THE DEGREE OF

DOCTOR OF PHILOSOPHY

By

CHANG-GU LEE

FEBRUARY, 2014

ABSTRACT

This thesis deals with the synthesis, characterization, and application of magnetic composites as adsorbents for selenium, chromium, arsenic, and phosphorous removal from aqueous solutions. The magnetic composites presented in this study include carbon nanotube/ iron oxide magnetic nanocomposites and magnetic alginate-layered double hydroxide composites.

Carbon nanotube/ iron oxide magnetic nanocomposites were prepared using chemical co-precipitation of iron oxide nanoparticles on surface of carbon nanotube. The synthesized magnetic nanocomposites were characterized by various analytical techniques such as SEM, TEM, nitrogen sorption, FTIR, pH_{PZC} , EDS, XRD, XPS, and VSM. The removal of the contaminants by the nanocomposites materials was verified by batch experiments and full filtration test. The adsorption properties were analyzed and quantified using kinetic and equilibrium models and thermodynamic analysis.

These analyses indicated that nano-sized iron oxide particles grown on the surface of oxidized carbon nanotube has diameters ranging from 6 to 17 nm, regularly. XRD peaks showed that iron oxide nanoparticles

were classified as a cubic iron oxide phase, i.e., maghemite and goethite. The magnetic nanocomposites have a magnetic saturation of 39.37 emu/g and a coercivity of 15.66 Oe, can be easily separated by permanent magnet.

The sorption capacities of carbon nanotube/iron oxide magnetic nanocomposites were in decreasing order: 9.55 mg/g for arsenate, 8.12 mg/g for selenite, 7.10 mg/g for arsenite, 5.93 mg/g for chromate, and 3.82 mg/g for selenate under given experimental conditions (dosage = 1 g/L, initial concentration = 10 mg/L, reaction time = 4 h, and temperature = 30°C). The results indicated that the pseudo second order model was most suitable for describing the kinetic experiments. In case of equilibrium test, the Freundlich and Redlich-Peterson isotherms were fitted well. XPS analysis revealed that selenite and selenate were reduced on the surface of magnetic nanocomposites, accompanied with iron oxidation. Sequencing extraction experiments showed that 57.8% of Cr(VI) was present in fraction of iron oxides (F3). Arsenate was removed by magnetic nanocomposites in the adsorptive filtration process, effectively.

Magnetic alginate-layered double hydroxide composites were prepared by entrapping powdered forms of both calcined Mg–Al LDHs

and magnetic iron oxide into an alginate hydrogel. The magnetic composites had a particle size of 1.5 ± 0.1 μm and showed magnetic properties under an external magnetic field. The sorption capacity of magnetic composites (2% magnetic iron oxide and 6% calcined Mg–Al LDHs) was 4.99 mg/g for phosphate and 1.61 mg/g for chromate under given conditions (adsorbent dose = 0.05 g in 30 mL solution, initial concentration = 10 mg/L, reaction time = 24 h). The magnetic composite material could be reused by magnetic separation.

Therefore, this study elucidated that the magnetic composites removed selenium, chromium, arsenic, and phosphorous from aqueous solutions, effectively. These results also demonstrate that the magnetic composites developed in this study can be applied to advanced water treatment system.

Keywords: Adsorbents, Arsenic removal, Carbon nanotubes, Chromium removal, Iron oxide nanoparticles, Layered double hydroxides, Magnetic composites, Phosphorous removal, Selenium removal

Student Number : 2008-30335

CONTENTS

ABSTRACT	i
CONTENTS	v
LIST OF TABLES	ix
LIST OF FIGURES	xiii
Chapter 1 Introduction	1
1.1. Background.....	3
1.2. Objective.....	14
Chapter 2 Literature Review	17
2.1. Nanoadsorbents and their Composites	19
2.1.1. Carbon nanotubes	19
2.1.2. Magnetic iron oxide nanoparticles	20
2.1.3. Carbon nanotube/iron oxide nanocomposites	21
2.1.4. Layered double hydroxides and magnetic polymer composites	22
2.2. Anionic Aqueous Contaminants.....	29
2.2.1. Selenium.....	29
2.2.2. Chromium.....	30
2.2.3. Arsenic.....	30
2.2.4. Phosphorus	31

Chapter 3 Synthesis and Characterization of Magnetic Composites	33
3.1. Carbon Nanotube/Iron Oxide Magnetic Nanocomposites.....	35
3.1.1. Synthesis and characterization methods.....	35
3.1.2. Surface characterization	39
3.1.3. X-ray analysis.....	48
3.1.4. Magnetic properties.....	55
3.2. Magnetic Alginate-Layered Double Hydroxide Composites ...	58
3.2.1. Synthesis and characterization methods.....	59
3.2.2. Surface characterization	65
3.2.3. X-ray analysis.....	70
3.2.4. Magnetic properties.....	77
Chapter 4 Selenate and Selenite Removal by Carbon Nanotube/ Iron Oxide Magnetic Nanocomposites.....	81
4.1. Materials and Methods	83
4.1.1. Selenium removal experiments	83
4.1.2. XPS analysis.....	84
4.1.3. Data analysis	88
4.2. Results and Discussion	92
4.2.1. Characteristics of selenium sorption	92
4.2.2. Adsorption kinetic, isotherm and thermodynamic analysis	96
4.2.3. XPS analysis for selenium adsorption.....	107
Chapter 5 Use of Carbon Nanotube/Iron Oxide Magnetic Nanocomposites for Removal of Chromium in Aqueous Solution	111
5.1. Materials and Methods	114

5.1.1. Chromate removal experiments	114
5.1.2. Sequential extraction	115
5.2. Results and Discussion	118
5.2.1. Characteristics of chromate sorption.....	118
5.2.2. Adsorption kinetic, isotherm and thermodynamic analysis ..	123
5.2.3. Chromate fractions in magnetic nanocomposites.....	134
Chapter 6 Arsenate and Arsenite Removal by Carbon Nanotube/Iron Oxide Magnetic Nanocomposites	137
6.1. Materials and Methods	139
6.1.1. Arsenic removal experiments	139
6.1.2. Adsorptive filtration experiments.....	141
6.2. Results and Discussion	144
6.2.1. Characteristics of arsenic sorption	144
6.2.2. Adsorption kinetic, isotherm and thermodynamic analysis ..	147
6.2.3. Filtration study	157
Chapter 7 Magnetic Alginate-Layered Double Hydroxide Composites for Phosphate Removal	161
7.1. Materials and Methods	164
7.1.1 Phosphate removal experiments.....	164
7.2. Results and Discussion	166
7.2.1. Characteristics of phosphate sorption	166
7.2.2. Adsorption kinetics and equilibrium isotherms.....	174

Chapter 8 Removal of Chromate from Aqueous Solution Using Magnetic Alginate-Layered Double Hydroxide Composites	183
8.1. Materials and Methods	185
8.1.1 Chromate removal experiments	185
8.2. Results and Discussion	187
8.2.1. Characteristics of chromate sorption.....	187
8.2.2. Adsorption kinetics and equilibrium isotherms.....	196
Chapter 9 General Conclusions and Recommendations.....	205
9.1 General conclusions.....	207
9.2. Recommendations	212
REFERENCES	215
NOMENCLATURE.....	235
국 문 초 록	237

LIST OF TABLES

Table 1.1 The study outline of this thesis	16
Table 2.1 Previous studies for contaminants removal from aqueous solution using carbon nanotube/iron oxide nanocomposites	25
Table 2.2 Previous studies for water treatment of the magnetic composite using magnetic separation techniques	27
Table 3.1 Physical characteristics of oxidized carbon nanotube and carbon nanotube/iron oxide magnetic nanocomposites obtained from the N ₂ adsorption–desorption data.....	45
Table 3.2 Physical characteristics of the magnetic composites obtained from the N ₂ adsorption–desorption data.....	69
Table 3.3 Chemical composition of magnetic alginate–layered double hydroxide composites (data from XRF analysis)	76
Table 4.1 Kinetic model parameters obtained from model fitting to experimental data.....	100
Table 4.2 Intra-particle diffusion model parameters obtained from model fitting to experimental data.....	102
Table 4.3 Equilibrium isotherm model parameters obtained from model	

fitting to experimental data.....	104
Table 4.4 Thermodynamic parameters for selenium adsorption to carbon nanotube/iron oxide magnetic nanocomposites.....	106
Table 4.5 Binding energies of Se 3d _{5/2} XPS spectra.....	110
Table 5.1 Scheme of sequential extraction	117
Table 5.2 Kinetic model parameters obtained from model fitting to experimental data.....	127
Table 5.3 Intra-particle diffusion model parameters obtained from model fitting to experimental data.....	129
Table 5.4 Equilibrium isotherm model parameters obtained from model fitting to experimental data.....	131
Table 5.5 Thermodynamic parameters for selenium adsorption to carbon nanotube/iron oxide magnetic nanocomposites.....	133
Table 6.1 Kinetic model parameters obtained from model fitting to experimental data.....	150
Table 6.2 Intra-particle diffusion model parameters obtained from model fitting to experimental data.....	152
Table 6.3 Equilibrium isotherm model parameters obtained from model fitting to experimental data.....	154

Table 6.4 Thermodynamic parameters for selenium adsorption to carbon nanotube/iron oxide magnetic nanocomposites.....	156
Table 7.1 Phosphate removal by the magnetic composites at different initial solution pH (adsorbent dose = 0.05 g in 30 ml solution; initial phosphate concentration = 10 mg P /l)	173
Table 7.2 Kinetic model parameters obtained from model fitting to phosphate experimental data	177
Table 7.3 Intra-particle diffusion model parameters obtained from model fitting to phosphate experimental data.....	179
Table 7.4 Equilibrium isotherm model parameters obtained from model fitting to phosphate experimental data	181
Table 8.1 Kinetic model parameters obtained from model fitting to phosphate experimental data	199
Table 8.2 Intra-particle diffusion model parameters obtained from model fitting to phosphate experimental data.....	201
Table 8.3 Equilibrium isotherm model parameters obtained from model fitting to phosphate experimental data	203

LIST OF FIGURES

Figure 1.1 Changes of (a) international (WHO) and (b) domestic (MOE) water quality standards for related contaminants.....	10
Figure 1.2 Schematic for surface area of nanoparticles (modified from Feldmann and Goesmann (2010)).	11
Figure 1.3 Application fields of nanotechnology (modified from NNI (2008)).	12
Figure 1.4 Application groups of nanomaterials for water purification (modified from Ambashta and Sillanpaa (2010)).	13
Figure 3.1 Schematic illustration of the synthesis of the carbon nanotube/iron oxide magnetic nanocomposites.....	37
Figure 3.2 Field emission scanning electron micrographs of (a) oxidized carbon nanotube and (b) carbon nanotube/iron oxide magnetic nanocomposites (x 50.00K).....	42
Figure 3.3 Transmission electron micrographs of (a, b) oxidized carbon nanotube and (c, d) carbon nanotube/iron oxide magnetic nanocomposites.	43
Figure 3.4 Nitrogen sorption and pore size distribution methods: (a) N ₂ adsorption-desorption curves; (b) BET analysis; (c) BJH methods; (d)	

HK methods.....	44
Figure 3.5 FTIR spectra of oxidized carbon noanotube and carbon nanotube/iron oxide magnetic nanocomposites.....	46
Figure 3.6 Potentiometric titration curves for carbon nanotube/iron oxide magnetic nanocomposites.....	47
Figure 3.7 Color mapping of oxidized carbon nanotube: (a) SEM image of mapping point; (b) carbon (C) map; (c) oxygen (O) map.....	50
Figure 3.8 Color mapping of magnetic nanocomposites: (a) SEM image of mapping point; (b) carbon (C) map; (c) oxygen (O) map; (d) iron (Fe) map.....	51
Figure 3.9 Energy dispersive X-ray spectrums of (a) oxidized carbon nanotube and (b) carbon nanotube/iron oxide magnetic nanocomposites.	52
Figure 3.10 XRD patterns of oxidized carbon noanotube and carbon nanotube/iron oxide magnetic nanocomposites (C= carbon, G= goethite, M= maghemite).	53
Figure 3.11 XPS spectra of carbon nanotube/iron oxide magnetic nanocomposites: (a) wide scan; (b) high-resolution scan of Fe2p region.	54
Figure 3.12 Digital snapshot images of carbon nanotube/iron oxide magnetic nanocomposites under external permanent magnet condition.	56

Figure 3.13 Magnetic hysteresis curves for (a) magnetic iron oxide nanoparticles and (b) carbon nanotube/iron oxide magnetic nanocomposites.	57
Figure 3.14 Powder form of (a) magnetic iron oxide and (b) layered double hydroxides used in the synthesis of magnetic composites.	62
Figure 3.15 Schematic illustration of the synthesis of the magnetic alginate-layered double hydroxide composites.	63
Figure 3.16 Digital images of (a) magnetic alginate-layered double hydroxide composites and (b) size distribution.	66
Figure 3.17 SEM images of magnetic alginate-layered double hydroxide composites: (a) surface area; (b) cross section area.	67
Figure 3.18 Nitrogen sorption and pore size distributions of magnetic composites: (a) N ₂ adsorption-desorption curves; (b) BET analysis; (c) BJH methods; (d) HK methods.	68
Figure 3.19 Color mapping of magnetic composites at surface area: (a) carbon (C) map; (b) iron (Fe) map; (c) magnesium (Mg) map; (d) aluminum (Al) map.	72
Figure 3.20 Color mapping of magnetic composites at cross section area: (a) carbon (C) map; (b) iron (Fe) map; (c) magnesium (Mg) map; (d) aluminum (Al) map.	73
Figure 3.21 Energy dispersive X-ray spectrums of magnetic alginate-layered double hydroxide composites.	74

Figure 3.22 XRD patterns of magnetic iron oxide and layered double hydroxides used in the synthesis of magnetic composites.	75
Figure 3.23 Digital image of magnetic alginate-layered double hydroxide composites.	78
Figure 3.24 Magnetic hysteresis curves for magnetic alginate-layered double hydroxide composites.	79
Figure 4.1 Schematic diagram of Einstein relationship (modified from Lee and Boo (1990)).	87
Figure 4.2 Selenium adsorption to magnetic nanocomposites: (a) effect of reaction time for Se(IV); (b) effect of reaction time for Se(VI); (c) effect of initial selenium concentration; (d) effect of solution pH.	95
Figure 4.3 Kinetic model fits for selenate and selenite removal in the magnetic nanocomposites at various temperatures: (a) 15°C; (b) 30°C; (c) 45°C.	99
Figure 4.4 Intra-particle diffusion model for selenate and selenite removal in the magnetic nanocomposites.	101
Figure 4.5 Equilibrium isotherm model fits for selenate and selenite removal in the magnetic nanocomposites.	103
Figure 4.6 Thermodynamic analyses for selenate and selenite removal in the magnetic nanocomposites.	105
Figure 4.7 XPS spectra of selenium adsorbed on carbon nanotube/iron	

oxide magnetic nanocomposites surface: (a) Se 3d _{5/2} spectra; (b) Fe 2p _{3/2} spectra.	109
Figure 5.1 Cr(VI) adsorption to magnetic nanocomposites: (a) effect of reaction time; (b) effect of initial Cr(VI) concentration; (c) effect of reaction temperature; (d) effect of solution pH.	121
Figure 5.2 XPS spectra of Cr(VI) adsorbed on carbon nanotube/iron oxide magnetic nanocomposites surface.	122
Figure 5.3 Kinetic model fits for chromate removal in the magnetic nanocomposites at various temperatures: (a) 15°C; (b) 30°C; (c) 45°C.	126
Figure 5.4 Intra-particle diffusion model for chromate removal in the magnetic nanocomposites, iron oxide nanoparticles, and oxidized carbon nanotubes.	128
Figure 5.5 Equilibrium isotherm model fits for chromate removal in the magnetic nanocomposites.	130
Figure 5.6 Thermodynamic analyses for chromate removal in the magnetic nanocomposites.	132
Figure 5.7 Cr(VI) distribution on the carbon nanotube/iron oxide magnetic nanocomposites by sequential extraction.	135
Figure 6.1 Digital image of filter type of carbon nanotube/iron oxide magnetic nanocomposites.	142

Figure 6.2 Schematic diagram of full filtraion experiment.	143
Figure 6.3 Arsenic adsorption to magnetic nanocomposites: (a) effect of reaction time for As(III); (b) effect of reaction time for As(V); (c) effect of initial selenium concentration; (d) effect of solution pH.	146
Figure 6.4 Kinetic model fits for arsenate and arsenite removal in the magnetic nanocomposites at various temperatures: (a) 15°C; (b) 30°C; (c) 45°C.	149
Figure 6.5 Intra-particle diffusion model for arsenate and arsenite removal in the magnetic nanocomposites.	151
Figure 6.6 Equilibrium isotherm model fits for arsenate and arsenite removal in the magnetic nanocomposites.	153
Figure 6.7 Thermodynamic analyses for arsenate and arsenite removal in the magnetic nanocomposites.	155
Figure 6.8 SEM image of filter type magnetic nanocomposites: (a) aerial view; (b) cross section view.	158
Figure 6.9 Color mapping of filter type magnetic nanocomposites: (a) SEM image of mapping point; (b) carbon (C) and iron (Fe) map; (c) carbon map; (d) iron map.	159
Figure 6.10 As(V) removal by filter type of carbon nanotube/iron oxide magnetic nanocomposites: (a) different pressure (As(V) concentration = 10ppm); (b) different initial As(V) concentration (pressure = 30 psi).	160

Figure 7.1 Phosphate removal at various contents of magnetic iron oxide-calcined Mg-Al LDHs in the magnetic composites (adsorbent dose = 0.05 g in 30 mL solution; initial phosphate concentration = 10 mgP/L)	169
Figure 7.2 Phosphate removal by the magnetic composites as a function of reaction time (adsorbent dose = 0.05 g in 30 mL solution; initial phosphate concentration = 10 mg/l).	170
Figure 7.3 Phosphate removal by the magnetic composites as a function of initial phosphate concentration (adsorbent dose = 0.05 g in 30 mL solution; reaction time = 24 h).....	171
Figure 7.4 Phosphate removal upon repeated use of the magnetic composites (adsorbent dose = 0.05 g in 30 mL solution; initial phosphate concentration = 10 mgP/l).	172
Figure 7.5 Kinetic model fits for phosphate removal in the magnetic composites.	176
Figure 7.6 Intra-particle diffusion model for phosphate removal in the magnetic composites.	178
Figure 7.7 Equilibrium isotherm model fits for phosphate removal in the magnetic composites.....	180
Figure 8.1 Chromate removal at various contents of calcined Mg-Al LDHs-magnetic iron oxide in the magnetic composites (adsorbent dose = 0.05 g in 30 mL solution; initial Cr(VI) concentration = 10 mg/L).	191

Figure 8.2 Chromate removal upon repeated use of the magnetic composites (adsorbent dose = 0.05 g; initial Cr(VI) concentration = 10 mg/L).	192
Figure 8.3 Chromate removal by the magnetic composites as a function of reaction time (adsorbent dose = 0.05 g in 30 mL solution; initial Cr(VI) concentration = 10 mg/L).	193
Figure 8.4 Chromate removal by the magnetic composites as a function of initial Cr(VI) concentration (adsorbent dose = 0.05 g in 30 mL solution; reaction time = 24 h).....	194
Figure 8.5 Effect of initial solution pH on chromate removal by the magnetic composites (adsorbent dose = 0.05 g; initial Cr(VI) concentration = 10 mg/L). The number in the parenthesis is final (equilibrium) pH.	195
Figure 8.6 Kinetic model fits for chromate removal in the magnetic composites.	198
Figure 8.7 Intra-particle diffusion model for chromate removal in the magnetic composites.	200
Figure 8.8 Equilibrium isotherm model fits for phosphate removal in the magnetic composites.....	202

Chapter 1 Introduction

1.1. Background

Indiscriminate development in recent decades has led to a rapid urbanization and an uncontrolled population growth. As a result, the world has encountered a variety of pressing environmental challenges such as climate change/global warming (Hansen, 2005), excessive generation of solid waste (Lo *et al.*, 2010), and water pollution (Kurniawan and Lo, 2009; Sillanpaa *et al.*, 2011). To address those global water quality problems, pioneering approaches are required.

Clean water is an important strategic resource to be protected as a basis for economic prosperity and a healthy society, water quality is one of the important parameters indicating the state of quality of life (Kurniawan *et al.*, 2012). In order to solve the problem of environmental pollution that changes according to the times, environmental remediation technology level that time requests is required. Looking at the quality standards of each country, the target quality criterion, and also have increased, there is a tendency to decrease the allowable concentration is necessary to develop technology that can respond appropriately to this.

With the development of technology, new contaminants that were not known to the prior art is detected or found, resulted in an increase of the new water quality criterion. Subsequent to the existing nine water quality standards by 2006, Korean Ministry of Environment (MOE) issues the additional eight water quality standards by 2009, and plans to finally expand water quality standards up to thirty substances by 2015 (An *et al.*, 2007). The allowed limits for well-known contaminants were revised periodically. The recommended maximum

value for arsenic in drinking water, as per the World Health Organization (WHO) International standards, has been reduced from 200 ppb to 10 ppb, through a number of revisions during the last 50 years. During the same period, the allowed concentration for lead in drinking water was reduced from 100 ppb to 10 ppb (Pradeep and Anshup, 2009). Changes of international and domestic water quality standards for related contaminants are shown in Figure 1.1.

Conventional water treatment plants could be completely removed the contaminants present in raw water following a sequence of steps including aggregation, filtration and disinfection. But unfortunately in recent years, the results of industrialization and abuse of pesticides/fertilizers are discharged number of toxic contaminants into water bodies. Presence of contaminants such as heavy metals (Muller *et al.*, 1995; Kruawal *et al.*, 2005) and/or nutrients (Wang *et al.*, 2005; Xiong *et al.*, 2008) in the source water leaves a detrimental impact on water treatment. The treatment efficiency is drastically reduced and the contaminant flows out because conventional water treatment plants were not designed to handle of them. Therefore, additional post-processing step is needed.

On the other hand, advanced membrane filtration techniques such as nanofiltration (NF) / reverse osmosis (RO) exhibit superior performance removal of chemical contaminants as compared with conventional water treatment systems. But, the use of NF / RO filter is limited owing to high operating and maintenance costs (Pianta *et al.*, 2000). Moreover, the biological contaminants are cause of membrane fouling as a result the removal efficiency drastically decreased (Meng

et al., 2009). Thus, the membrane filtration technique is needed a pre-treatment barrier to remove these contaminants.

As previously discussed the water treatment plants have to accept the additional needs for complex chemical decontamination of anthropogenic origin. The centralized treatment system may not be sufficient under these environmental conditions. Therefore, the development of technology such as point of use system is required. Point-of-use (POU) devices are treatment systems installed on single or multiple taps and are often combined with other treatment processes to provide a more complete water treatment. They are usually used to improve the aesthetic qualities of drinking water and to remove chemicals. POU processes employed include ion-exchange resins or adsorption filters. Various types of ion-exchange resins are used in softening hard water (Greenleaf *et al.*, 2006; Coca *et al.*, 2010). Activated carbon filters are generally effective in removing chemical contaminants and are often used to improve smell and taste (Da Silva *et al.*, 2012; Flanagan *et al.*, 2013). Filters containing activated aluminum oxide are used to remove heavy metals from water (Fox, 1989; Thomson *et al.*, 2003). These are commonly used in rural areas (Environment and Workplace Health Report Canada, 2009).

Recognition of the importance of the environment increases, the demand for innovative technology that cost-effective and can minimize the harmful substances in water environments has increases significantly. These ideas are well-organized in the report by the Royal Society of Chemistry (RSC, 2007). The report recommends the way to minimize the generation of sludge or secondary waste after treatment

by reducing consumption of chemicals. As well as reducing byproducts, energy consumption and treatment costs can be reduced with satisfying the requirement set by legislation. Therefore, nanotechnology suggest as sustainable and environmental friendly alternative to overcome the limitations of prior art water treatment (Kurniawan *et al.*, 2012).

According to National Nanotechnology Initiative (NNI), the definition of nanotechnology is the understanding and control of matter at dimensions between approximately 1 and 100 nm, where unique phenomena enable novel applications. Excellent properties of nanomaterials are the large surface area corresponding to the size of the particles. Feldmann and Goesmann (2010) simply described this concept as shown in Figure 1.2. A cube with edges 1 cm in length divides into cubes with edges 10 nm in length, the surface area increases 10^6 fold while the volumes remain the same. Also, increasing number of surface atoms leads to drastic increase in chemical reactivity of the nanoparticles. Recently, superior features of these products are used in various fields (Figure 1.3).

Due to the nano-sized, nanoadsorbents can be effectively removes contaminants from water. The molecular level of their size leads to maximize the amount of adsorption per unit mass but minimize the sludge generation. According to the literature, as particle size of magnetite is decreased from 300 nm to 12 nm the sorption capacity for arsenic increase nearly 200 times, this is more than expected from simple consideration of surface area (Mayo *et al.*, 2007). Nanoadsorbents are mainly divided into some groups based in their application for water purification as shown in Figure 1.4. Among them,

this study covers meso-structure carbon material of carbon nanotubes, magnetic iron oxide nanoparticles, and layered double hydroxides as hydrated metal oxide.

Carbon nanotubes (CNTs) are a hollow single or multiple layers of carbon material. They are used to remove organic and inorganic contaminants as excellent adsorbents from aqueous solutions. (Rao *et al.*, 2007; Upadhyayula *et al.*, 2009). Unlike many adsorbents, CNTs has a fibrous shape with high aspect ratio, large accessible external surface area, and well developed mesopores. Due to a large surface area, CNTs used as support of metallic oxides have still been reported (Gupta *et al.*, 2011; Velickovic *et al.*, 2012; Chen *et al.*, 2013). Modification of CNTs by the iron oxide nanoparticles can enhance the removal capacity of anionic contaminants such as chromate (47.98 mg/g) and arsenite (23.47 mg/g). Iron oxide nanoparticles are iron oxide particles with diameters between about 1 and 100 nanometers. The two main forms are magnetite (Fe_3O_4) and its oxidized form maghemite ($\gamma\text{-Fe}_2\text{O}_3$). They appeared superparamagnetic properties (Khajeh *et al.*, 2013) and effectively separated from water using magnetic assistance (Ambashta and Silanpaa, 2010). Iron oxide nanoparticles have been used in water treatment as well as high-density information storage and electronic devices (Sun *et al.*, 2000; Wan *et al.*, 2007; Yoon *et al.*, 2014). Layered double hydroxides (LDHs) are a class of nanostructured anionic clays. They consist of positively charged brucite-like sheets that are balanced by the intercalation of anions in the hydrated interlayer regions (Goh *et al.*, 2008). LDHs have high surface areas, large anion exchange capacities, and good thermal properties (Cavani *et al.*, 1991). Several

researchers have investigated the removal of various contaminants using LDHs.

These nanoadsorbents has highly reactive and excellent adsorption capacity, but was difficult to separation from water due to their nano size. Magnetic separation is an innovative technology and has been applied by several researchers to water treatment and purification (Yavuz *et al.*, 2009). Individual magnetic nanoadsorbents can be separated by high-gradient magnetic separation (HGMS) technique (Mayo *et al.*, 2007). However, this technique requires large energy consumption. For easy magnetic separation, magnetic particles such as magnetite (Fe_3O_4) and maghemite ($\gamma\text{-Fe}_2\text{O}_3$) are immobilized into polymers such as alginate, chitosan, polyvinyl alcohol, and gellan gum to form magnetic beads or composites (Yavuz *et al.*, 2009). These magnetic composites can be easily separated from the aqueous solution using permanent magnet. In addition, functional materials are added into the beads/composites to remove target contaminants. Even though extensive studies using LDHs for anionic contaminants removal, but the best of our knowledge, so far there is no applied to a magnetic composite as functional materials. Decorated iron oxide nanoparticles on supporting materials can maintain high reactivity and improve separation efficiency. To our knowledge, however, studies related to the removal of anionic contaminants by iron oxide nanoparticles doped on carbon nanotube are scarce, and research for the removal of selenium is none. As well, there are no experimental studies that were used as adsorptive filter type.

In this study, provides a simple and inexpensive method for

synthesis of magnetic composites as adsorbents, and presents precisely physicochemical properties of the composites using various analytical methods. Also, this research provides information about removal characteristics of various anionic contaminants, and presents applicability for water decontamination.

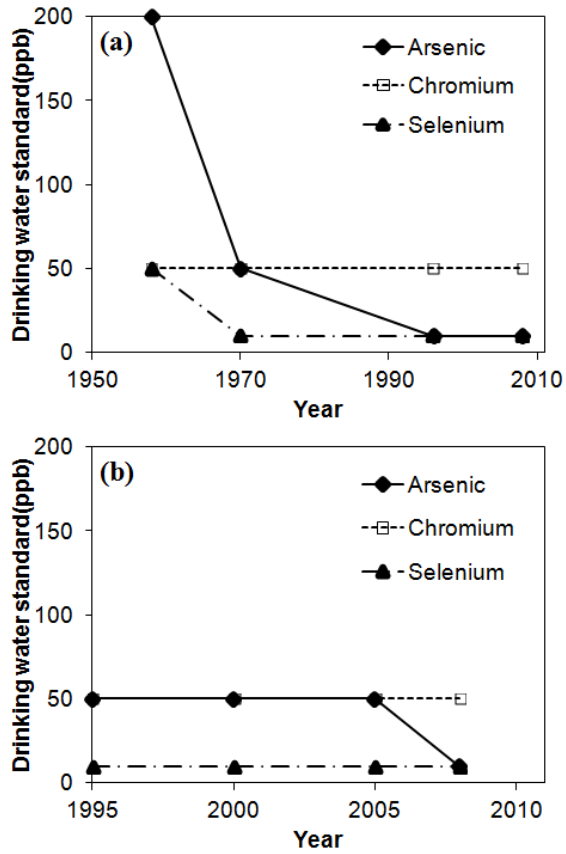
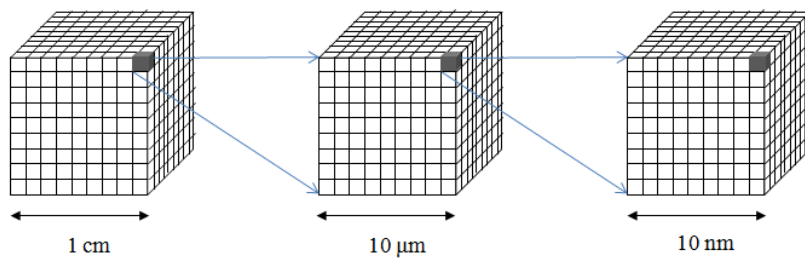


Figure 1.1 Changes of (a) international (WHO) and (b) domestic (MOE) water quality standards for related contaminants.



Edge length of cubes	Number of cubes	Volume of cubes	Surface area of cubes
1 cm	1	1 cm ³	0.0006 m ²
10 μm	10 ⁹	1 cm ³	0.6 m ²
10 nm	10 ¹⁸	1 cm ³	600 m ²

Figure 1.2 Schematic for surface area of nanoparticles (modified from Feldmann and Goesmann (2010)).

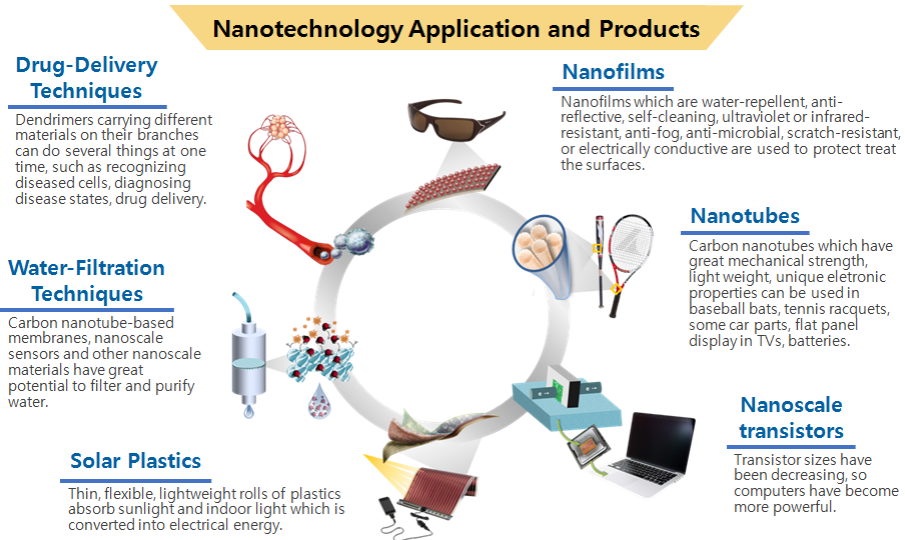


Figure 1.3 Application fields of nanotechnology (modified from NNI (2008)).

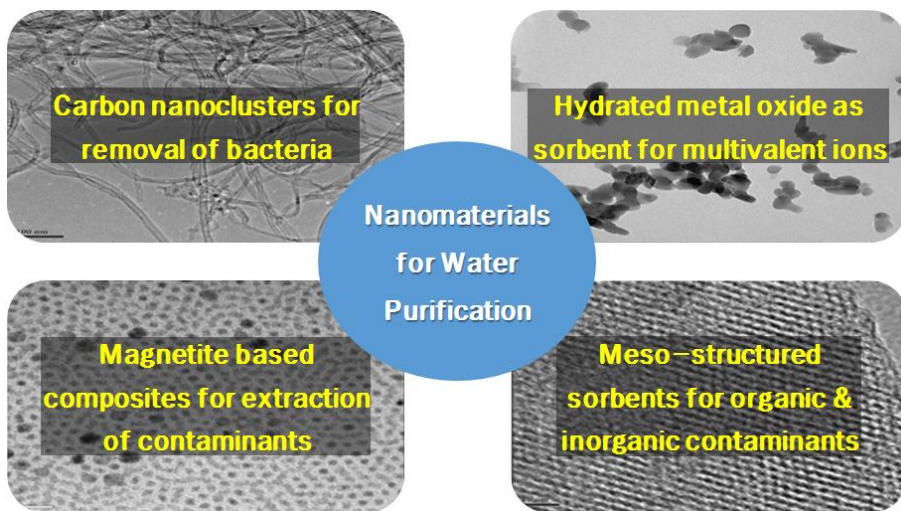


Figure 1.4 Application groups of nanomaterials for water purification (modified from Ambashta and Sillanpaa (2010)).

1.2. Objective

The objective of this thesis is to the synthesis of magnetic composites and their application as adsorbents for contaminant in aqueous solutions. The specific objectives of the dissertation are to:

- Synthesize and characterize the magnetic composites. Carbon nanotube / iron oxide magnetic nano composites were prepared using co-precipitation and oxidation methods. Magnetic alginate – layered double hydroxide composites were prepared by entrapping method after co-precipitation. The magnetic composites were analyzed by surface properties, crystalline structures, and magnetic properties (Chapter 3).

- Investigate the selenium removal using carbon nanotube/iron oxide magnetic nanocomposites. The effects of reaction time, initial concentration, solution pH, and temperature were investigated with model analysis. Oxidation state of selenium was also analyzed (Chapter 4).

- Evaluate the sorption capacity of chromium by carbon nanotube/iron oxide magnetic nanocomposites. Batch experiments were performed at different reaction time, initial concentration, solution pH, and temperature. Distribution of chromium on the magnetic nanocomposites was investigated. (Chapter 5).

- Investigate the arsenic removal using carbon nanotube/iron oxide magnetic nanocomposites. Batch experiments and adsorption model analysis were conducted. Adsorptive filtration experiments were conducted using stirred ultrafiltration cell (Chapter 6).

- Examine the removal of phosphorous using magnetic alginate – layered double hydroxide composites. Batch experiments were performed at various contents, reaction time, initial concentration, and solution pH. Reuse test was also investigated with magnetic separation. (Chapter 7).

- Evaluate the sorption capacity of chromium by magnetic alginate – layered double hydroxide composites. Batch experiments and adsorption model analysis were conducted. Reuse test was also investigated with magnetic separation. (Chapter 8).

The study outline of this thesis is shown in Table 1.1.

Table 1.1 The study outline of this thesis

Adsorbents	Carbon Nanotube / Iron Oxide Magnetic Nanocomposites	Magnetic Alginate / Layered Double Hydroxide Composites
Synthetic methods	Oxidation / Co-precipitation	Co-precipitation / Entrapment
Characterizations	SEM, TEM, N ₂ sorption, FTIR, pH _{PZC} , EDS, XRD, XPS, VSM	SEM, N ₂ sorption, EDS, XRD, XRF, VSM
Contaminants	Selenium Chromium Arsenic	Chromium Phosphorous
Conditions	Reaction time, Initial concentration, Solution pH, (Temperature)	
Data analysis	Kinetic adsorption model, Kinetic diffusion model, Isotherm model, (Thermodynamic analysis)	
Specific research	Surface chemistry analysis Sequential extraction	Adsorptive filtration experiments Contents / Reuse

Chapter 2 Literature Review

2.1. Nanoadsorbents and their Composites

Nanoscale solid materials have become very important because of their special properties, and the nanomaterials field has gained increasing attention from scientists and engineers (Upadhyayula *et al.*, 2009; Sharma *et al.*, 2009; Pradeep and Anshup, 2009; Ambashta and Sillanpaa, 2010; Kurniawan *et al.*, 2012; Khajeh *et al.*, 2013). Due to the most of the atoms are on the surface of the nanomaterials, they have high chemical activity and sorption capacity to many contaminants.

2.1.1. Carbon nanotubes

Carbon nanotubes (CNTs) were first discovered by Iijima in 1991 (Iijima, 1991). CNTs have been applied to various fields due to their excellent mechanical, thermal, and electrical properties. Carbon nanotubes (CNTs) include single-walled carbon nanotubes (SWCNTs) and multiwalled carbon nanotubes (MWCNTs) depending on the number of layers. The application of CNTs as adsorbent to remove organic and inorganic pollutants has been studied (Tan *et al.*, 2008; Li *et al.*, 2002; Chen and Wang, 2006). Carbon nanotubes (CNTs) have been chemically functionalized with various oxygen-containing surface groups. Functionalized CNTs have a superior adsorption capacity toward CrO_4^{2-} , Zn^{2+} , and BTEX (Xu *et al.*, 2011; Lu and Chiu, 2008; Lu *et al.*, 2008). Several studies have been carried out on the adsorption of radionuclides. Chen *et al.* (2009) examined the interaction between Eu(III) and a multiwall carbon nanotube (MWCNTs)/iron oxide magnetic composite in the absence and presence of poly(acrylic acid)

(PAA). Chen *et al.* (2008) were conducted to investigate the surface charge characteristics of oxidized MWCNTs and the surface complexation interactions between Sr(II)/Eu(III) and oxidized MWCNTs. CNTs have shown high adsorption efficiency for various organic contaminants such as dioxin, benzene, and 1,2-dichlorobenzene (Long and Yang, 2001; Gauden *et al.*, 2006; Peng *et al.*, 2003). Metal or nonmetal doping on CNTs surface can change the adsorption properties. Wang *et al.* (2007) removed Pb(II) by MnO₂/CNTs. Gupta *et al.* (2011) were used alumina-coated multi-wall carbon nanotube as adsorbent for removal of lead ions from aqueous solutions.

2.1.2. Magnetic iron oxide nanoparticles

The synthesis and application of magnetic nanoparticles to water and wastewater treatment have attracted considerable attention in recent years (Li *et al.*, 2011). Magnetic nanoparticles can be used as adsorbents for water and wastewater treatment and separated from aqueous medium through magnetic separation (Sayin *et al.*, 2013; Ambashta and Sillanpää, 2010; Tang and Lo, 2013), and among the various magnetic nanoparticles, maghemite (γ -Fe₂O₃) and magnetite (Fe₃O₄) are the iron oxides observed to be useful (Wu *et al.*, 2008). Several researchers applied magnetic iron oxide nanoparticles to remove contaminants from aqueous solutions (Chan *et al.*, 2012; Senel *et al.*, 2008). Pan *et al.* (2012) removed mercury from an aqueous solution by mercapto functionalized magnetite nanoparticles. Badruddoza *et al.* (2011) fabricated magnetite nanoparticles functionalized with carboxymethyl- β -cyclodextrin to remove copper

ions. Wang et al. (2011) investigated the sorption kinetics and mechanism of copper to nanoscale magnetite. Iram et al. (2010) removed neutral red dye from an aqueous solution using magnetite hollow nanospheres. Chowdhury and Yanful (2010) showed the limitation of arsenic and chromium uptake by the nano-size magnetite-maghemite mixture in the presence of a competing anion such as phosphate.

2.1.3. Carbon nanotube/iron oxide nanocomposites

Because of their relatively large surface area, CNTs can also be used as supports for iron oxide nanoparticles. Unlike many CNTs based materials, CNTs-iron oxide magnetic nanocomposites can be used to adsorb contaminants from aqueous solution and after the adsorption is carried out, the adsorbent can be separated from the medium by a magnetic separation (Dong *et al.*, 2009; Ntim et al., 2011; Chen *et al.*, 2013). Several researchers applied CNTs-iron oxide magnetic nanocomposites to remove dye from aqueous solutions (Qu *et al.*, 2008; Gong *et al.*, 2009; Ai *et al.*, 2011). Zhu *et al.* (2010) removed methyl orange by magnetic chitosan enwrapping nanosized γ -Fe₂O₃ and multi-walled carbon nanotubes. Chang *et al.* (2011) synthesized magnetic soluble starch-functionalized carbon nanotubes to application for the adsorption of the dyes. CNTs-iron oxide magnetic nanocomposites can be also used as adsorbents for removal of heavy metals (Chen et al., 2009; Hu et al., 2010; Hu et al., 2011). Wang *et al.* (2011) removed cobalt from aqueous solution by magnetic multiwalled carbon nanotube/iron oxide composites. Gupta *et al.* (2011) showed

that the adsorptions of Cr(III) on the MWCNT/nano-iron oxide composites was strongly dependent on contact time, agitation speed and pH, in the batch mode. Ma *et al.* (2013) reported a one-pot method to synthesize magnetic iron oxide/CNTs composites based on as-prepared CNTs for use as adsorbents for arsenic removal. Else, Wei *et al.* (2012) demonstrated that magnetic MWCNTs could offer a new type of adsorbent for removal of bilirubin. Yang *et al.* (2013) showed that the adsorption of naphthalene and its derivatives on magnetic graphene and MWCNTs. Wang *et al.* (2013) removed oil droplets from contaminated water using magnetic carbon nanotubes. Previous studies for contaminants removal from aqueous solution using carbon nanotube/iron oxide nanocomposites were summarized in table 2.1.

2.1.4. Layered double hydroxides and magnetic polymer composites

Layered double hydroxides (LDHs) are a class of nanostructured anionic clays. They consist of positively charged brucite-like sheets that are balanced by the intercalation of anions in the hydrated interlayer regions (Goh *et al.*, 2008). LDHs have high surface areas, large anion exchange capacities, and good thermal properties (Cavani *et al.*, 1991). Several researchers have investigated the adsorption and removal of Cr(VI) using various LDHs (Prasanna *et al.*, 2006; Tzou *et al.*, 2007; Prasanna and Kamath, 2008; Goh and Lim, 2010). They have observed the removal of Cr(VI) using calcined Mg-Al LDHs through an anion exchange reaction between a chromate ion and a hydroxyl ion (Rhee *et al.*, 1997), better performance of chloride-LDHs as adsorbents than

calcined carbonate LDHs in Cr(VI) removal (Carriazo *et al.*, 2007), Cr(VI) removal by Mg-Al LDHs nanoparticles (Goh *et al.*, 2010), and the influence of textural and structural properties of calcined Mg-Al and Mg-Zn-Al LDHs on sorption of Cr(VI) (Dudek *et al.*, 2012). Researchers have examined the removal of phosphate using various LDHs, including the ion exchange between chloride and phosphate into zinc-aluminium (Zn-Al) LDHs (Badreddine *et al.*, 1999), phosphate removal by iron-based LDHs (Seida and Nakano, 2002) and characterization of magnesium-manganese (Mg-Mn) LDHs for the removal of phosphate from seawater (Chitrakar *et al.*, 2005). They also investigated the comparison of various calcined LDHs on phosphate removal (Das *et al.*, 2006) and enhancement of the phosphate removal capacity of Zn-Al LDHs through the incorporation of zirconium (Koilaraj and Kannan, 2009).

Magnetic separation is an innovative technology and has been applied by several researchers to water treatment and purification (Yavuz *et al.*, 2009). For magnetic separation, magnetic particles such as magnetite (Fe_3O_4) and maghemite ($\gamma\text{-Fe}_2\text{O}_3$) are immobilized into polymers such as alginate, chitosan, polyvinyl alcohol, and gellan gum to form magnetic beads or composites (Yavuz *et al.*, 2009). In addition, functional materials are added into the beads/composites to remove target contaminants. These previous studies were presented in Table 2.2. Researchers conducted a removal experiment of various heavy metal ions in aqueous solution. Bayramoglu and Arica (2007) were using amino group functionalized magnetic beads for removal of Hg(II). Uzen *et al.* (2009) were using magnetic beads containing triazole

chelating groups for removal of various divalent heavy metal ions like Hg(II), Pb(II), Cu(II), Cd(II), and Zn(II). In addition to magnetic separation function, magnetite was used to remove Pb(II), Ni(II), La(III), and As(V) as a functional material (Wakui *et al.*, 2005; Tran *et al.*, 2010; Wu *et al.*, 2011; Jiang *et al.*, 2012). Along these lines, recent studies have focused on recovery of Cr(VI) from wastewater using magnetic beads containing *Rhizopus cohnii* (industrial fungus) (Li *et al.*, 2008), adsorption of Cr(III) to magnetic gellan gum beads (Wang *et al.*, 2009), separation of Cr(VI) from an aqueous solution using magnetic chitosan beads modified with diethylenetriamine (Li *et al.*, 2011), photocatalytic reduction of Cr(VI) to Cr(III) using maghemite-containing magnetic beads (Idris *et al.*, 2011, Idris *et al.*, 2012b), and removal of low concentration of Cr(VI) using magnetic chitosan beads coated by MnFe₂O₄ nanoparticles (Xiao *et al.*, 2013). Activated carbon has been widely used as a functional material for the removal of dye from water using magnetic composites (Rocher *et al.*, 2008; Luo and Zhang, 2009; Rocher *et al.*, 2010; Ai *et al.*, 2011). Also, Zhang *et al.* (2013) was synthesized of BSA cross-linked magnetic composite for adsorption of antibiotics and Chen *et al.* (2013) was reported highly selective oil-absorbent materials coated with a polystyrene layer based magnetic nanoparticles.

Table 2.1 Previous studies for contaminants removal from aqueous solution using carbon nanotube/iron oxide nanocomposites

	Contaminants	Efficiency (mg/g)	Iron-type	Reference
Heavy metal	Cr(VI)	47.98	Mn	Chen <i>et al.</i> , 2013
	As(III)	8.13	Mh/Mn	Ma <i>et al.</i> , 2013
	As(V)	9.74		
	Pb(II)	75.02	Mn	Ji <i>et al.</i> , 2012
	As(V)	23.47	G/H	Velickovic <i>et al.</i> , 2012
	Cr(III)	–	Mh/Mn	Gupta <i>et al.</i> , 2011
	Cu(II)	12.87	Mh/Mn/G	Hu J. <i>et al.</i> , 2011b
	Pb(II)	31.25	Mh/Mn/G	Hu J. <i>et al.</i> , 2011a
	Cu(II)	8.92		
	Eu(III)	–	Mh/Mn/G	Lu <i>et al.</i> , 2011
	As(III)	1.72	Mh/Mn/G/H	Ntim and Mitra, 2011
	As(V)	0.19		
	Co(II)	8.84	Mh/Mn/G	Wang <i>et al.</i> , 2011
	Pb(II)	12.29	Mh/Mn/G	Hu J. <i>et al.</i> , 2010
	Eu(III)	–	Mh/Mn/G	Chen <i>et al.</i> , 2009b
	Ni(II)	9.18	Mh/Mn/G	Chen <i>et al.</i> , 2009a
	Sr(II)	–		
	Cu(II)	–	Mn	Dong <i>et al.</i> , 2009
	Pb(II)	105.67	Mh/Mn/G	Peng <i>et al.</i> , 2005
Cu(II)	45.12			
Dye	Methylene blue	48.06	Mn	Ai <i>et al.</i> , 2011
	Methyl orange	135.8	Mn	Chang <i>et al.</i> , 2011
	Methylene blue	94.1		
	Methyl orange	66.09	Mh	Zhu <i>et al.</i> , 2010
	Methylene blue	15.74	Mh/Mn/H	Gong <i>et al.</i> , 2009
	Neutral red	20.33		
	Brilliant cresyl blue	23.55		

	Methylene blue	42.3		
	Neutral red	77.5	Mh	Qu <i>et al.</i> , 2008
	Diesel	6600	Mn	Wang <i>et al.</i> , 2013
	Naphthalene	337	Mn	Yang <i>et al.</i> , 2013
	Tetrabromobisphenol A	33.72	Mn	Ji <i>et al.</i> , 2012
	Bilirubin	263.16	Mh/Mn/H	Wei <i>et al.</i> , 2012
Organics	Polychlorinated biphenyls	–	Mn	Zeng <i>et al.</i> , 2012
	17 α -methyltestosterone	122.81	Mn	Hu X. <i>et al.</i> , 2011
	1-naphthylamine	200.0	Mh/Mn/G	Hu J. <i>et al.</i> , 2011c
	Estrogens	–	Mn	Guan <i>et al.</i> , 2010
	2,4-dichlorophenol	–	Mn	Dong <i>et al.</i> , 2009

¶ MW: multi-walled, Mn: magnetite, Mh: maghemite, H: hematite, G: goethite

Table 2.2 Previous studies for water treatment of the magnetic composite using magnetic separation techniques

	Contaminants	Polymers	Functional materials	Reference
Heavy metal	Pb(II)	Xanthan gum	Xanthan gum	Peng <i>et al.</i> , 2014
	Cr(VI)	Chitosan	Manganese ferrite	Xiao <i>et al.</i> , 2013
	Pb(II)	Alginate	Zirconium	Li X. <i>et al.</i> , 2013
	Cu(II)	β -cyclodextrin	β -cyclodextrin	Li J. <i>et al.</i> , 2013
	Pb(II)	Gelatin	Gelatin	Ren <i>et al.</i> , 2013
	Cr(VI)	PVA-alginate	Maghemite	Idris <i>et al.</i> , 2012b
	Pb(II)	Alginate	Maghemite	Idris <i>et al.</i> , 2012a
	As(V)	Polystyrene	Magnetite	Jiang <i>et al.</i> , 2012
	Pb(II)	Chitosan	Magnetite	Gregorio-Jauregui <i>et al.</i> , 2012
	Cd(II)	MMA-DVB	Ethylenediamine	Chen <i>et al.</i> , 2011
	Cu(II), Zn(II), Cr(VI)	Chitosan	Diethylenetriamine	Li H. <i>et al.</i> , 2011
	Pb(II), Nd(III), Cu(II), Zn(II), Co(II), Ni(II)	Alginate	P507	Zhang <i>et al.</i> , 2011
	Pb(II)	Alginate	Citrate	Bee <i>et al.</i> , 2011
	La(III)	Alginate-chitosan	Magnetite	Wu <i>et al.</i> , 2011
	Ag(I)	Chitosan	Thiourea	Fan <i>et al.</i> , 2011
	Cr(VI)	Alginate	Maghemite	Idris <i>et al.</i> , 2011
	Pb(II), Ni(II)	Chitosan	Magnetite	Tran <i>et al.</i> , 2010
	Co(II)	Alginate	Cyanex 272®	Ngomsik <i>et al.</i> , 2009
	Hg(II), Pb(II), Cu(II), Cd(II), Zn(II)	EGDMA	1-vinyl-1,2,4-triazole	Uzun <i>et al.</i> , 2009
	Pb(II), Cr(III), Mn(II)	Gellan gum	Magnetite	Wang <i>et al.</i> , 2009
	Cr(VI)	Alginate/PVA	<i>Rhizopus cohnii</i>	Li H. <i>et al.</i> , 2008
	Hg(II)	Chitosan	Thiourea/Glutaraldehyde	Donia <i>et al.</i> , 2008
	Hg(II)	GMA-MMA-EGDMA	Amino groups	Bayramoglu and Arica, 2007
Ni(II)	Alginate	Cyanex 272®	Ngomsik <i>et al.</i> , 2006	
As(V)	HP2MG	Magnetite	Wakui <i>et al.</i> , 2005	

Dye	Methyl orange	Ammonium persulfate	Polyaniline	Yao <i>et al.</i> , 2013
	Congo red	Alginate	Cadmium sulfide	Jiang <i>et al.</i> , 2013
	Direct red 23	Chitosan	Glutaraldehyde	Sanlier <i>et al.</i> , 2013
	Methylene blue	Alginate	Activated carbon	Ai <i>et al.</i> , 2011
	Methyl orange, Methylene blue	Alginate	Activated carbon	Rocher <i>et al.</i> , 2010
	Methyl orange, Methylene blue	Cellulose	Activated carbon	Luo and Zhang, 2009
	Methyl orange, Methylene blue	Alginate	Activated carbon	Rocher <i>et al.</i> , 2008
Organics	Lubricating oil	Polystyrene	Magnetite	Chen <i>et al.</i> , 2013
	1-naphthylamine	β -cyclodextrin	β -cyclodextrin	Li J. <i>et al.</i> , 2013
	Erythromycin, Streptomycin, Tetracycline, Chloramphenicol	BSA	Magnetite	Zhang <i>et al.</i> , 2013
	Gonadotropin	Polyvinyl	N,N-diethylammonium	Muller <i>et al.</i> , 2011
	Trypsin	EGDMA	Glycidyl methacrylate	Arica <i>et al.</i> , 2008
	Immunoglobulin-G	HEMA-EGDMA	IMEO	Ozturk <i>et al.</i> , 2007
	Protein BSA	PMMA	Magnetite	Banert and Peuker, 2007

¶ PVA: polyvinyl alcohol, P507: 2-ethylhexyl phosphonic acid mono-2-ethylhexyl ester, EGDMA: ethyleneglycol dimethylmethacrylate, GMA: glycidylmethacrylate, MMA: methyl methacrylate, DVB: divinylbenzene, HP2MG: 2-propenoic acid, 2-methyl-,1,2-ethanediyl ester, polymer with methyl 2-methyl-2-propenoate, BSA: bovine serumalbumin, HEMA: 2-hydroxyethyl methacrylate, IMEO: 3-(2-imidazole-1-yl)propyl (triethoxysilane)

2.2. Anionic Aqueous Contaminants

Above certain levels of anionic species have been found in the environment and they may be considered as pollutants. Moreover, their bioaccumulation becomes an environmental concern when their concentrations in the environment begin to affect human health and ecosystems (Lito *et al.*, 2012). In recent years, many studies have been investigating to remove harmful anionic contaminant from waters by various treatment technologies such as adsorption, ion-exchange, and reverse osmosis (Goh *et al.*, 2008). Among them, this chapter covers selenium, chromium, arsenic, and phosphorous.

2.2.1. Selenium

Selenium (^{34}Se , Atom wt. 78.96) is a natural trace element that is 68th earth's crustal (Adriano, 2001). It is an essential nutrient for animals and human at appropriate concentration, but toxic at high concentration. The narrow range (0.8-1.7 mmol/L) between selenium deficiency and toxicity is the subject of a concern (Albert *et al.*, 1995). Therefore, US EPA has set the maximum contaminant level in drinking water to be 0.05 mg/L as selenium. In the environment, selenium can exist in four oxidation states (+VI: selenate, +IV: selenite, 0: elemental selenium, -II: selenide) and in several organic forms. The higher valent selenium is more soluble, so selenite (SeO_3^{2-}) and selenate (SeO_4^{2-}) is predominant forms in water. It is introduced in water environment from different sources, both natural and artificial, activities related to the agriculture and combustion of fossil fuels (Loyo *et al.*, 2008; Rovita *et*

al., 2008). A variety of treatment technologies have been reported for selenium removal from contaminated waters (Zhang et al., 2008; Huang et al., 2013; Labaran and Vohra, 2013). Examples include adsorption, biological volatilization, photocatalytic reduction.

2.2.2. Chromium

Chromium can exist in oxidation states ranging from -2 to +6. In aquatic environments, trivalent Cr(III) and hexavalent Cr(VI) are the major forms of chromium, and Cr(VI) is more toxic and cancerous (Zhitkovich, 2011). Chromium contamination of drinking water resources is a serious global environmental problem. In many countries, chromium is present in groundwater at concentrations exceeding the guidelines of the World Health Organization (0.05 mg/L), causing serious health problems (Richard and Bourg, 1991). Various treatment methods have been used for the removal of chromium from water, including coagulation-precipitation, ion exchange, adsorption, and membrane technology. Adsorption can be widely used for chromium removal because of cost-effectiveness and simplicity of operation (Sharma *et al.*, 2011).

2.2.3. Arsenic

Arsenic contamination in drinking water resources is a significant environmental problem around the world. In many countries such as Bangladesh, Chile, India, Nepal, Thailand, and Vietnam, arsenic occurs naturally in groundwater at concentrations exceeding the guidelines of

the World Health Organization (10 $\mu\text{g/L}$), causing serious health problems and human mortality (Adamson and Polya, 2007; Shibasaki *et al.*, 2007; Ahmad *et al.*, 2007). Arsenic is a toxic trace element existing in nature as arsenite (As(III)) and arsenate (As(V)) depending on redox conditions. Under oxidizing environments, As(V) is predominant while As(III) is predominant under reducing conditions. As(III) is more toxic and mobile than As(V) (Bang and Meng, 2004; Gimenez *et al.*, 2007).

2.2.4. Phosphorus

The pollution of water bodies by phosphorus, an essential macronutrient, is a widespread environmental problem, causing eutrophication in lakes and seas and posing a serious threat to aquatic environments (Lee and Kim, 2013). The input of phosphorus to water bodies is divided into two main sources. One is a point source due to human population and inherent activities, and the other is non-point source caused by excessive use of fertilizers to increase the production of crops (Oliveira *et al.*, 2012). According to recent studies, 30 $\mu\text{g/L}$ of phosphorus may be enough to provoke the excessive growth of aquatic plants and algal blooms (Zheng *et al.*, 2011). Several processes have been used to remove phosphorus from water bodies. Examples include chemical precipitation and adsorption with iron oxide nanoparticles (Genz *et al.*, 2004; Yoon *et al.*, 2014).

Chapter 3 Synthesis and Characterization of Magnetic Composites

3.1. Carbon Nanotube/Iron Oxide Magnetic Nanocomposites

Carbon nanotubes (CNTs) have been applied to various fields due to their excellent mechanical, thermal, and electrical properties. Because of their nano-scale structure and large surface area, CNTs could be served as templates for the assembly and combining of nanoparticles on their surface. The composites of CNTs with various compounds could increase their surface functionality such as electrical and magnetic characteristics (Kim *et al.*, 2010; Kim *et al.*, 2011).

Iron oxide nanoparticles, such as magnetite or maghemite, have been investigated by many research groups due to their unique electrical and magnetic properties. The iron oxide nanoparticles have been used in water treatment as well as high-density information storage and electronic devices (Sun *et al.*, 2000; Wan *et al.*, 2007; Yoon *et al.*, 2014). These nano metals has highly reactive and excellent adsorption capacity, but was difficult to separation from water due to their nano size. Decorated iron oxide nanoparticles on supporting materials can maintain high reactivity and improve separation efficiency.

The aims of this chapter were to prepare carbon nanotube/iron oxide magnetic nanocomposites and to analyze surface properties, crystalline structures, and magnetic properties.

3.1.1. Synthesis and characterization methods

Multi-walled carbon nanotube (CM-250, MWCNTs) were obtained

from Hanwha Nanotech, Korea. The MWCNTs had an outer diameter of 10-15 nm, inner diameter of 7-8 nm, length of less than 200 μm , and a purity of approximately 95%. To increase the binding affinity of carbon nanotube and magnetic iron oxides, additional purification process was conducted in concentrated nitric acid at 70°C with stirring for 12 h. Then the oxidized carbon nanotube was filtered and washed with distilled water, and dried at 110°C for 6 h.

The synthesis methods of carbon nanotube/iron oxide magnetic nanocomposites were as follows. A 400 ml solution (Fe(III)/Fe(II) molar ratio = 2) of $\text{FeCl}_3 \cdot 6\text{H}_2\text{O}$ (0.1 mol) and $\text{FeSO}_4 \cdot 7\text{H}_2\text{O}$ (0.05 mol) was prepared. Two grams of oxidized MWCNTs were added to the mixed solution and dispersed by ultrasonication for 4 h. Then, 6 M NaOH solution was added by drop-wise until the solution pH reached 8. The solution was continually stirred for a further 12 h to ensure completion of the reaction. Then the precipitates were washed with distilled water and dried at 150°C for 6 h. The synthesis of iron oxide magnetic nanoparticles were prepared by following the method described above but without carbon nanotube. The schematic diagram of the synthetic methods of the carbon nanotube/iron oxide magnetic nanocomposites was shown in Figure 3.1.

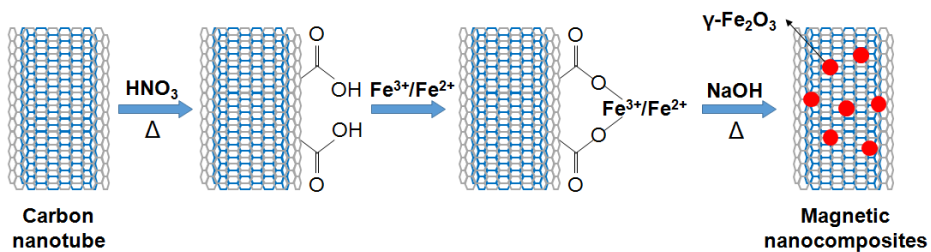


Figure 3.1 Schematic illustration of the synthesis of the carbon nanotube/iron oxide magnetic nanocomposites.

The surface properties was analyzed by scanning electron microscopy (SEM), transmission electron microscope (TEM), nitrogen sorption, Fourier transform infrared (FTIR), point of zero charge (pH_{PZC}). Field emission scanning electron microscopy (FESEM) analysis was performed using a field emission scanning electron microscope (Supra 55VP; Carl Zeiss, Oberkochen, Germany). TEM images were obtained from a high resolution transmission electron microscope (JEM-3010, JEOL, Japan). Nitrogen gas (N_2) adsorption-desorption experiments were performed using a surface area analyzer (BELSORP-max, BEL Japan Inc., Japan) after the sample was pretreated at 120°C . From the N_2 adsorption-desorption isotherms, the specific surface area, average pore diameter, total pore volume, and mesopore volume were determined using Brunauer-Emmett-Teller (BET), Barrett-Joyner-Halenda (BJH), and Horvath-Kawazoe (HK) analyses. Infrared spectra were recorded on a Nicolet 6700 (Thermo Scientific, USA) Fourier-transform infrared spectrometer using KBr pellets. pH_{PZC} was determined by the potentiometric titration methods (Appel *et al.*, 2003). One gram of carbon nanotube/iron oxide magnetic nanocomposites was added to 500 ml beakers with 100 ml of electrolyte solution (0.1, 0.01 and 0.001 M NaCl). After equilibrium reached, 0.1 M HCl or 0.1 M NaOH was added to each electrolyte solution to decrease or increase the solution pH in the range between 2 and 12, respectively, and the amount of added 0.1 M HCl or 0.1 M NaOH was calculated.

The crystalline structures was analyzed by X-ray analysis. The structure of oxidized carbon nanotube and carbon nanotube/iron oxide

magnetic nanocomposites were determined using a powder X-ray diffractometer (XRD Geigerflex D/max rA, Rigaku, Japan) with Cu K α radiation at fixed power source (40 kV and 30 mA). The diffraction data were collected over a 2 θ range between 3 and 70°, at a scanning rate of 2.0°/min. Energy dispersive X-ray spectrometry (EDS) analysis were performed using a field emission scanning electron microscope (Supra 55VP; Carl Zeiss, Oberkochen, Germany). The oxidation states of metal on the surface of the sample were analyzed by X-ray photoelectron spectroscopy (XPS SIGMA PROBE, Thermo VG, U.K) scans using monochromatic Al K α radiation.

The magnetic properties of iron oxide magnetic nanoparticles and carbon nanotube/iron oxide magnetic nanocomposites were measured using a vibrating sample magnetometer (VSM 5-15, Toei Industry Co., Japan) with field measurement range ± 5.0 kOe at room temperature.

3.1.2. Surface characterization

The surface morphology was characterized by scanning electron micrographs (SEM) and transmission electron micrographs (TEM). Figure 3.2 showed the SEM images of (a) oxidized carbon nanotube and (b) carbon nanotube/iron oxide magnetic nanocomposites. In contrast to the aligned type of oxidized carbon nanotube, the magnetic nanocomposites depicts the entangled with iron oxide nanoparticles. More detail microstructure of the multi-wall of carbon nanotube was revealed by the TEM image in Figure 3.3. The oxidized carbon nanotube (Figure 3.3 (a) and (b)) had hallow inner tube diameter of 7-8 nm, outer diameter of 10-15 nm, and length ranging from hundreds of

nanometers to micrometers. There was opened edge of carbon nanotube found and the amorphous carbon did not exist. The TEM image of magnetic nanocomposites (Figure 3.3 (c) and (d)) showed nano-sized iron oxide particles growing on the surface of oxidized carbon nanotube regularly with diameters ranging from 6 to 17 nm.

The nitrogen adsorption-desorption curves for samples was shown in Figure 3.4. The adsorption isotherms of the samples can be described as a Type-II isotherm with characteristic H1 hysteresis, which is typical for mesoporous materials (Lee and Park, 2012; Wang *et al.*, 2012). The adsorption volume decreased after synthesis nanocomposites, which suggested decreased the specific surface area and total pore volume. According to the Brunauer–Emmett–Teller (BET) theory, a specific surface area of magnetic nanocomposites $119.09 \text{ m}^2/\text{g}$ with total pore volume of $0.4748 \text{ cm}^3/\text{g}$ and average pore diameter 15.947 nm , which was smaller than that of $189.03 \text{ m}^2/\text{g}$, $0.7625 \text{ cm}^3/\text{g}$ and 16.134 nm for oxidized carbon nanotube. And the Barrett–Joyner–Halenda (BJH) model determined the mesopore volume of $0.4656 \text{ cm}^3/\text{g}$ for magnetic nanocomposites and $0.7509 \text{ cm}^3/\text{g}$ for oxidized carbon nanotube. The Horvath–Kawazoe (HK) analysis was also performed for micropore size distributions. The results were shown in Table 3.1.

Analysis of Fourier transform infrared (FTIR) spectra could provide information about surface functional groups. The FTIR spectra of oxidized carbon nanotube and magnetic nanocomposites were depicted in Figure 3.5. The band at 3417 cm^{-1} (the O–H bond vibration), 1565 cm^{-1} (the C=O bond vibration), 1163 cm^{-1} (the C–C bond vibration), which suggests the surface of oxidized carbon nanotube possesses a

certain amount of oxygen-containing functional groups. That is the nitric acid in additional purification process could introduce some carboxylic groups on the outside surface of carbon nanotube, which would serve as reactive and anchoring sites for nucleation and growth of magnetic particles (Ai *et al.*, 2011; Kim *et al.*, 2010; Gupta *et al.*, 2011). The peaks at 636 and 585 cm^{-1} in the spectrum of magnetic nanocomposites are assigned to the Fe-O bond vibration of maghemite particles (Hu *et al.*, 2008).

The surface charge assessed by point of zero charge (pH_{PZC}) is defined as the point where the zeta potential is zero. When $\text{pH} < \text{pH}_{\text{PZC}}$, the surface charge is positive, and when $\text{pH} > \text{pH}_{\text{PZC}}$, the surface charge is negative. In this case, the pH_{PZC} of the magnetic nanocomposites determined by the potentiometric titration method (Figure 3.6) is about 5.1.

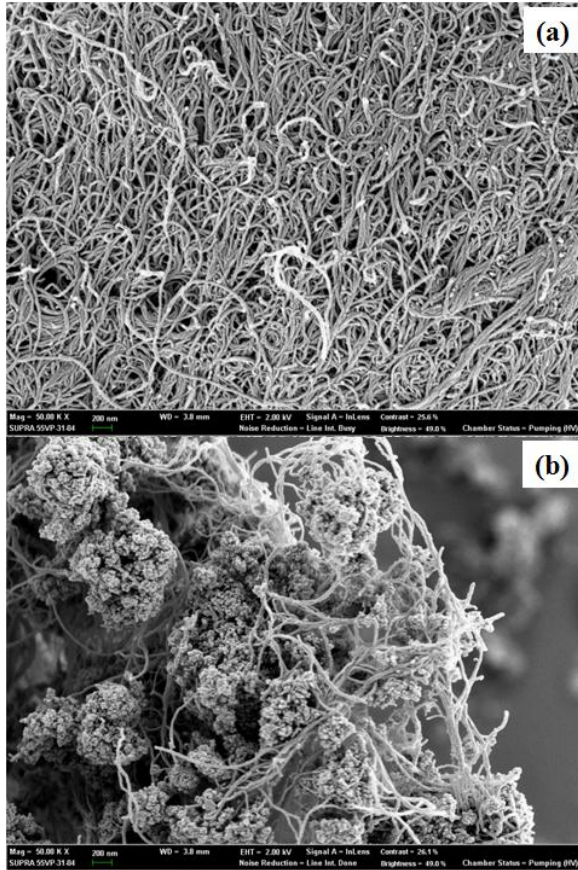


Figure 3.2 Field emission scanning electron micrographs of (a) oxidized carbon nanotube and (b) carbon nanotube/iron oxide magnetic nanocomposites (x 50.00K).

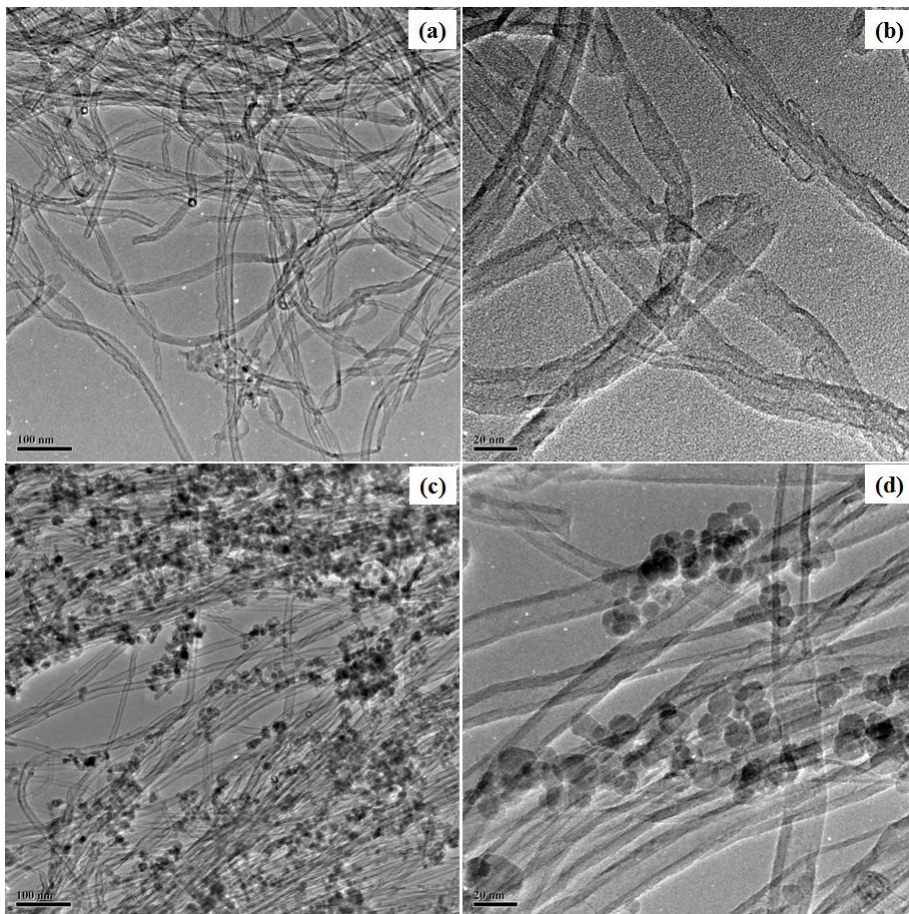


Figure 3.3 Transmission electron micrographs of (a, b) oxidized carbon nanotube and (c, d) carbon nanotube/iron oxide magnetic nanocomposites.

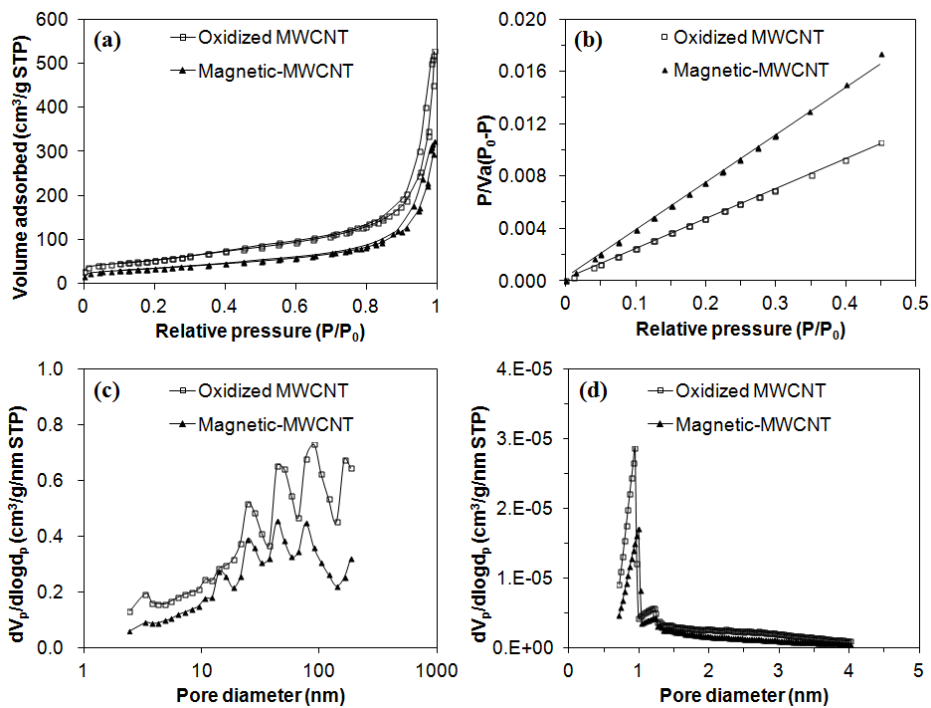


Figure 3.4 Nitrogen sorption and pore size distribution methods: (a) N₂ adsorption-desorption curves; (b) BET analysis; (c) BJH methods; (d) HK methods.

Table 3.1 Physical characteristics of oxidized carbon nanotube and carbon nanotube/iron oxide magnetic nanocomposites obtained from the N₂ adsorption–desorption data

Characteristics	Oxidized carbon nanotube	Magnetic nanocomposites	Unit
<i>Brunauer–Emmett–Teller (BET) analysis</i>			
Monolayer volume (V_m)	43.431	27.361	cm ³ /g
BET specific surface area ($a_{s,BET}$)	189.03	119.09	m ² /g
BET constant	120.49	139.05	-
Total pore volume (V_p)	0.7625	0.4748	cm ³ /g
Average pore diameter ($d_{p,ave}$)	16.134	15.947	nm
<i>Barrett–Joyner–Halenda analysis</i>			
Mesopore volume ($V_{p,me}$)	0.7509	0.4656	cm ³ /g
Peak diameter of mesopore ($d_{p,me}$)	90.22	43.57	nm
<i>Horvath–Kawazoe analysis</i>			
Micropore volume ($V_{p,mi}$)	0.0116	0.0092	cm ³ /g
Peak diameter of micropore ($d_{p,mi}$)	0.94	0.99	nm

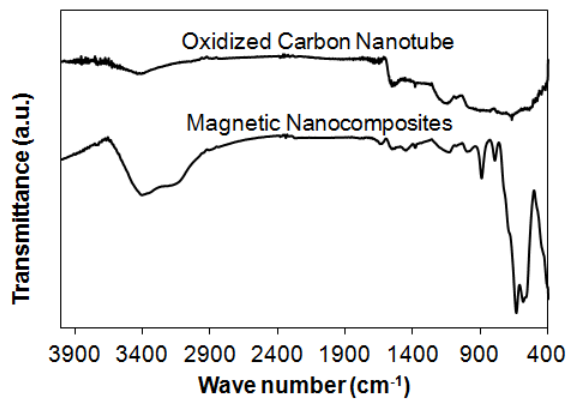


Figure 3.5 FTIR spectra of oxidized carbon nanotube and carbon nanotube/iron oxide magnetic nanocomposites.

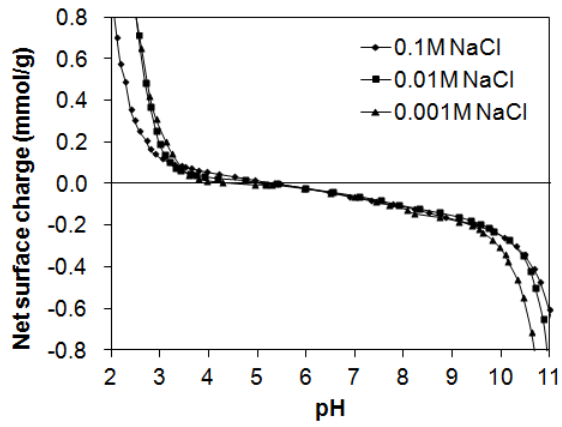


Figure 3.6 Potentiometric titration curves for carbon nanotube/iron oxide magnetic nanocomposites.

3.1.3. X-ray analysis

Color mapping was performed using energy dispersive X-ray spectrum (EDS) to visualize the spatial distribution of carbon, oxygen, and iron (Figure 3.7 and 3.8). The mapping image was shown all components well dispersed on surface of sample. Through the EDS analysis (Figure 3.9 (a)), the surface of oxidized carbon nanotube was consisted 96.89 atomic % of carbon and 3.11 atomic % of oxygen. In case of magnetic carbon nanotube/iron oxide magnetic nanocomposites (Figure 3.9 (b)), it was consisted 84.55 atomic % of carbon, 12.27 atomic % of oxygen, and 3.18 atomic % of iron. Due to the iron was produced on the oxidized carbon nanotube surface, the proportion of carbon was reduced and the proportion of oxygen was increased.

To investigate the crystalline of these nanocomposites, XRD measurements were performed. As shown in Figure 3.10 the two peaks corresponding to the structure of oxidized carbon nanotube also exist in the XRD pattern of the magnetic nanocomposites. Other peaks were revealed a cubic iron oxide phase, which are close to JCPD standards: γ -Fe₂O₃ (maghemite, 89-5892, $2\theta = 30.266, 35.651, 43.332, 53.766, 57.319, 62.949$) and α -FeOOH (goethite, 81-0464, $2\theta = 21.240, 33.243, 41.183, 58.998$).

The XPS spectra of carbon nanotube/iron oxide magnetic nanocomposites were shown in Figure 3.11. The photoelectron peaks at binding energy of about 712, 531, and 285 eV in wide scan were attributed to Fe2p, O1s, and C1s, respectively. The results indicate that the nanocomposites were composed of iron, oxygen, and carbon. The high-resolution scan of Fe2p region marked two peaks at 724.6 and

711.2 eV, which was agreed with literature data for maghemite and substantiate the XRD data (Sun *et al.*, 2005; Kim *et al.*, 2010). Thus, the formation of iron oxide in the magnetic-MWCNTs nanocomposites was maghemite.

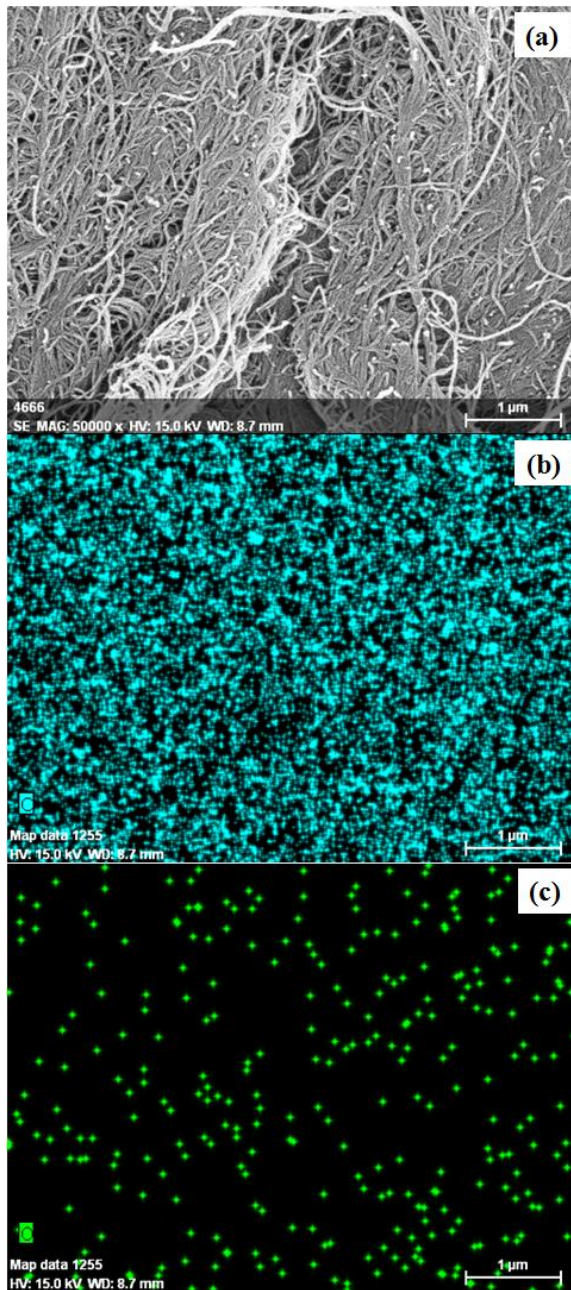


Figure 3.7 Color mapping of oxidized carbon nanotube: (a) SEM image of mapping point; (b) carbon (C) map; (c) oxygen (O) map.

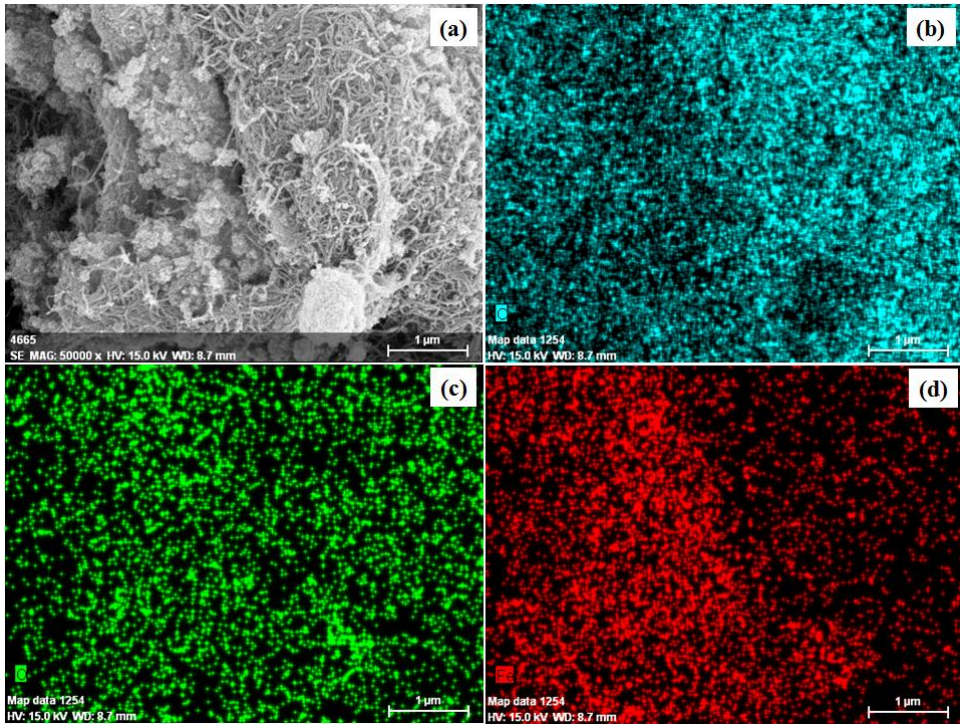


Figure 3.8 Color mapping of magnetic nanocomposites: (a) SEM image of mapping point; (b) carbon (C) map; (c) oxygen (O) map; (d) iron (Fe) map.

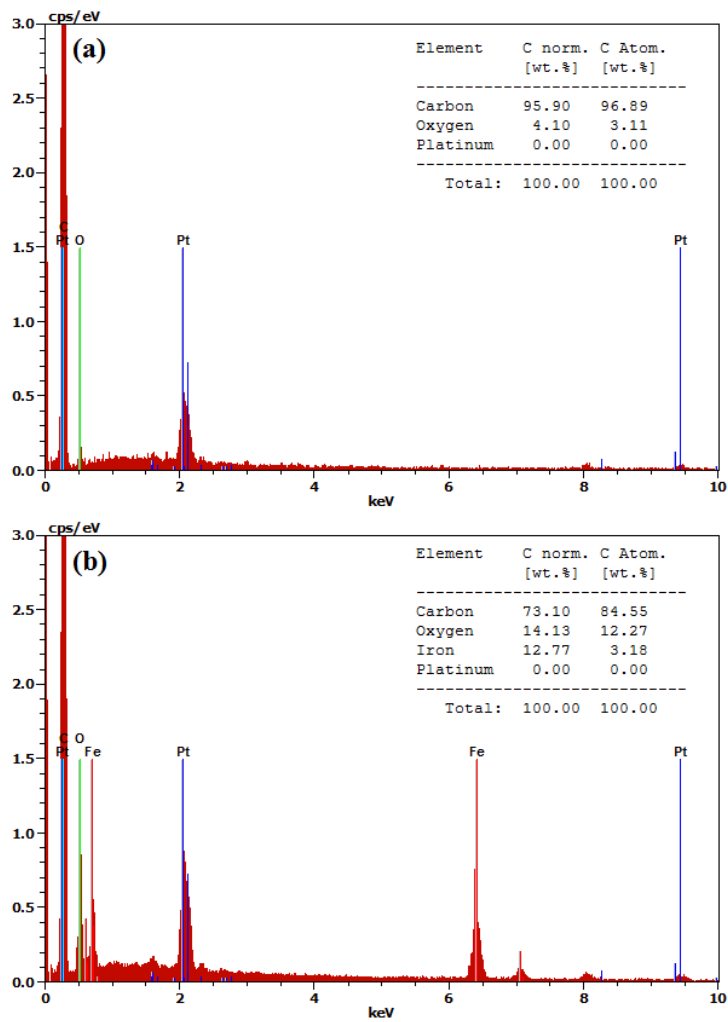


Figure 3.9 Energy dispersive X-ray spectrums of (a) oxidized carbon nanotube and (b) carbon nanotube/iron oxide magnetic nanocomposites.

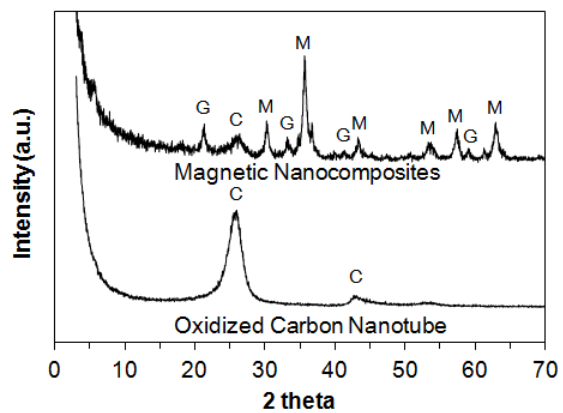


Figure 3.10 XRD patterns of oxidized carbon nanotube and carbon nanotube/iron oxide magnetic nanocomposites (C= carbon, G= goethite, M= maghemite).

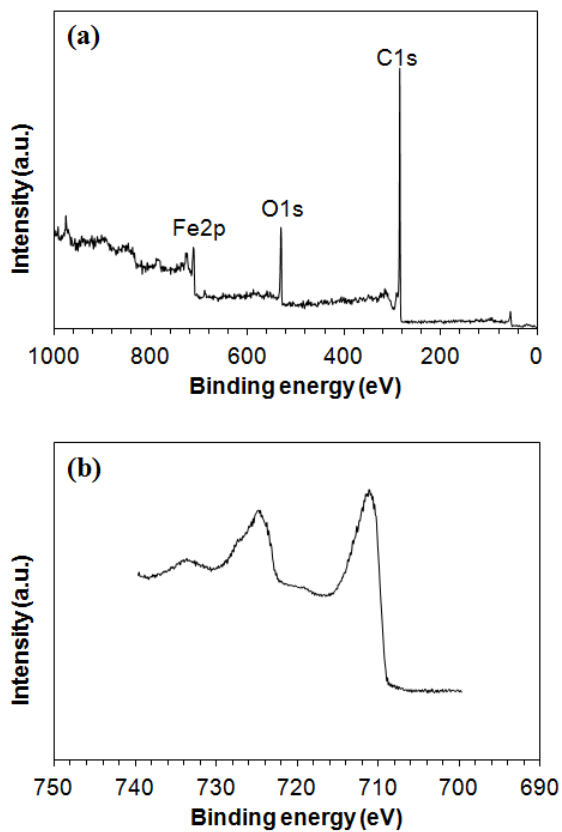


Figure 3.11 XPS spectra of carbon nanotube/iron oxide magnetic nanocomposites: (a) wide scan; (b) high-resolution scan of Fe2p region.

3.1.4. Magnetic properties

Digital snapshot images of carbon nanotube/iron oxide magnetic nanocomposites under external permanent magnet condition were shown in Figure 3.12. The magnetic nanocomposites can be easily separated from the aqueous solution within few seconds by placing a permanent magnet near the glass vials.

The magnetic properties of iron oxide magnetic nanoparticles and carbon nanotube/iron oxide magnetic nanocomposites were shown in Figure 3.13. The saturation magnetization (M_s) of the nanocomposites obtained from Figure 3.13(b) is 39.37 emu/g, which is considerably smaller than that of bulk iron ($M_s = 222$ emu/g). But, the coercivity (H_c) of the samples obtained from Figure 3.13(b) is 15.66 Oe, which is much larger than that of bulk iron ($H_c = 1$ Oe). The magnetization ($M_s = 43.29$ emu/g) and coercivity ($H_c = 26.27$ Oe) of the iron oxides (Figure 3.13(a)) are both higher than those of carbon nanotube/iron oxide magnetic nanocomposites, which should be mainly attributed to the small size of iron oxides that were formed in the presence of carbon nanotube (Sun *et al.*, 2005; Kim *et al.*, 2010).

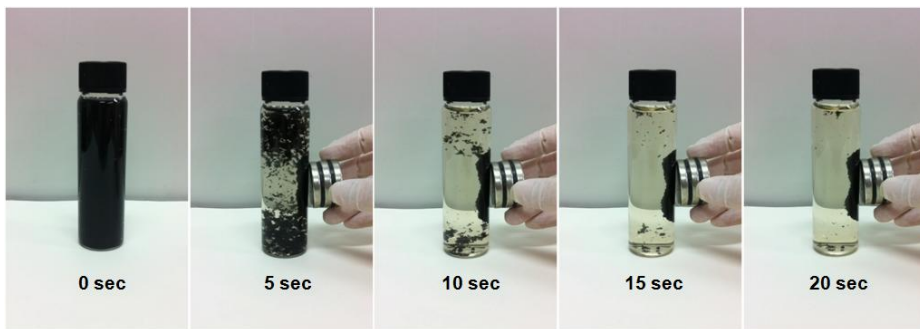


Figure 3.12 Digital snapshot images of carbon nanotube/iron oxide magnetic nanocomposites under external permanent magnet condition.

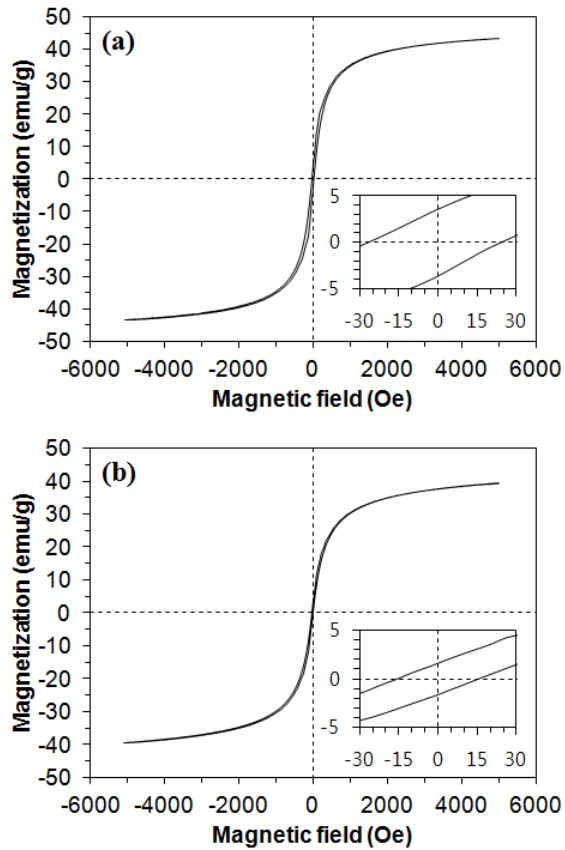


Figure 3.13 Magnetic hysteresis curves for (a) magnetic iron oxide nanoparticles and (b) carbon nanotube/iron oxide magnetic nanocomposites.

3.2. Magnetic Alginate-Layered Double Hydroxide Composites

Magnetic separation is an innovative technology and has been applied by several researchers to water treatment and purification (Yavuz *et al.*, 2009). For magnetic separation, magnetic particles such as magnetite (Fe_3O_4) and maghemite ($\gamma\text{-Fe}_2\text{O}_3$) are immobilized into polymers such as alginate, chitosan, polyvinyl alcohol, and gellan gum to form magnetic beads or composites (Yavuz *et al.*, 2009). In addition, functional materials are added into the beads/composites to remove target contaminants.

Layered double hydroxides (LDHs) are a class of nanostructured anionic clays. They consist of positively charged brucite-like sheets that are balanced by the intercalation of anions in the hydrated interlayer regions (Goh *et al.*, 2008). LDHs have high surface areas, large anion exchange capacities, and good thermal properties (Cavani *et al.*, 1991). Several researchers have investigated the removal of various contaminants using LDHs.

The aims of this chapter were to prepare magnetic alginate-layered double hydroxide composites and to analyze the surface properties by scanning electron microscopy (SEM) and nitrogen adsorption-desorption analysis; the crystalline structures by X-ray analysis (energy dispersive X-ray spectrometry (EDS), X-ray diffractometer (XRD), X-ray fluorescence spectrometer (XRF)); and magnetic properties by vibrating sample magnetometer (VSM).

3.2.1. Synthesis and characterization methods

All chemicals used for the experiments were purchased from Sigma Aldrich. Magnetic iron oxide particles were prepared by co-precipitating a solution of iron sulfate ($\text{FeSO}_4 \cdot 7\text{H}_2\text{O}$) and iron chloride ($\text{FeCl}_3 \cdot 6\text{H}_2\text{O}$). An alkali solution of sodium hydroxide (NaOH) was added drop wise into a 500 mL solution of $\text{FeSO}_4 \cdot 7\text{H}_2\text{O}$ (0.125 mol) and $\text{FeCl}_3 \cdot 6\text{H}_2\text{O}$ (0.25 mol) with intensive stirring at room temperature until pH 8.0 was reached. The resulting precipitates were aged at 60°C for 18 h and then washed thoroughly with deionized water to remove excess sodium. The washed precipitates were oven-dried at 150°C for 6 h and then pulverized in a ball mill.

The Mg-Al LDHs powders were synthesized by co-precipitating mixtures of magnesium nitrate ($\text{Mg}(\text{NO}_3)_2 \cdot 6\text{H}_2\text{O}$) and aluminum nitrate ($\text{Al}(\text{NO}_3)_3 \cdot 9\text{H}_2\text{O}$). A 700 mL solution (Mg/Al molar ratio = 2) of $\text{Mg}(\text{NO}_3)_2 \cdot 6\text{H}_2\text{O}$ (1 mol) and $\text{Al}(\text{NO}_3)_3 \cdot 9\text{H}_2\text{O}$ (0.5 mol) was added drop wise into 1,000 mL of an alkali solution (pH = 13) of sodium hydroxide (NaOH) and sodium carbonate (Na_2CO_3) using a peristaltic pump (QG400, Fasco, Springfield, MO, USA) at 3 mL/min under intensive stirring at room temperature. The resulting precipitates were aged at 65°C for 18 h in the mother liquor. The precipitates were washed thoroughly with deionized water to remove excess sodium. Then, final suspensions were centrifuged at $11,200 \times g$ (8,500 rpm) for 20 min. The washed precipitates were oven-dried again at 65°C for 24 h and were then pulverized in a ball mill. The calcined Mg-Al LDHs used for the experiments was finally obtained via thermal treatment at 300°C for 24 h in an electric muffle furnace (C-FMA, Vision Lab, Seoul, Korea). The

previous experiments showed that the Mg-Al LDHs calcined at 300°C had a higher BET surface area and total pore volume than the untreated LDHs (Kim et al., 2012). Digital image of a powder form of magnetic iron oxide and layered double hydroxides used in the synthesis of magnetic composites was shown in Figure 3.14. The color of the magnetic iron oxide was light brown and the Mg-Al LDHs was white. Particle size of the powder was fine enough to pass through a #100 sieve.

Magnetic alginate–LDHs composites were prepared by entrapping powdered forms of both calcined Mg-Al LDHs and magnetic iron oxide in an alginate hydrogel. One gram of sodium alginate powder was added to 100 mL deionized water to prepare a sodium alginate solution at room temperature. Then, the desired amount of calcined LDHs and magnetic iron oxide (8% w/v; for instance, 6 g calcined LDHs + 2 g magnetic iron oxide) were added to 100 mL of an alginate solution under intensive stirring to obtain a homogeneous suspension. ‘8% w/v’ was used to synthesize the magnetic composites because a higher percentage (>8%) was found to cause clogging at the outlet of the scalp vein set during synthesis. The suspension was allowed to drop using a disposable scalp vein set (needle diameter = 0.7 mm) equipped with a syringe pump (78-1100I, Fisher Scientific) at 4 mL/min into a stirred reservoir containing 200 mL of a 0.3 M calcium chloride (CaCl₂) solution. The resulting composites were allowed to cure in the same CaCl₂ solution for 24 h under stirring and for another 24 h without stirring. Then the magnetic composites were rinsed with deionized water to remove any excess Ca²⁺. Prior to use, the magnetic

composites were dried in an oven at 60°C for 24 h. The schematic diagram of the synthetic methods of the magnetic alginate-layered double hydroxide composites was shown in Figure 3.15.

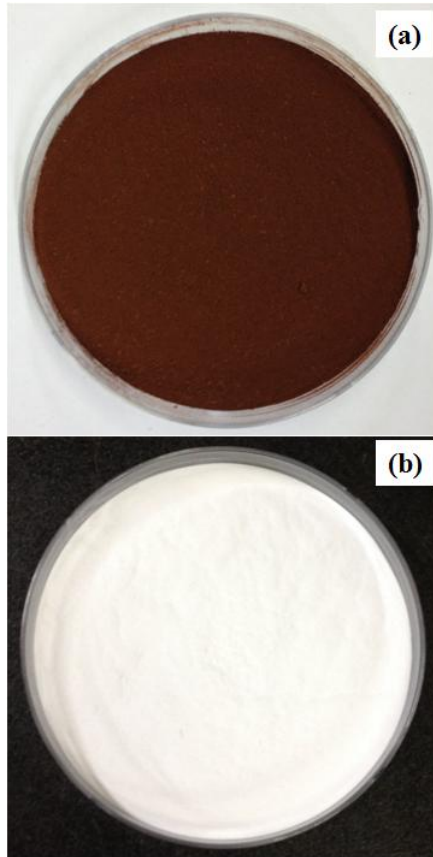


Figure 3.14 Powder form of (a) magnetic iron oxide and (b) layered double hydroxides used in the synthesis of magnetic composites.

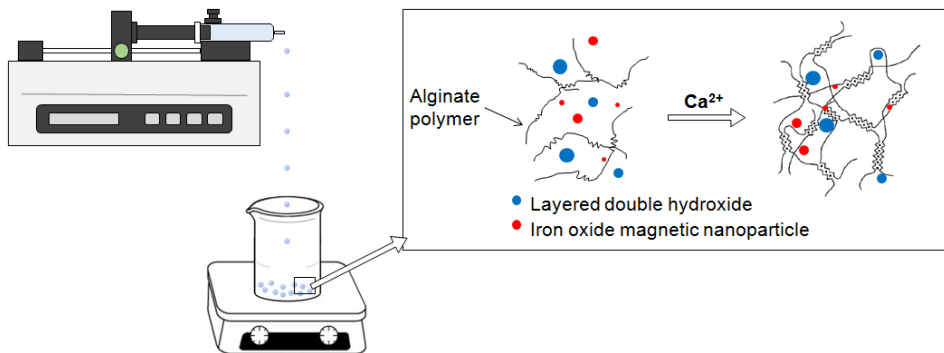


Figure 3.15 Schematic illustration of the synthesis of the magnetic alginate-layered double hydroxide composites.

The magnetic composites were observed and examined with X-ray microanalysis. Specimens were mounted on metal stubs using carbon tape and sputter-coated with platinum (approximately 20 nm in thickness). Specimens were examined with a field emission scanning electron microscope (FESEM; Supra 55VP; Carl Zeiss, Oberkochen, Germany) at an accelerating voltage of 3 kV. In addition, the elemental composition was determined with energy-dispersive X-ray spectrometry (EDS; XFlash 4000; Bruker AXS, Berlin, Germany), combined with an electron microscope at an accelerating voltage of 15 kV. X-rays were collected with a detector fixed at a take-off angle of 35° and region analysis and mapping were performed on the specimens. Nitrogen gas (N₂) adsorption–desorption isotherms of the magnetic composites were measured by a surface area analyser (BELSORP-max, BEL Japan Inc., Japan) after the sample was pretreated at 120°C. From the N₂ adsorption-desorption isotherms, the specific surface area, average pore diameter, total pore volume, and mesopore volume were determined using Brunauer-Emmett-Teller (BET), Barrett-Joyner-Halenda (BJH), and Horvath–Kawazoe (HK) analyses.

Mineralogical and crystalline structural properties of magnetic iron oxide and calcined Mg-Al LDHs were examined using X-ray diffractometry (XRD, D8 Advance, Bruker, Germany) with Cu K α radiation at 1.5406 Å at a scanning speed of 0.6 °/s. The chemical composition of the magnetic composites was investigated using an X-ray fluorescence spectrometer (XRF; S4 pioneer, Bruker, Germany).

The magnetic properties of magnetic alginate-layered double hydroxide composites were measured using a vibrating sample

magnetometer (VSM 5-15, Toei Industry Co., Japan) with field measurement range ± 5.0 kOe at room temperature.

3.2.2. Surface characterization

The digital images of the magnetic alginate-layered double hydroxide composites used in the experiments are presented in Figure 3.16. The magnetic composites had a sphere shape and red-brown color. The size distribution of magnetic beads was obtained from digital image of 31 beads using an image analysis programs (ImageJ). The mean diameter and standard deviation of the magnetic beads were 1.50 and 0.12 μm , respectively.

The surface morphology was characterized by scanning electron micrographs (SEM) image. The spherical surface (Figure 3.17(a)) and the cross-sectional surface (Figure 3.17(b)) of magnetic composites appeared to be overall heterogeneous in surface topography. It was common to observe powders of magnetic iron oxide and layered double hydroxides were intermingled with alginate polymers.

The N_2 adsorption-desorption isotherms of the magnetic composites along with related analyses are shown in Figure 3.18. The physical properties of the magnetic composites obtained from the N_2 adsorption-desorption data were summarized in Table 3.2. The magnetic composites had the BET specific surface area of $73.3 \text{ m}^2/\text{g}$, total pore volume of $0.25 \text{ cm}^3/\text{g}$, mesopore volume of $0.24 \text{ cm}^3/\text{g}$, and micropore volume of $0.01 \text{ cm}^3/\text{g}$.

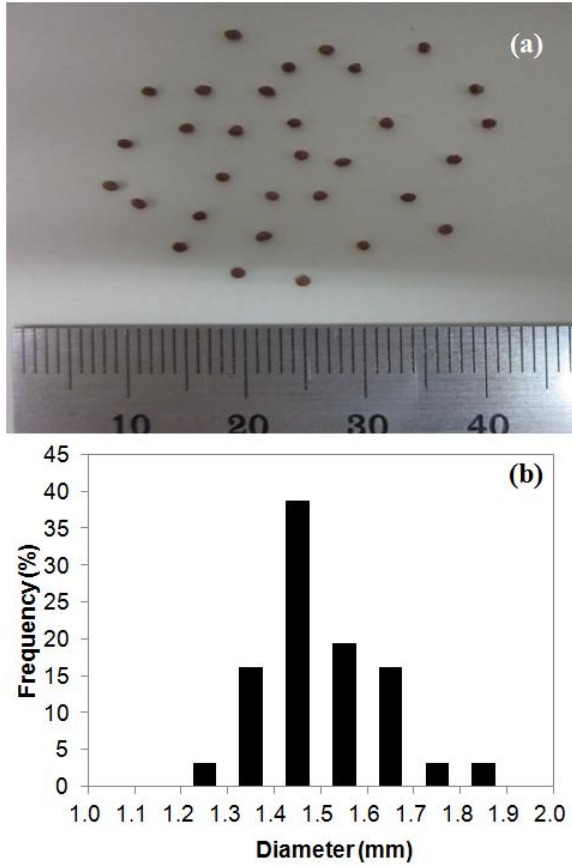


Figure 3.16 Digital images of (a) magnetic alginate-layered double hydroxide composites and (b) size distribution.

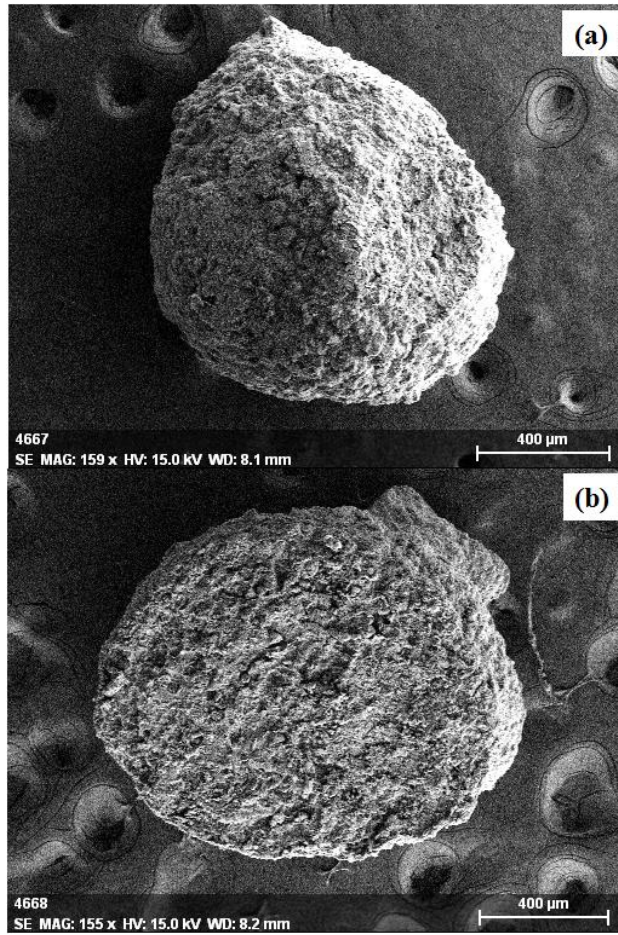


Figure 3.17 SEM images of magnetic alginate-layered double hydroxide composites: (a) surface area; (b) cross section area.

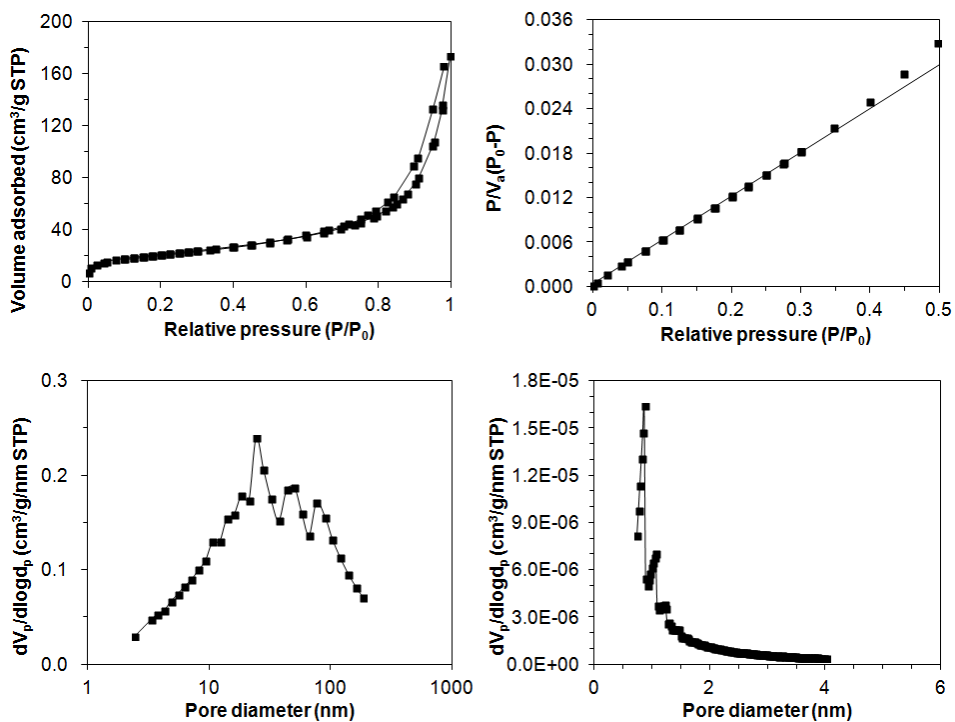


Figure 3.18 Nitrogen sorption and pore size distributions of magnetic composites: (a) N₂ adsorption-desorption curves; (b) BET analysis; (c) BJH methods; (d) HK methods.

Table 3.2 Physical characteristics of the magnetic composites obtained from the N₂ adsorption–desorption data

Characteristics	Value	Unit
<i>Brunauer–Emmett–Teller (BET) analysis</i>		
Monolayer volume (V_m)	18.65	cm ³ /g
BET specific surface area ($a_{s,BET}$)	73.3	m ² /g
BET constant	139.7	-
Total pore volume (V_p)	0.25	cm ³ /g
Average pore diameter ($d_{p,ave}$)	13.54	nm
<i>Barrett–Joyner–Halenda analysis</i>		
Mesopore volume ($V_{p,me}$)	0.24	cm ³ /g
Peak diameter of mesopore ($d_{p,me}$)	24.41	nm
<i>Horvath–Kawazoe analysis</i>		
Micropore volume ($V_{p,mi}$)	0.01	cm ³ /g
Peak diameter of micropore ($d_{p,mi}$)	0.86	nm

3.2.3. X-ray analysis

The EDS pattern and color mappings of the magnetic alginate-layered double hydroxide composites were illustrated in Figure 3.19 ~ Figure 3.21. Color mappings were performed to visualize the spatial distribution of carbon (C), iron (Fe), magnesium (Mg), and aluminium (Al) on the magnetic composites. C and Fe were colored as green and pink, whereas Mg and Al were visualized as red and yellow, respectively. The mapping image were shown all components well dispersed on surface area (Figure 3.19) and cross section area (Figure 3.20) of sample. The EDS pattern (Figure 3.21) demonstrates that iron (Fe), magnesium (Mg), and aluminium (Al) were the major elements of the magnetic composites. Through EDS analysis, Fe was found on the magnetic composites at peak positions of 0.707, 6.403, and 7.057 keV as L alpha, K alpha, and K beta signals, respectively. In addition, Mg and Al were evident at the peak positions of 1.254 keV as K alpha X-ray signal and of 1.486 keV as K alpha signal, respectively. The surface of cross section area of magnetic composites was consisted 13.98 atomic % of magnesium, 9.36 atomic % of aluminium, and 7.10 atomic % of iron.

XRD data (Figure 3.22) show that calcined Mg-Al LDHs had a sharp and intense line at low 2θ and less intense lines at high 2θ with the peaks corresponding to LDHs (JCPDS 53-0005, $2\theta = 26.939, 33.833, 36.371, 43.704, 60.188, 61.847$), which conformed well with the literature (Kanezaki, 1998). The calcined Mg-Al LDHs had a chemical composition of $\text{Mg}_{0.7}\text{Al}_{0.28}(\text{OH})_{1.98}(\text{CO}_3)_{0.15} \cdot 0.48\text{H}_2\text{O}$. The

XRD pattern of magnetic iron oxide indicated the peaks corresponding to maghemite (γ -Fe₂O₃, JCPDS 89-5892, $2\theta = 30.266, 35.651, 43.332, 53.766, 57.319, 62.949$) and goethite (α -FeOOH, JCPDS 81-0464, $2\theta = 21.240, 33.243, 41.183, 58.998$).

The chemical composition from XRF analysis (Table 3.3) indicates that the magnetic composites were composed of C/H (53.0 %), Mg (22.4 %), Al (12.7 %), Fe (9.2 %), and Ca (2.7 %). Note that C/H and Ca came from alginate matrix, whereas Mg and Al from calcined LDHs and Fe from magnetic iron oxide.

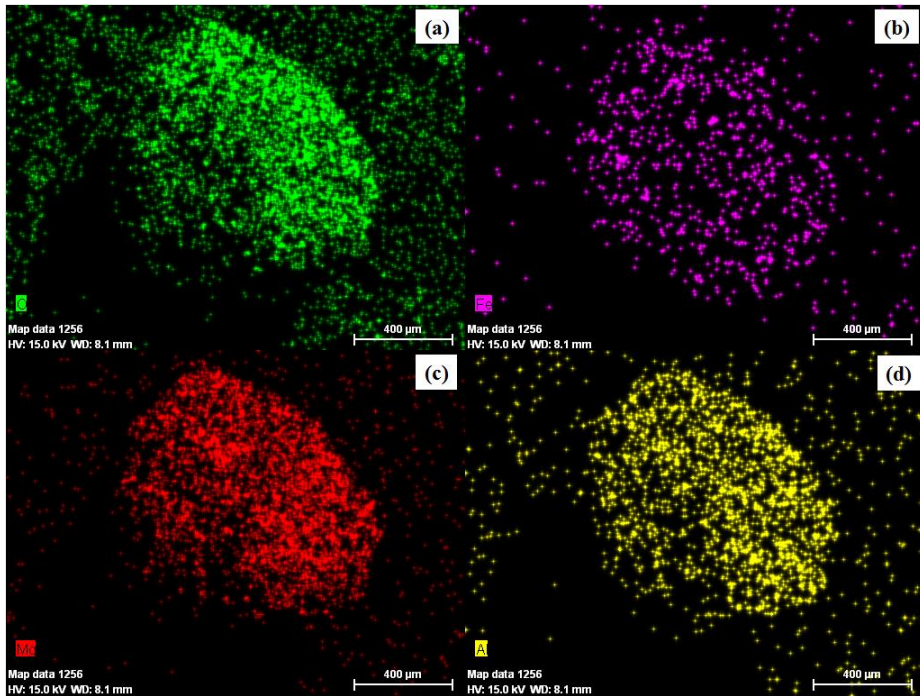


Figure 3.19 Color mapping of magnetic composites at surface area: (a) carbon (C) map; (b) iron (Fe) map; (c) magnesium (Mg) map; (d) aluminum (Al) map.

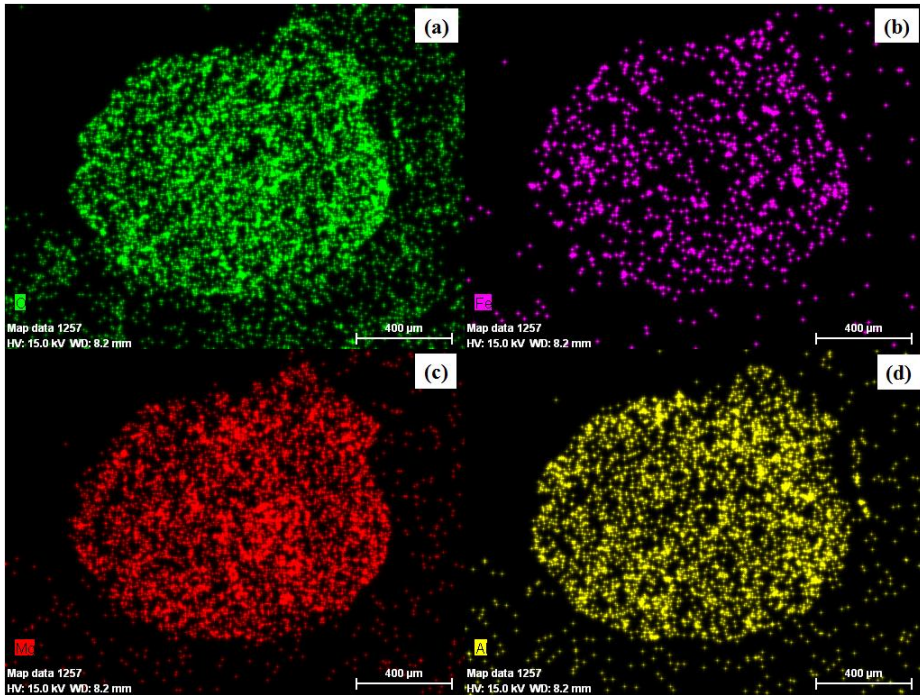


Figure 3.20 Color mapping of magnetic composites at cross section area: (a) carbon (C) map; (b) iron (Fe) map; (c) magnesium (Mg) map; (d) aluminum (Al) map.

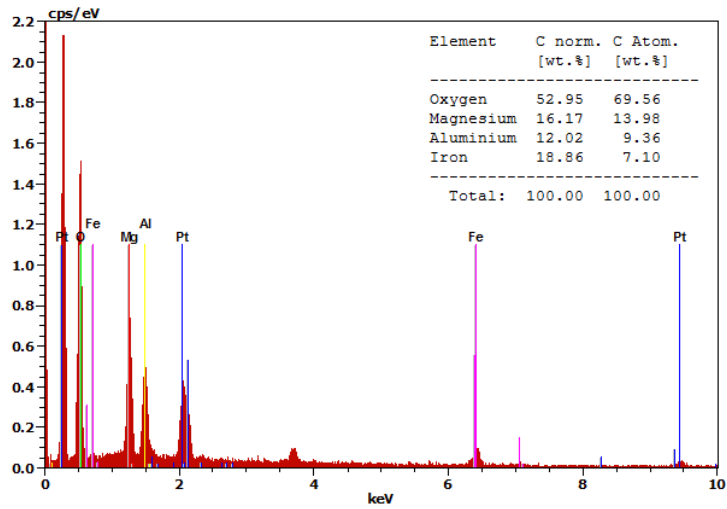


Figure 3.21 Energy dispersive X-ray spectrums of magnetic alginate-layered double hydroxide composites.

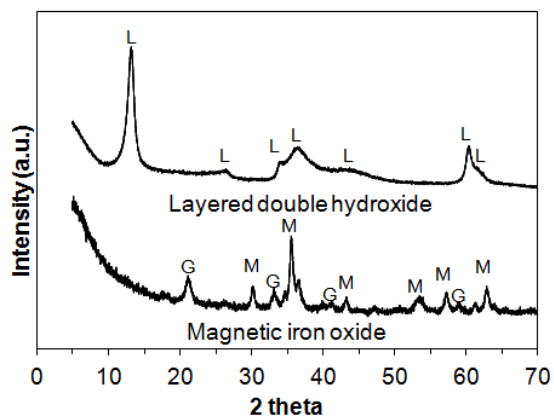


Figure 3.22 XRD patterns of magnetic iron oxide and layered double hydroxides used in the synthesis of magnetic composites.

Table 3.3 Chemical composition of magnetic alginate-layered double hydroxide composites (data from XRF analysis)

Chemical compositions (weight %)					
CHO	MgO	Al ₂ O ₃	Fe ₂ O ₃	CaO	Total
53.0	22.4	12.7	9.2	2.7	100

3.2.4. Magnetic properties

The digital images of the magnetic alginate-layered double hydroxide composites used in the experiments are presented in Figure 3.23. They showed magnetic properties under an external magnetic field. VSM data of magnetic composites were shown in Figure 3.24. The saturation magnetization (M_s) of the nanocomposites obtained from Figure 3.24 was 4.686 emu/g, which is considerably smaller than that of bulk iron ($M_s = 222$ emu/g). This result was similar to the report of Denkbas *et al.* (2002) showing that the saturation magnetization (M_s) of magnetic chitosan microspheres was ~ 4.6 emu/g. The coercivity (H_c) of the samples obtained from image was 36.47 Oe, which is much larger than that of bulk iron ($H_c = 1$ Oe). This hysteresis phenomenon was the unique characteristic of the ferromagnetic behavior. Similar results were reported to hollow nickel submicrometer sphere ($H_c = 32.3$ Oe) and magnetic alginate nanocomposite ($H_c = 163.64$ Oe) (Bao *et al.*, 2003; Jiang *et al.*, 2013). But, Wang *et al.* (2010) reported that magnetic alginate-chitosan beads had superparamagnetic property (hysteresis was not observed).



Figure 3.23 Digital image of magnetic alginate-layered double hydroxide composites.

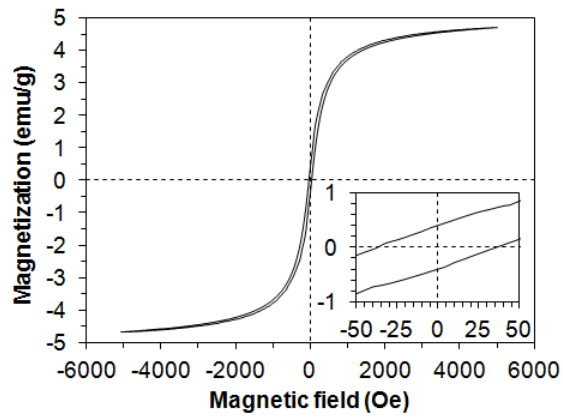


Figure 3.24 Magnetic hysteresis curves for magnetic alginate-layered double hydroxide composites.

Chapter 4 Selenate and Selenite Removal by Carbon Nanotube/ Iron Oxide Magnetic Nanocomposites

The objective of this study was to investigate the selenium removal using carbon nanotube/iron oxide magnetic nanocomposites. The magnetic nanocomposites were prepared by coprecipitation of magnetic iron oxide nanoparticles on oxidized carbon nanotube (multiwall). Results showed that the magnetic nanocomposites were effective in the removal of selenium with the sorption capacity of 8.12 mg/g for Se(IV) and 3.82 mg/g for Se(VI) under given experimental conditions (dose = 1 g/L; initial selenium concentration = 10 mg/L; reaction time = 240 min). Compared to magnetic nanocomposites, oxidized carbon nanotube has little sorption capacity for selenium. In the magnetic nanocomposites, oxidized carbon nanotube played supporting material to prevent aggregation of magnetic iron oxide nanoparticles and to easily separate from water. The maximum sorption capacity of magnetic nanocomposites were determined to be 14.521 mg/g for Se(IV) and 6.470 mg/g for Se(VI). In addition, selenium removal was clearly affected by initial solution pH. From the XPS study, Se(IV) and Se(VI) were reduced on the surface of magnetic nanocomposites with oxidation of iron. This study demonstrated that carbon nanotube/iron oxide magnetic nanocomposites could be used for selenium removal.

4.1. Materials and Methods

4.1.1. Selenium removal experiments

The desired concentration of Se(IV) and Se(VI) were prepared by diluting the stock solution (1,000 mg/L), which were made from sodium selenite (Na_2SeO_3 , 99%, Sigma-Aldrich, USA) and sodium

selenate (Na_2SeO_4 , $\geq 95\%$, Sigma-Aldrich, USA). Batch experiments were performed in 50 mL polypropylene conical tubes containing 1.0 g/L of magnetic nanocomposites (0.03 g) and diluted selenium solution (30 ml). The tubes were shaken at 30°C and 100 rpm using a shaking incubator (Daihan Science, Korea). Then, the magnetic nanocomposites were separated from the solution through a 0.45 μm cellulose filter after desired reaction time. The residual selenium concentration was measured by inductively coupled plasma-atomic emission spectroscopy (ICP-AES) (Optima-4300, PerkinElmer, USA).

Batch experiments were performed at different reaction times (selenium concentration = 10 mg/L, solution pH = 4.0). In the experiments, samples were taken at 15, 30, 45, 60, 120, 180, and 240 min after reaction. To examine the effect of temperature on selenium removal, the same procedures were followed at 15 and 45°C. Further batch experiments were conducted at different concentrations of selenium solution (initial selenium concentration = 5 - 120 mg/L, solution pH = 4.0). The samples were collected 6 h post-reaction. The effects of solution pH on selenium removal were investigated in 10 mg/L selenium solution during 6 h. The pH of solution was adjusted using 0.1 M NaOH or 0.1 M HCl. The solution pH was measured with a pH probe (9107BN, Thermo Scientific, USA). All experiments were performed in triplicate.

4.1.2. XPS analysis

X-ray photoelectron spectroscopy (XPS) was a surface-sensitive quantitative spectroscopic technique that provided unique information

about chemical composition and chemical state of a surface. XPS was also commonly named as ESCA (Electron Spectroscopy for Chemical Analysis) by Siegbahn's research group (1967) in university of Uppsala (Sweden). The principle of XPS was as follows. Sufficiently large energy of X-ray beam directs to the sample surface, the electron was escaped from the atom and emitted out of the surface. The photoelectron with kinetic energy emitted from the sample was measured for calculation of binding energy. Binding energy was unique properties of photoelectrons emitted atoms, which enables element analysis can be performed. The binding energy of each of the emitted electrons can be determined by the Einstein relationship:

$$E_b = h\nu - E_k - e\phi_{sp} \quad (1)$$

where E_b is the binding energy (BE) of the electron, $h\nu$ is the energy of the X-ray beam (for Mg Ka, $h\nu = 1253.6\text{eV}$), E_k is the kinetic energy of the electron as measured by the instrument and $e\phi_{sp}$ is the work function of the spectrometer (not the material). The schematic diagram of photoelectrons effects of Einstein relationship was shown in Figure 4.1.

A typical XPS spectrum is a plot of the binding energy of the electrons detected (X-axis, abscissa) versus the number of electrons detected (a.u., arbitrary unit) (Y-axis, ordinate). Right end of the abscissa axis represents zero binding energy and go up to slightly lower than the photon energy of 1,000 eV at left end. Such a wide range of

spectrum was shown in Figure 3.11 (a). C1s peak (284.6 eV) was used to calibrate the binding energy of other elements peaks. The high resolution spectrum (Figure 3.11 (b) or Figure 4.6 (a), (b)) was obtained to cumulate several times of narrow spectrum at specific peaks. The binding energy peaks was changed depending on the oxidation state. The binding energy was increased with decreasing electron density at oxidation process. This allows the chemical information of atom could be obtained.

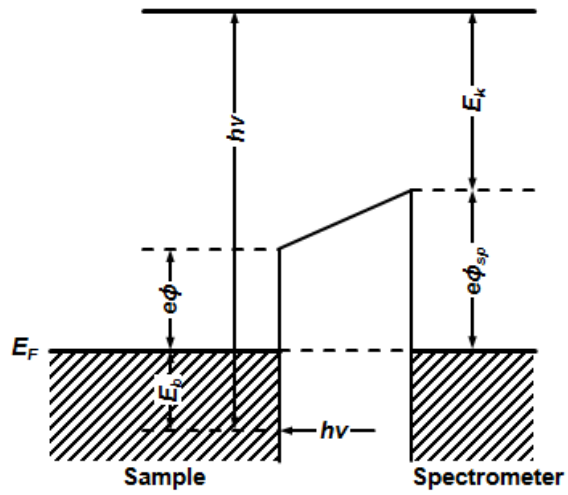


Figure 4.1 Schematic diagram of Einstein relationship (modified from Lee and Boo (1990)).

4.1.3. Data analysis

The experimental data obtained as a function of reaction time were analyzed using the pseudo first-order (eq. 2), pseudo second-order (eq. 3), and Elovich (eq. 4) kinetic models (Gupta and Bhattacharyya, 2011):

$$q_t = q_e (1 - e^{-k_1 t}) \quad (2)$$

$$q_t = \frac{k_2 q_e^2 t}{1 + k_2 q_e t} \quad (3)$$

$$q_t = \frac{1}{\beta} \ln(\alpha\beta) + \frac{1}{\beta} \ln t \quad (4)$$

where q_e is the amount of selenium adsorbed (adsorption capacity) at equilibrium, q_t is the amount of selenium adsorbed (adsorption capacity) at time t , k_1 is the pseudo first-order rate constant, k_2 is the pseudo second-order rate constant, α is the initial adsorption rate constant, and β is the Elovich adsorption constant. The rate constant k_2 was used to calculate the initial adsorption rate constant (h) at $t \rightarrow 0$ with the following equation :

$$h = k_2 q_e^2 \quad (5)$$

In addition, the kinetic data were analyzed with the following intra-particle diffusion model (Weber-Morris equation) (Bajpai and Armo,

2009):

$$q_t = k_i t^{1/2} + I \quad (6)$$

where k_i is the intra-particle diffusion rate constant and I is the intercept related to the thickness of the boundary layer.

The experimental data obtained as a function of initial adsorbate concentration were analyzed with the Freundlich (eq. 7), Langmuir (eq. 8), and Redlich-Peterson (eq. 9) isotherm models (Foo and Hameed, 2010):

$$q_e = K_F C_e^{1/n} \quad (7)$$

$$q_e = \frac{Q_m K_L C_e}{1 + K_L C_e} \quad (8)$$

$$q_e = \frac{K_R C_e}{1 + a_R C_e^g} \quad (9)$$

where C_e is the equilibrium concentration of adsorbate in the aqueous solution, K_F is the Freundlich constant related to the adsorption capacity, $1/n$ is the Freundlich constant related to the adsorption intensity, Q_m is the maximum adsorption capacity, K_L is the Langmuir constant related to the affinity of the binding sites, K_R is the Redlich-Peterson constant related to the adsorption capacity, a_R is the Redlich-Peterson constant related to the affinity of the binding sites, and g is the Redlich-Peterson

constant related to the adsorption intensity. K_F and $1/n$ were used to calculate the maximum adsorption capacity q_m with the following equation (Halsey, 1948):

$$q_m = K_F C_0^{1/n} \quad (10)$$

where C_0 is the initial concentration of adsorbate in the aqueous solution.

The experimental data obtained as a function of different temperatures were analyzed to determine thermodynamic parameters using the following equations (Goswami and Purkait, 2011):

$$\Delta G^0 = \Delta H^0 - T\Delta S^0 \quad (11)$$

$$\ln(K_e) = \frac{\Delta S^0}{R} - \frac{\Delta H^0}{RT}; K_e = \frac{aq_e}{C_e} \quad (12)$$

where ΔG^0 is the change in Gibb's free energy, ΔS^0 is the change in entropy, ΔH^0 is the change in enthalpy, K_e is the equilibrium constant (dimensionless), and a is the adsorbent dose (g /L). Values of ΔS^0 and ΔH^0 were determined by plotting $\ln(K_e)$ versus $1/T$ using Eq. (12), and then value of ΔG^0 was calculated from Eq. (11).

Model parameters were estimated by nonlinear regression using MS Excel 2010 with solver add in program. The determined coefficient (R^2) and the chi-square coefficient (χ^2) were used to analyze the data and

confirm the fit to the model. The expressions of R^2 and χ^2 were given below:

$$R^2 = \frac{\sum_{i=1}^m (y_c - \bar{y}_e)_i^2}{\sum_{i=1}^m (y_c - \bar{y}_e)_i^2 + \sum_{i=1}^m (y_c - y_e)_i^2} \quad (13)$$

$$\chi^2 = \sum_{i=1}^m \left\{ \frac{(y_e - y_c)^2}{y_c} \right\}_i \quad (14)$$

4.2. Results and Discussion

4.2.1. Characteristics of selenium sorption

The effect of reaction time (selenium concentration = 10 mg/L, solution pH = 4.0) on the removal of selenium by carbon nanotube/iron oxide magnetic nanocomposites and oxidized carbon nanotube were presented in Figure 4.1 (a) (Se(IV)) and (b) (Se(VI)). In case of magnetic nanocomposites, the sorption capacity increased gradually with increasing reaction time until the equilibrium was reached. At 30°C, the sorption capacity of Se(IV) augmented to 6.81 mg/g at 30 min of reaction time and further increased to 8.12 mg/g at 240 min. The Se(VI) sorption capacity was 3.68 mg/g at 30 min and slightly increased to 3.82 mg/g at 240 min. Meanwhile, the sorption capacity of oxidized carbon nanotube was 1.52 mg/g for Se(IV) and 1.14 mg/g for Se(VI) at 240 min of reaction time.

The selenium removal by the carbon nanotube/iron oxide magnetic nanocomposites as a function of initial selenium concentrations (reaction time = 6 h, solution pH = 4.0) were provided in Figure 4.1 (c). Selenium removal was more sensitive at lower concentration than higher concentration. At the lowest concentration of 5.73 mg/L, the sorption capacity of Se(IV) was 5.37 mg/g. The sorption capacity increased to 11.59 mg/g at the Se(IV) concentration of 23.23 mg/L and further increased to 14.37 mg/g at the highest concentration of 116.78 mg/L. Meanwhile, the sorption capacity of Se(VI) increased from 3.40 to 6.47 mg/g with increasing Se(VI) concentrations from 6.33 to 122.54 mg/L. At lower concentrations, the selenium ions available in the

solution are fewer in number than the sorption sites on the magnetic nanocomposites, but there are fewer sorption sites at higher selenium concentrations.

The effect of solution pH (selenium concentration = 10 mg/L, reaction time = 6 h) on the removal capacity of Se(IV) and Se(VI) by carbon nanotube/iron oxide magnetic nanocomposites were presented in Figure 4.1 (d). Selenium removal by magnetic nanocomposites was clearly affected by the solution pH. In the adsorption of Se(IV) to magnetic nanocomposites, the removal capacity remained relatively constant, above 9.0 mg/g for 1.81-4.01 and then dropped gradually to 4.65 mg/g at pH 7.11. In the adsorption of Se(VI) to magnetic nanocomposites, the removal capacity dropped gradually from 6.09 mg/g to 0.11 mg/g between pH 1.88 and 7.01. For the same pH conditions, the removal capacity of Se(IV) was greater than Se(VI) by magnetic nanocomposites. These results were good agreement can be observed at nano-sized magnetite, but not in agreement at nano iron (Wei *et al.*, 2012).

The pH dependency of adsorption of Se(IV) and Se(VI) to magnetic nanocomposites were primarily related to ionization of selenium in accordance with pH change. The speciation of Se(IV) in the pH range between 2.63 and 8.36, HSeO_3^- (monovalent anion) is dominant. As shown in Figure 3.6, the point of zero charge (pH_{pzc}) nanocomposites was around 5.1. Below the pH_{pzc} , the nanocomposites was positively charged and therefore, the adsorption of Se(IV) was favorable via electrostatic attractions. Above the pH_{pzc} , the nanocomposites became more negatively charged with increasing pH and therefore, the

adsorption of Se(IV) became more unfavorable due to electrostatic repulsion. H_2SeO_3 (uncharged form) dominates at $\text{pH} < 2.63$, and the adsorption of this species to magnetic nanocomposites may occur as inner-sphere bidentate surface complexes, $=\text{Fe}_2\text{SeO}_3$, $=\text{FeOHSeO}_3^{2-}$ and $=\text{FeHSeO}_3$, with magnetite or goethite (Balistreri and Chao, 1990; Loyo *et al.*, 2008; Martinez *et al.*, 2006). The speciation of Se(VI) is also influenced by the solution pH. Divalent anion (SeO_4^{2-}) is dominant at $\text{pH} > 1.61$. The adsorption of Se(VI) to magnetite was occur as outer-sphere hydrated complex, $=\text{FeOH}_2^+ - \text{SeO}_4^{2-}$ (Martinez *et al.*, 2006; Kim *et al.*, 2012). The weakly bonded outer-sphere complex of Se(VI) in addition to increased competitiveness between OH^- and selenium anions for the adsorption site with increasing pH, could explain the decrease adsorption capacity.

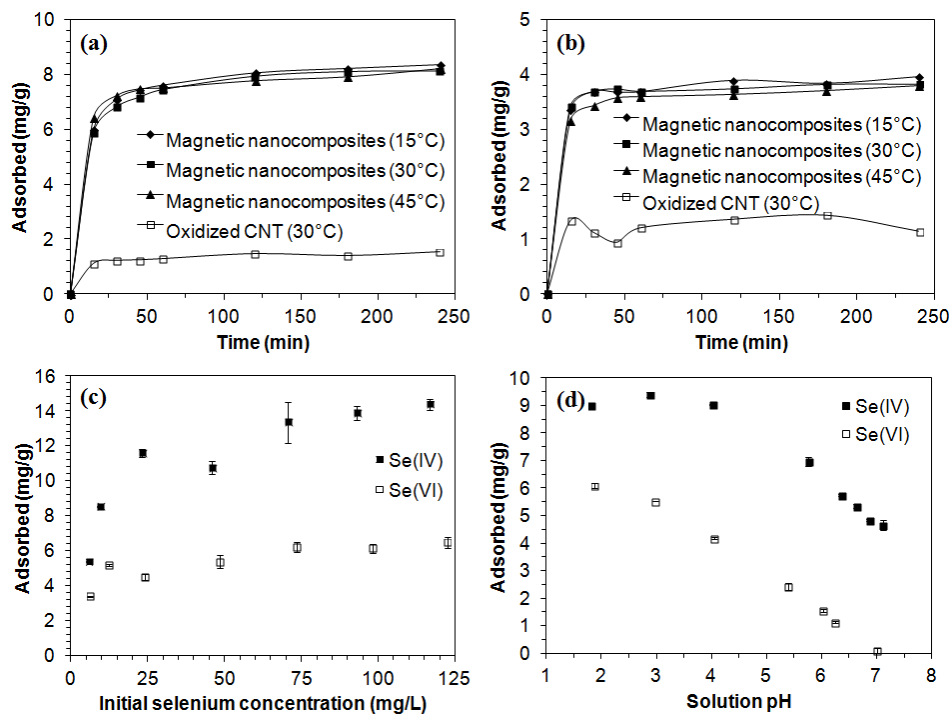


Figure 4.2 Selenium adsorption to magnetic nanocomposites: (a) effect of reaction time for Se(IV); (b) effect of reaction time for Se(VI); (c) effect of initial selenium concentration; (d) effect of solution pH.

4.2.2. Adsorption kinetic, isotherm and thermodynamic analysis

The kinetic model analysis were presented in Figure 4.2. The kinetic model parameters for the pseudo first-order, pseudo second-order, and Elovich models were provided in Table 4.1. The coefficient of determination (R^2) and the value of Chi-square (χ^2) indicates that the pseudo second-order model (Figure 4.2) was most suitable at describing the kinetic data. This indicates that chemisorption is involved in the adsorption of selenium to carbon nanotube/iron oxide magnetic nanocomposites. In the pseudo second-order model parameters (Table 4.1), values of q_e decreased with increasing temperature, demonstrating that the selenium adsorption capacity decreased with increasing temperature both selenite(IV) and selenate(VI).

The intra-particle diffusion model applied to the data is shown in Figure 4.3, indicating that the plots were composed of two line segments. The first line in the plot indicates boundary layer adsorption, while the second line describes the intra-particle diffusion (Bajpai and Armo, 2009). The Intra-particle diffusion model parameters are provided in Table 4.2. The diffusion rate constant (k_i) and intercept value (I) for Se(IV) were superior to the values for Se(VI).

The equilibrium isotherms of selenium in the carbon nanotube/iron oxide magnetic nanocomposites were illustrated in Figure 4.4. Equilibrium isotherm constants were summarized in Table 4.3. The correlation coefficients (R^2) and the value of Chi-square (χ^2) indicated that Redlich–Peterson isotherms was most suitable at describing the

equilibrium data. The value of K_R/a_R in the Redlich–Peterson model for Se(IV) and Se(VI) were 9.872 mg/g and 4.068 mg/g, respectively. The adsorption capacity of Freundlich model (q_m) was calculated from the values of K_F and $1/n$ using equation (9). The values of q_m were 14.521 mg/g for Se(IV) and 6.470 mg/g for Se(VI), while the maximum adsorption capacity of Langmuir model (Q_m) were 13.080 mg/g for Se(IV) and 6.130 mg/g for Se(VI). The maximum adsorption capacity determined from our experiments was in the range of selenate(VI) removal capacity of Fe-loaded activated carbon (2.3 ~ 21.0 mg/g) reported by Dobrowolski and Otto (2013), or superior to the range of selenite(IV) removal capacity of iron-coated GAC (2.53 ~ 2.89 mg/g) reported by Zhang *et al.* (2008).

The thermodynamic analysis for selenium sorption to magnetic nanocomposites was presented in Figure 4.5. The thermodynamic parameters were provided in Table 4.4. The selenium adsorption to magnetic nanoparticles decreased with increasing temperature from 15 to 45 °C (Figure 4.1 (a) Se(IV) and (b) Se(VI)), demonstrating that the sorption process were exothermic. The negative value of ΔH^0 (−6.921 kJ/mol for Se(IV) and −1.599 kJ/mol for Se(VI)) indicates the exothermic nature of selenium sorption. The negative value of ΔS^0 (−9.474 J/K mol for Se(IV) and −9.178 J/K mol for Se(VI)) indicates that the randomness decreased at the interface between solid and solution during the sorption process. The negative values of ΔG^0 (−3.907 ~ −4.191 kJ/mol) indicate that the selenite(IV) sorption process was spontaneous. These results (negative value of ΔH^0 , negative value of ΔS^0 , negative values of ΔG^0) conform well with the

reports of other researchers who examined the Se(IV) sorption on nano-TiO₂ (Zhang *et al.*, 2009) or on green algae biomass (Tuzen and Sari, 2010). But, the positive values of ΔG^0 (1.046 ~ 1.321 kJ/mol) indicate that the selenite(VI) sorption process was unfavorable and less feasible. This results (negative value of ΔH^0 , negative value of ΔS^0 , positive values of ΔG^0) were good agreement with other research of Se(VI) sorption onto anatase (Jordan *et al.*, 2013).

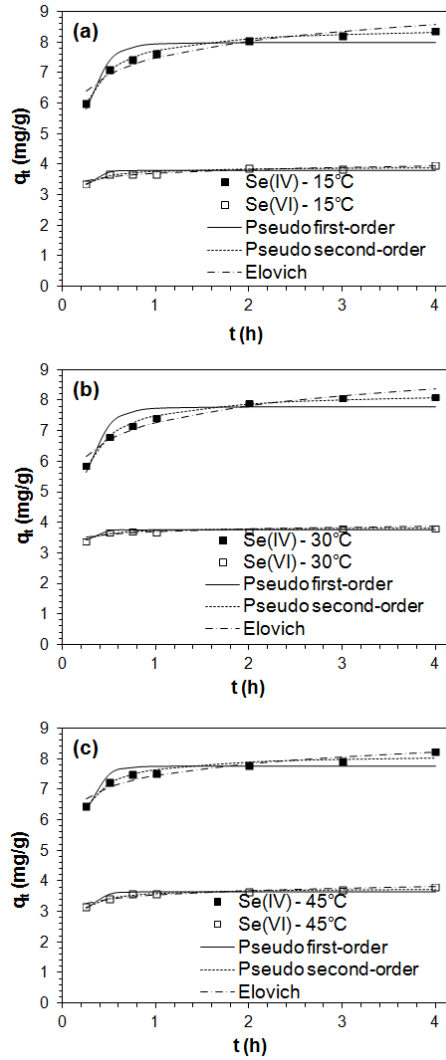


Figure 4.3 Kinetic model fits for selenate and selenite removal in the magnetic nanocomposites at various temperatures: (a) 15°C; (b) 30°C; (c) 45°C.

Table 4.1 Kinetic model parameters obtained from model fitting to experimental data

Pseudo first-order model	Temp. (°C)	q _e (mg/g)	k ₁ (/h)	R ²	χ ²	
Se(IV)	15	7.987	5.209	0.860	0.074	
	30	7.776	5.156	0.821	0.099	
	45	7.771	6.761	0.786	0.055	
Se(VI)	15	3.799	8.397	0.725	0.017	
	30	3.757	9.483	0.873	0.004	
	45	3.640	7.725	0.802	0.015	
Pseudo second-order model	Temp. (°C)	q _e (mg/g)	k ₂ (g/mg/h)	h (mg/g/h)	R ²	χ ²
Se(IV)	15	8.525	1.122	81.524	0.995	0.002
	30	8.315	1.117	77.211	0.993	0.004
	45	8.149	1.838	122.041	0.962	0.009
Se(VI)	15	3.928	5.947	91.745	0.906	0.006
	30	3.843	8.902	131.480	0.918	0.003
	45	3.779	5.283	75.442	0.971	0.002
Elovich kinetic model	Temp. (°C)	α (mg/g/h)	β (g/mg)	R ²	χ ²	
Se(IV)	15	1.03E+04	1.269	0.927	0.042	
	30	7.43E+03	1.260	0.946	0.030	
	45	3.74E+05	1.801	0.922	0.022	
Se(VI)	15	9.42E+07	5.417	0.869	0.009	
	30	3.99E+11	7.801	0.763	0.008	
	45	1.09E+07	5.050	0.891	0.008	

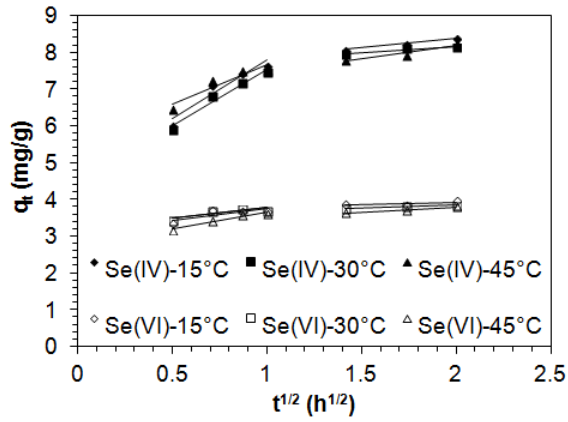


Figure 4.4 Intra-particle diffusion model for selenate and selenite removal in the magnetic nanocomposites.

Table 4.2 Intra-particle diffusion model parameters obtained from model fitting to experimental data

Temperature		$k_{i,1}$ (mg/g/h ^{0.5})	I	R ²	$k_{i,2}$ (mg/g/h ^{0.5})	I	R ²
	15°C	3.239	4.565	0.913	0.512	7.352	1.000
Se(IV)	30°C	3.105	4.438	0.959	0.335	7.475	0.875
	45°C	2.177	5.499	0.871	0.743	6.701	0.935
	15°C	0.623	3.118	0.674	0.104	3.711	0.252
Se(VI)	30°C	0.576	3.19	0.704	0.148	3.54	0.822
	45°C	0.908	2.737	0.928	0.269	3.246	0.984

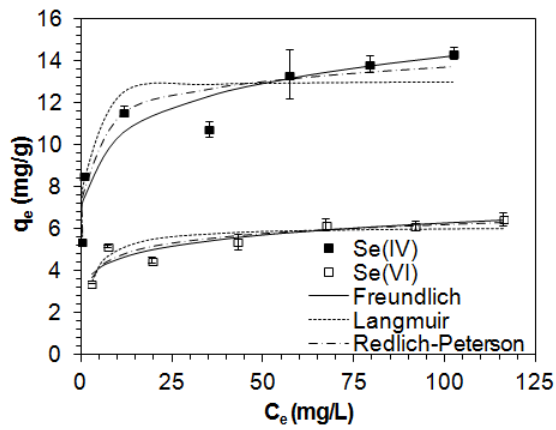


Figure 4.5 Equilibrium isotherm model fits for selenate and selenite removal in the magnetic nanocomposites.

Table 4.3 Equilibrium isotherm model parameters obtained from model fitting to experimental data

Freundlich	K_F	$1/n$	q_m	R^2	χ^2	
	(L/g)		(mg/g)			
Se(IV)	7.573	0.137	14.521	0.904	0.671	
Se(VI)	3.298	0.140	6.470	0.829	0.274	
Langmuir	Q_m	K_L	R^2	χ^2		
	(mg/g)	(L/mg)				
Se(IV)	13.080	1.962	0.870	0.641		
Se(VI)	6.130	0.444	0.754	0.323		
Redlich-Peterson	K_R	a_R	K_R/a_R	g	R^2	χ^2
	(L/g)	(L/mg)	(mg/g)			
Se(IV)	43.248	4.381	9.872	0.928	0.923	0.417
Se(VI)	6.608	1.624	4.068	0.906	0.831	0.253

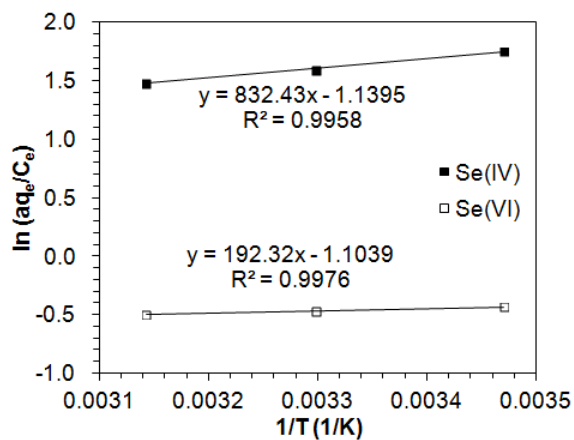


Figure 4.6 Thermodynamic analyses for selenate and selenite removal in the magnetic nanocomposites.

Table 4.4 Thermodynamic parameters for selenium adsorption to carbon nanotube/iron oxide magnetic nanocomposites

	Temperature (°C)	ΔH° (kJ/mol)	ΔS° (J/K mol)	ΔG° (kJ/mol)
Se(IV)	15	-6.921	-9.474	-4.191
	30			-4.049
	45			-3.907
Se(VI)	15	-1.599	-9.178	1.046
	30			1.183
	45			1.321

4.2.3. XPS analysis for selenium adsorption

The surface of the carbon nanotube/iron oxide magnetic nanocomposites was analyzed by XPS to determine the oxidation state of selenium on the sample surfaces. When analyzing selenium on iron compounds by this technique, the spectrum of iron can cause interference in the selenium spectrum. Thus, several researchers chose the Se 3d peaks to deconvolute the spectrum (Briggs and Seah, 1983; NIST, 2013; Volynsky *et al.*, 2001; Naveau *et al.*, 2007). Literature data of Se 3d binding energy for selenium species were presented in Table 4.5. Metallic selenide (-II) compounds peaks are generally found under 56 eV, whereas elemental selenium observed between 54.6 ~ 57.5 eV. Selenite(IV) species and selenate(VI) species were appeared above 58 eV. High-resolution spectra of Se 3d on magnetic nanocomposites were presented in Figure 4.6 (a). After reaction with Se(IV) or Se(VI), the binding energy were centered at 56.313 eV and 56.372 eV, respectively. Based on the literature data, these values are close to the elemental selenium. It means that Se(IV) and Se(VI) were reduced on the surface of magnetic nanocomposites. Several researchers have demonstrated that Se(IV) is reduced by FeS through intermediates such as Se (0) to less soluble species such as Se(-II) (Naveau *et al.*, 2007; Han *et al.*, 2013). Sasaki *et al.* (2008) observed that Se(VI) was reduced to iron selenide (FeSe) on surface of column containing zero valence iron (ZVI). In particular, selenite(IV) and selenate(VI) was rapidly reduced by iron nanoparticle like nZVI, mackinawite, and magnetite than green rust or Fe(II) beared montmorillonite (Charlet *et al.*, 2007; Scheinost and Charlet, 2008; Hayashi *et al.*, 2009; Olegario *et al.*, 2010). Beside,

the high-resolution spectra of Fe 2p in Figure 4.6 (b) showed that oxidation of iron on magnetic nanocomposites surface after reaction with selenium. Before the reaction, binding energy of Fe 2p was centered at 711.115 eV. After the reaction with Se(IV) or Se(VI) the Fe 2p peaks was shift to 711.463 eV and 711.222 eV, respectively.

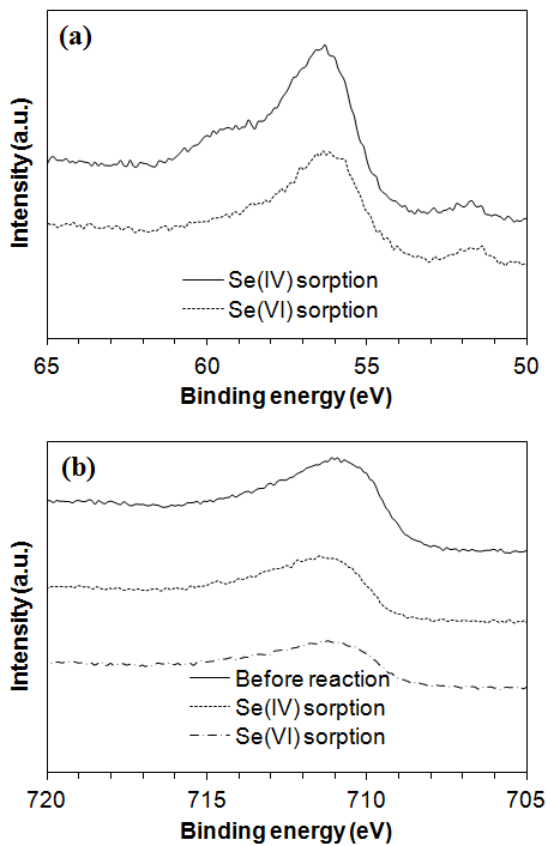


Figure 4.7 XPS spectra of selenium adsorbed on carbon nanotube/iron oxide magnetic nanocomposites surface: (a) Se 3d_{5/2} spectra; (b) Fe 2p_{3/2} spectra.

Table 4.5 Binding energies of Se 3d_{5/2} XPS spectra

Sample	B.E. (eV)	Reference
FeSe	54.8	Naveau (2007)
	55.8	NIST (2013)
Se	54.6–57.5	NIST (2013)
	55.5–56.3	Briggs (1983)
	56.1	Volynsky (2001)
SeO ₂	59	Briggs (1983)
	58.8–59.9	NIST (2013)
H ₂ SeO ₃	59.2	Briggs (1983)
	59.0–59.9	NIST (2013)
H ₂ SeO ₄	61.2	Briggs (1983)
	61	NIST (2013)
Na ₂ SeO ₃	58.2	Naveau (2007)
	58.5	Briggs (1983)
	59.1	NIST (2013)
	58.7–59.9	Volynsky (2001)
Na ₂ SeO ₄	60.6	Briggs (1983)
	61.6	NIST (2013)
Pyrite + Se(-II)	54.8	Naveau (2007)
Pyrite + Se(IV)	54.8	Naveau (2007)
Chalcopyrite + Se(-II)	54.8	Naveau (2007)
Chalcopyrite + Se(IV)	54.8	Naveau (2007)
Magnetic nanocomposites + Se(IV)	56.313	This study
Magnetic nanocomposites + Se(VI)	56.372	This study

**Chapter 5 Use of Carbon
Nanotube/Iron Oxide Magnetic
Nanocomposites for Removal of
Chromium in Aqueous Solution**

The objective of this study was to investigate the chromate removal using carbon nanotube/iron oxide magnetic nanocomposites. The magnetic nanocomposites were prepared by coprecipitation of magnetic iron oxide nanoparticles on oxidized carbon nanotube. Results showed that the magnetic nanocomposites were effective in the removal of chromate with the sorption capacity of 5.93 mg/g for chromate under given experimental conditions (dose = 1 g/L; initial concentration = 10 mg/L; reaction time = 240 min). Compared to magnetic nanocomposites, iron oxide nanoparticles and oxidized carbon nanotube has little sorption capacity for chromate. In the magnetic nanocomposites, oxidized carbon nanotube played supporting material to prevent aggregation of magnetic iron oxide nanoparticles and to easily separate from water. This indicated that the magnetic iron oxide nanoparticles in the magnetic nanocomposites were provided not only magnetic properties for easily separation but also improve sorption capacity. The maximum sorption capacity of magnetic nanocomposites were determined to be 12.849 mg/g and chromate removal was clearly affected by initial solution pH. The XPS results suggest that there is no change in the valence of the chromium undergoing adsorption. The sequential extraction of chromate from magnetic nanocomposites indicated that 57.82% of chromate bounded to iron oxide. This study demonstrated that carbon nanotube/iron oxide magnetic nanocomposites could be used for chromate removal.

5.1. Materials and Methods

5.1.1. Chromate removal experiments

The desired Cr(VI) concentration was prepared by diluting the stock Cr(VI) solution (1,000 mg/L), which was made from potassium dichromate ($K_2Cr_2O_7$). Batch experiments were performed in 50 mL polypropylene conical tubes containing 1.0 g/L of carbon nanotube/iron oxide magnetic nanocomposites. The tubes were shaken at 30 °C and 100 rpm using a shaking incubator (Daihan Science, Korea). Then, the magnetic nanocomposites were separated from the solution through a 0.45 μ m cellulose filter after desired reaction time. The residual Cr(VI) concentration was measured by UV–vis spectrophotometer (Helios, Thermo, USA) using diphenylcarbazide method. The oxidation states of chromium on the surface of the magnetic nanocomposites were analyzed by X-ray photo-electron spectroscopy (XPS Sigma Probe, Thermo VG, UK).

Batch experiments were performed at different reaction times (Cr(VI) concentration = 10 mg/L, solution pH = 3.0). In the experiments, samples were taken at 15, 30, 45, 60, 120, 180, and 240 min after reaction. To examine the effect of temperature on selenium removal, the same procedures were followed at 15 and 45 °C. Further batch experiments were conducted at different concentrations of Cr(VI) solution (initial Cr(VI) concentration = 5 - 100 mg/L, solution pH = 3.0). The samples were collected 6 h post-reaction. The effects of solution pH on Cr(VI) removal were investigated in 10 mg/L Cr(VI) solution during 6 h. The pH of solution was adjusted using 0.1 M NaOH or 0.1 M HCl. The solution pH was measured with a pH probe

(9107BN, Thermo Scientific, USA). All experiments were performed in triplicate.

5.1.2. Sequential extraction

Sequential extraction experiments were conducted to investigate the distribution of Cr(VI) on the carbon nanotube/iron oxide magnetic nanocomposites and to evaluate qualitative binding force of Cr(VI) on the magnetic nanocomposites. Bielicka *et al.* (2005) established a sequential extraction procedure suitable for chromium based on the methods proposed by Tessier *et al.* (1979). A detailed description of the sequential extraction procedure used in this study was given below.

- (i) Exchangeable. The sample was extracted at room temperature for 1 h with 10 mL of magnesium chloride solution (0.5 M MgCl₂, pH 7.0) with continuous agitation (125 rpm).
- (ii) Bound to carbonates. The residue from (i) was leached at room temperature with 10 mL of 1 M NaOAc adjusted to pH 5.0 with acetic acid (HOAc). Continuous agitation was maintained 5 h with 125 rpm.
- (iii) Bound to Fe-Mn oxides. The residue from (ii) was extracted with 20 mL of 0.04 M NH₂OH-HCl in 25% (v/v) HOAc. The latter experiments were performed at 95°C with occasional agitation during 6 h.
- (iv) Bound to organic matter. The residue from (iii) were added 3 mL of 0.02 M HNO₃ and 5 mL of 30% H₂O₂ adjusted to

pH 2 with HNO₃, and the mixture was heated to 85°C for 2 h with occasional agitation. A second 3-mL aliquot of 30% H₂O₂ (pH 2 with HNO₃) was then added and the sample was heated again to 85°C for 3 h with intermittent agitation. After cooling, 5 mL of 3.2 M NH₄OAc in 20% (v/v) HNO₃ was added and the sample was diluted to 20 mL and agitated continuously for 30 min.

- (v) Residual. The residue from (iv) was digested with a HF-HClO₄ mixture according to the procedure described below for total metal analysis. The residue from (iv) were added 2.5 mL HNO₃ and 7.5 mL of HCl, and the mixture was heated to 75°C for 1 h. After heating, the sample was diluted to 10 mL with deionized water.

After each extraction, the suspension was centrifuged at 3,500 rpm and the supernatant solution was filtered through a 0.45 µm membrane filter paper. The slag residues were washed with deionized water, and then washing solution was carefully decanted and added to the each supernatant solution. This solution was analyzed for chromium by inductively coupled plasma-atomic emission spectroscopy (ICP-AES) (Optima-4300, PerkinElmer, USA). The resulting residue was dried for the next step. All experiments were performed in triplicate. Each extraction condition was summarized in Table 5.1.

Table 5.1 Scheme of sequential extraction

Fraction	Extractants	Operating conditions
F1: Exchangeable	10 ml of MgCl ₂ 0.5 mol/L (pH = 7)	1 h at 25°C
F2: Bound to Carbonates	10 ml of NaOAc 1 mol/L (pH = 5)	5 h at 25°C
F3: Bound to Fe-Mn Oxides	20 ml NH ₂ OH·HCl 0.04 mol/L in HOAc 25% w/w	6 h at 96°C
	3 ml HNO ₃ 0.02 mol/L + 5 ml H ₂ O ₂ 30% w/v (pH = 2)	2 h at 85°C
F4: Bound to Organic Matter	+ 3 ml H ₂ O ₂ 30% w/v (pH = 2)	3 h at 85°C
	+ 5 ml NH ₄ OAc 3.2 mol/L	30 min at 25°C
F5: Residual	2.5 ml HNO ₃ + 7.5 ml HCl	1 h at 70°C
	+ 10 ml H ₂ O	30 min at 25°C

5.2. Results and Discussion

5.2.1. Characteristics of chromate sorption

The characteristics of chromate sorption to the magnetic nanocomposites were shown in Figure 5.1. The effect of reaction time (initial concentration = 10 mg/L, solution pH = 3.0) on the removal of Cr(VI) by carbon nanotube/iron oxide magnetic nanocomposites, magnetic iron oxide nanoparticles, and oxidized carbon nanotube were presented in Figure 5.1 (a). The sorption capacity was increased gradually with increasing reaction time. In case of the magnetic nanocomposites, the sorption capacity augmented to 4.54 mg/g at 15 min of reaction time and further increased to 5.93 mg/g at 240 min. Meanwhile, the sorption capacity of oxidized carbon nanotube and magnetic iron oxide nanoparticles at 240 min of reaction time were 4.80 mg/g and 5.27 mg/g, respectively. This indicated that the magnetic iron oxide nanoparticles in the magnetic nanocomposites were provided not only magnetic properties for easily separation but also improve sorption capacity.

The Cr(VI) removal by the carbon nanotube/iron oxide magnetic nanocomposites as a function of initial chromate concentrations (reaction time = 6 h, solution pH = 3.0) were provided in Figure 5.1 (b). The percent removal decreased with increasing initial chromate concentration from 5 to 100 mg/L. At the lowest concentration of 5 mg/L, the percent removal was 80.8%. The percent removal decreased to 24.4% at the chromate concentration of 20 mg/L and further decreased to 12.6% at the highest concentration of 100 mg/L. Meanwhile, the sorption capacity increased from 4.04 to 12.61 mg/g

with increasing chromate concentrations from 5 to 100 mg/L.

The effect of reaction temperature on the removal of Cr(VI) by carbon nanotube/iron oxide magnetic nanocomposites were presented in Figure 5.1 (c). The sorption capacity was decreased with increasing reaction temperature. This results indicated that sorption of Cr(VI) onto carbon nanotube/iron oxide magnetic nanocomposites was an exothermic process. After 240 min of reaction, the sorption capacity for 15°C and 45°C were evaluated to be 6.20 mg/g and 5.96 mg/g, respectively.

The effect of solution pH (chromate concentration = 10 mg/L, reaction time = 6 h) on the removal capacity of Cr(VI) by carbon nanotube/iron oxide magnetic nanocomposites were presented in Figure 5.1 (d). Cr(VI) removal by magnetic nanocomposites was clearly affected by the solution pH. The sorption capacity at pH 2.58 was 5.57 mg/g and slightly increased to 5.70 mg/g at pH 2.97. Then, the sorption capacity dropped gradually from 5.07 mg/g to 2.13 mg/g between pH 3.77 and 7.28. This results indicated that Cr(VI) removal was relatively favorable at acidic solution pH. Similar findings were reported in the literature, including work by Hu *et al.* (2009), who showed that the maximum sorption of Cr(VI) by oxidized MWCNTs occurred at pH range around 2, and then the removal of Cr(VI) decreased with increasing pH. Chowdhury and Yanful (2010) showed that Cr(VI) removal by magnetite-maghemite nanoparticles had a tendency to gradual decrease from 85% to 0% as pH increased from 2 to 10.

Detailed XPS analysis was carried out to identify the chromium species on the surface of magnetic nanocomposites after adsorption.

The Cr(2p_{3/2}) spectra results in four peaks occurring at 576.52 eV, 577.40 eV, 578.66 eV, and 579.97 eV; FWHM were 1.16 eV, 1.16 eV, 1.51 eV, and 1.51 eV, respectively. The Cr(2p_{1/2}) peak centered at 586.4 eV, 9.1 eV above the midpoint of the Cr(2p_{3/2}) peaks, 577.3 eV. The photoelectron peak generated from Cr(VI) compounds has higher binding energies (~579 eV), sharper FWHM at ~2.1, and smaller 2p spin-orbit split (8.7~9.4 eV) than Cr(III) (Mullet *et al.*, 2004; Li *et al.*, 2008; Kim *et al.*, 2012). Thus, the XPS results suggest that there is no change in the valence of the chromium undergoing adsorption. Similar results were found in other research with Cr(VI) adsorption on δ -FeOOH coated maghemite nanoparticles (Hu *et al.*, 2007).

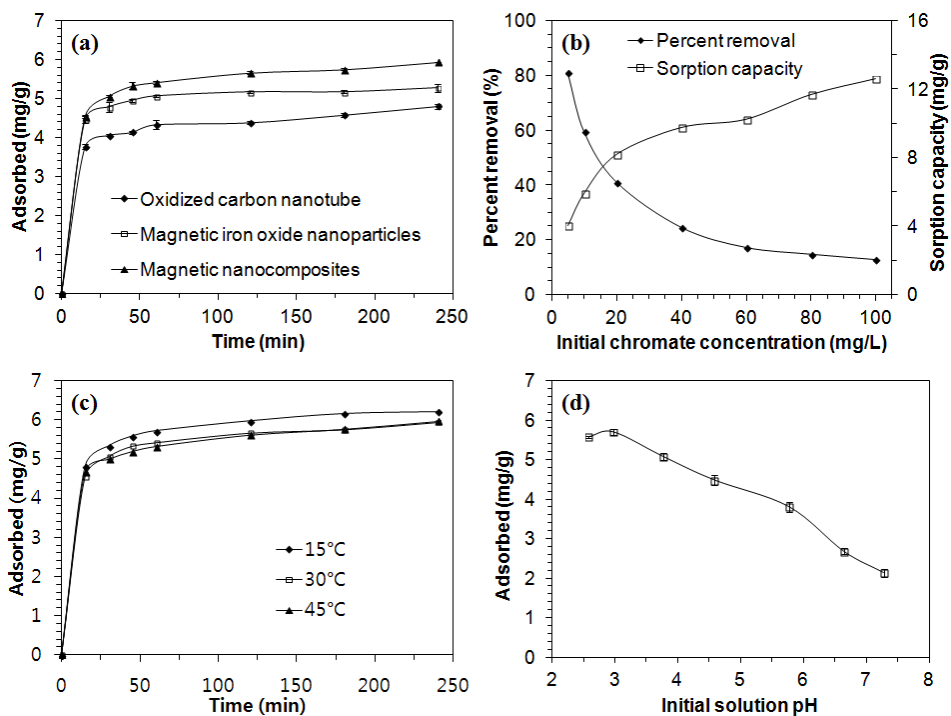


Figure 5.1 Cr(VI) adsorption to magnetic nanocomposites: (a) effect of reaction time; (b) effect of initial Cr(VI) concentration; (c) effect of reaction temperature; (d) effect of solution pH.

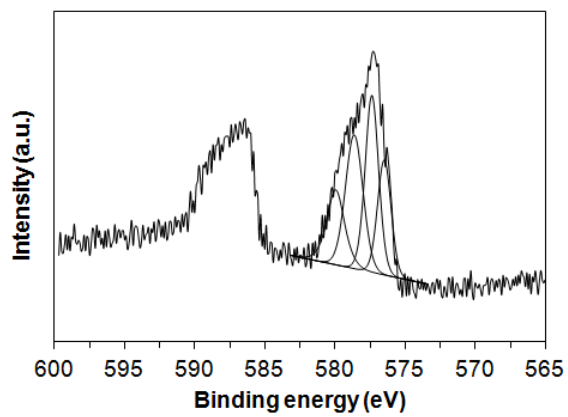


Figure 5.2 XPS spectra of Cr(VI) adsorbed on carbon nanotube/iron oxide magnetic nanocomposites surface.

5.2.2. Adsorption kinetic, isotherm and thermodynamic analysis

The kinetic model analysis were presented in Figure 5.3. The kinetic model parameters for the pseudo first-order, pseudo second-order, and Elovich models were provided in Table 5.2. The coefficient of determination (R^2) and the value of Chi-square (χ^2) indicates that both the pseudo second-order model and the Elovich model were more suitable at describing the kinetic data than the pseudo first-order model. This indicates that chemisorption is involved in the adsorption of chromate to carbon nanotube/iron oxide magnetic nanocomposites. The values of q_e from the pseudo second-order model was greater than that from the pseudo first-order model. In the pseudo second-order model parameters (Table 5.2), values of q_e decreased with increasing temperature, demonstrating that the selenium adsorption capacity decreased with increasing temperature. Also, in order the values of q_e at 30°C for magnetic nanocomposites was 5.919 mg/g, for iron oxide nanoparticles was 5.286 mg/g, and for oxidized carbon nanotube was 4.658 mg/g. The initial adsorption rate of pseudo second-order model (h) was 3~4 orders of magnitude lower than the values of α from the Elovich model.

The intra-particle diffusion model applied to the data is shown in Figure 5.4, indicating that the plots were composed of two line segments. The first line in the plot indicates boundary layer adsorption, while the second line describes the intra-particle diffusion (Bajpai and Armo, 2009). The Intra-particle diffusion model parameters are provided in Table 5.3.

The equilibrium isotherms of chromate in the carbon nanotube/iron oxide magnetic nanocomposites were illustrated in Figure 5.5. Equilibrium isotherm constants were summarized in Table 5.4. The coefficient of determination (R^2) and the value of Chi-square (χ^2) indicates that both the Redlich–Peterson isotherms and the Freundlich isotherms were more suitable at describing the equilibrium data than Langmuir isotherms. In the Redlich–Peterson model, the value of K_R/a_R was 4.751 mg/g and the value of g was 0.786. The adsorption capacity of Freundlich model (q_m) was 12.847 mg/g while the maximum adsorption capacity of Langmuir model (Q_m) was 11.256 mg/g. The maximum adsorption capacity determined from our experiments was superior to the range of Cr(VI) removal capacity of oxidized multiwalled carbon nanotubes (1.177 ~ 4.262 mg/g) reported by Hu *et al.* (2009).

The thermodynamic analysis for chromate sorption to magnetic nanocomposites was presented in Figure 5.6. The thermodynamic parameters were provided in Table 5.5. The chromate adsorption to magnetic nanoparticles decreased with increasing temperature from 15 to 45 °C (Figure 5.1 (c)), demonstrating that the sorption process were exothermic. The negative value of ΔH^0 (–6.635 kJ/mol) indicates the exothermic sorption. The negative value of ΔS^0 (–9.402 J/K mol) indicates that the randomness decreased at the interface between solid and solution during the sorption process. The negative values of ΔG^0 (–3.644 ~ –3.926 kJ/mol) indicate that the Cr(VI) sorption process was spontaneous. These results (negative value of ΔH^0 , negative value of ΔS^0 , negative values of ΔG^0) were good agreement with other other

researcher of Cr(VI) sorption on MnO₂ (Bhutani *et al.*, 1992).

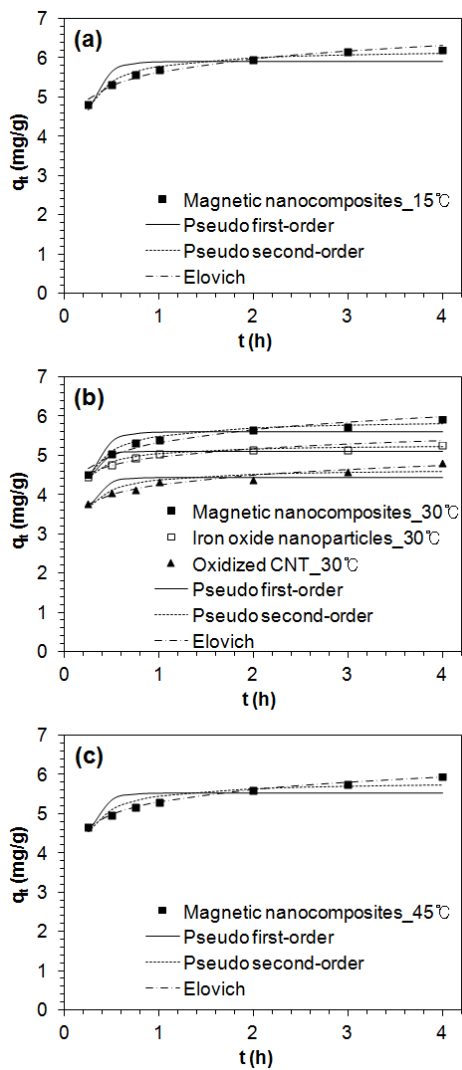


Figure 5.3 Kinetic model fits for chromate removal in the magnetic nanocomposites at various temperatures: (a) 15°C; (b) 30°C; (c) 45°C.

Table 5.2 Kinetic model parameters obtained from model fitting to experimental data

Pseudo first-order model	Temp. (°C)	q _e (mg/g)	k ₁ (/h)	R ²	χ ²	
Magnetic nanocomposites	15	5.910	6.248	0.746	0.066	
	30	5.603	6.197	0.768	0.058	
	45	5.536	6.854	0.570	0.097	
Iron oxide nanoparticles	30	5.097	7.989	0.760	0.023	
Oxidized CNTs	30	4.429	7.086	0.565	0.071	
Pseudo second-order model	Temp. (°C)	q _e (mg/g)	k ₂ (g/mg/h)	h (mg/g/h)	R ²	χ ²
Magnetic nanocomposites	15	6.245	2.017	78.661	0.980	0.005
	30	5.919	2.119	74.231	0.979	0.005
	45	5.841	2.378	81.137	0.900	0.023
Iron oxide nanoparticles	30	5.286	3.960	110.640	0.985	0.001
Oxidized CNTs	30	4.658	3.214	69.727	0.866	0.022
Elovich kinetic model	Temp. (°C)	α (mg/g/h)	β (g/mg)	R ²	χ ²	
Magnetic nanocomposites	15	4.27E+04	2.020	0.967	0.009	
	30	3.39E+04	2.096	0.956	0.012	
	45	4.59E+04	2.170	0.997	0.001	
Iron oxide nanoparticles	30	3.97E+06	3.314	0.913	0.010	
Oxidized CNTs	30	5.18E+04	2.794	0.960	0.007	

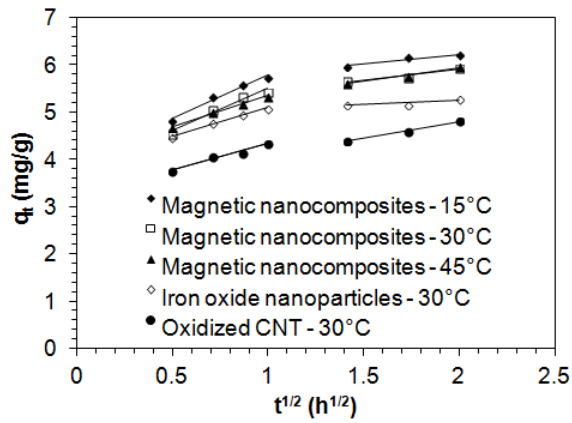


Figure 5.4 Intra-particle diffusion model for chromate removal in the magnetic nanocomposites, iron oxide nanoparticles, and oxidized carbon nanotubes.

Table 5.3 Intra-particle diffusion model parameters obtained from model fitting to experimental data

Sample/Temperature	$k_{i,1}$ (mg/g/h ^{0.5})	I	R ²	$k_{i,2}$ (mg/g/h ^{0.5})	I	R ²
15°C	1.829	3.955	0.966	0.406	5.415	0.924
Magnetic nanocomposites						
30°C	1.788	3.712	0.951	0.461	4.990	0.936
45°C	1.297	4.046	0.991	0.592	4.758	0.982
Iron oxide nanoparticles						
30°C	1.202	3.890	0.983	0.174	4.904	0.706
Oxidized CNTs						
30°C	1.086	3.240	0.971	0.711	3.370	0.992

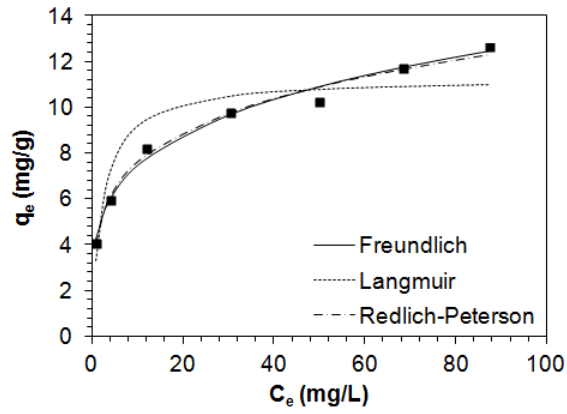


Figure 5.5 Equilibrium isotherm model fits for chromate removal in the magnetic nanocomposites.

Table 5.4 Equilibrium isotherm model parameters obtained from model fitting to experimental data

Freundlich model					
K_F (L/g)	$1/n$	q_m (mg/g)	R^2	χ^2	
4.254	0.240	12.847	0.987	0.079	
Langmuir model					
Q_m (mg/g)	K_L (L/mg)	R^2	χ^2		
11.256	0.430	0.867	0.913		
Redlich-Peterson model					
K_R (L/g)	a_R (L/mg)	K_R/a_R (mg/g)	g	R^2	χ^2
28.896	6.082	4.751	0.786	0.989	0.062

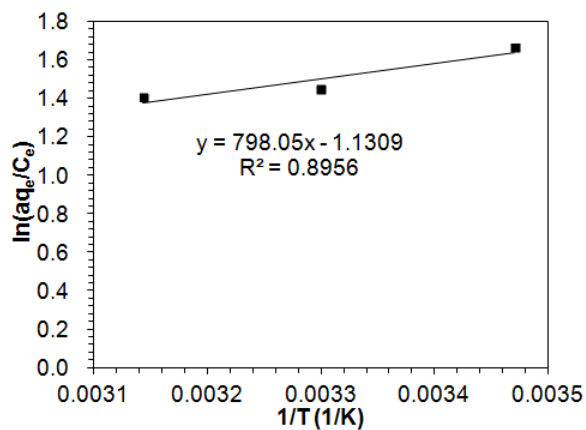


Figure 5.6 Thermodynamic analyses for chromate removal in the magnetic nanocomposites.

Table 5.5 Thermodynamic parameters for selenium adsorption to carbon nanotube/iron oxide magnetic nanocomposites

Temperature (°C)	ΔH° (kJ/mol)	ΔS° (J/K mol)	ΔG° (kJ/mol)
15	-6.63499	-9.4023	-3.92571
30			-3.78468
45			-3.64365

5.2.3. Chromate fractions in magnetic nanocomposites

An analytical procedure involving sequential chemical extractions has been developed for the partitioning of particulate trace metals into five fractions: exchangeable, bound to carbonates, bound to iron and manganese oxides, bound to organic matter, and residual (Tessier *et al.*, 1979). The quantities of chromate extracted with different extractants, with each chromate fraction expressed as a percentage of the sum of Cr(VI) contents in from F1 to F5 fractions were given in Figure 5.7. Analysis of contribution of particular fractions of chromate present in the samples has shown the predominant contribution of the fraction bound to iron and manganese oxides F3 (57.82%) and residual fraction F5 (23.38%). Its smaller amounts were determined bound to organic matter F4 (12.14%) and bound to carbonates F2 (6.45%). The exchangeable fraction contained only 0.21% of total chromate content in the magnetic nanocomposites. The accuracy proved to be satisfactory by comparing total trace metal concentrations with the sum of the five individual fractions.

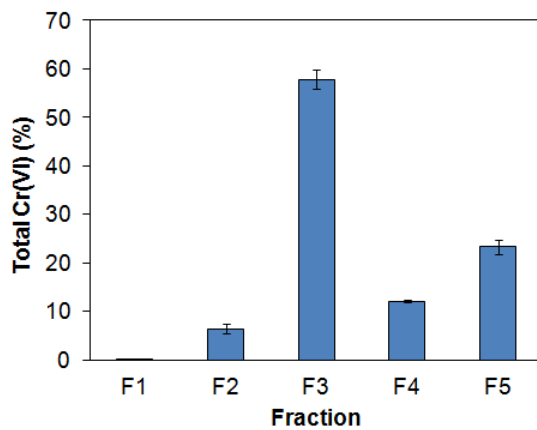


Figure 5.7 Cr(VI) distribution on the carbon nanotube/iron oxide magnetic nanocomposites by sequential extraction.

Chapter 6 Arsenate and Arsenite Removal by Carbon Nanotube/Iron Oxide Magnetic Nanocomposites

The objective of this study was to investigate the arsenic removal using carbon nanotube/iron oxide magnetic nanocomposites. The magnetic nanocomposites were prepared by coprecipitation of magnetic iron oxide nanoparticles on oxidized carbon nanotube (multiwall). Results showed that the magnetic nanocomposites were effective in the removal of arsenic with the sorption capacity of 7.10 mg/g for As(III) and 9.55 mg/g for As(V) under given experimental conditions (dose = 1 g/L; initial arsenic concentration = 10 mg/L; reaction time = 240 min). Compared to magnetic nanocomposites, arsenic adsorption capacity of oxidized carbon nanotubes was negligible. In the magnetic nanocomposites, oxidized carbon nanotube played supporting material to prevent aggregation of magnetic iron oxide nanoparticles and to easily separate from water. The maximum sorption capacity of magnetic nanocomposites were determined to be 19.54 mg/g for As(III) and 16.52 mg/g for As(V). In addition, arsenic removal was clearly affected by initial solution pH. This study demonstrated that carbon nanotube/iron oxide magnetic nanocomposites could be used for arsenic removal.

6.1. Materials and Methods

6.1.1. Arsenic removal experiments

The desired concentration of As(III) and As(V) were prepared by diluting the stock solution (1,000 mg/L), which were made from sodium arsenite (NaAsO_2 , 0.05M, Fluka Sigma-Aldrich, USA) and

sodium arsenate ($\text{Na}_2\text{HAsO}_4 \cdot 7\text{H}_2\text{O}$, 98-102%, Sigma-Aldrich, USA). Batch experiments were performed in 50 mL polypropylene conical tubes containing 1.0 g/L of magnetic nanocomposites (0.03 g) and diluted arsenite or arsenate solution (30 ml). The tubes were shaken at 30°C and 100 rpm using a shaking incubator (Daihan Science, Korea). Then, the magnetic nanocomposites were separated from the solution through a 0.45 μm cellulose filter after desired reaction time. The residual arsenic concentration was measured by inductively coupled plasma-atomic emission spectroscopy (ICP-AES) (Optima-4300, PerkinElmer, USA).

Batch experiments were performed at different reaction times (As(III): concentration = 10 mg/L, solution pH = 7.0; As(V): concentration = 10 mg/L, solution pH = 3.0). In the experiments, samples were taken at 15, 30, 45, 60, 120, 180, and 240 min after reaction. To examine the effect of temperature on arsenic removal, the same procedures were followed at 15 and 45°C. Further batch experiments were conducted at different concentrations of arsenic solution (As(III): initial concentration = 5 – 100 mg/L, solution pH = 7.0; As(V): initial concentration = 5 – 100 mg/L, solution pH = 3.0). The samples were collected 6 h post-reaction. The effects of solution pH on selenium removal were investigated in 10 mg/L arsenite or arsenate solution during 6 h. The pH of solution was adjusted using 0.1 M NaOH or 0.1 M HCl. The solution pH was measured with a pH probe (9107BN, Thermo Scientific, USA). All experiments were performed in triplicate.

6.1.2. Adsorptive filtration experiments

Filter type of carbon nanotube/iron oxide magnetic nanocomposites was prepared by sonication and filtration procedure (Brady-Estevez *et al.*, 2011). The nanocomposites were added in dimethyl sulfoxide (DMSO) at a concentration of 1 mg/mL. The suspension was then sonicated for 4 h and subsequently allowed to cool. 20 mL of suspension was vacuum filtered over PTFE (0.5 μ m) membrane filter. An ethanol solution followed by deionized water was then filtered through the filters to remove residual DMSO. The digital image of deposition of carbon nanotube/iron oxide magnetic nanocomposites on PTFE filter was shown in Figure 6.1.

Adsorptive filtration experiments were performed by full filtration test using stirred ultrafiltration cell (Model 8050, Millipore). The schematic diagram of full filtration experiment was shown in Figure 6.2. Prior to experiment, 500 mL of deionized water filtered through the cell at a pressure of 40 psi for nanocomposites attached well to the PTFE surface. Then, 50 mL of desired concentration of As(V) solution (1, 5, 10 mg/L) was introduced to cell at various pressures (25, 30, 35 psi).

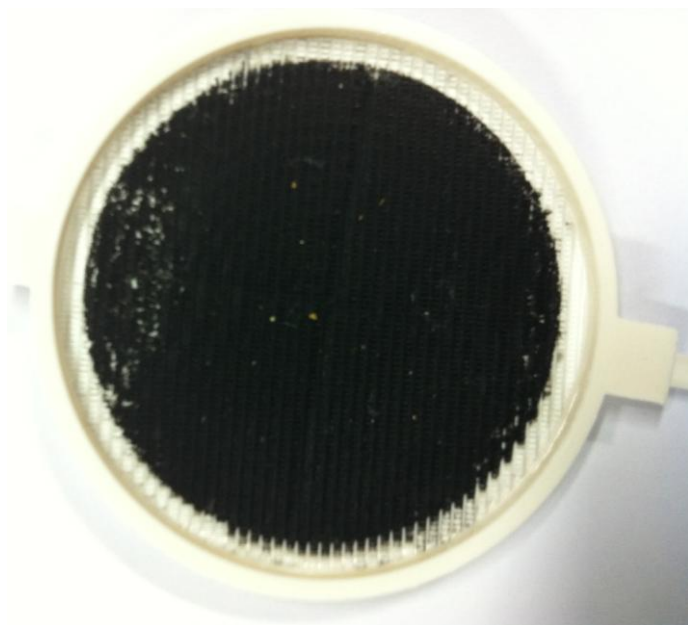


Figure 6.1 Digital image of filter type of carbon nanotube/iron oxide magnetic nanocomposites.

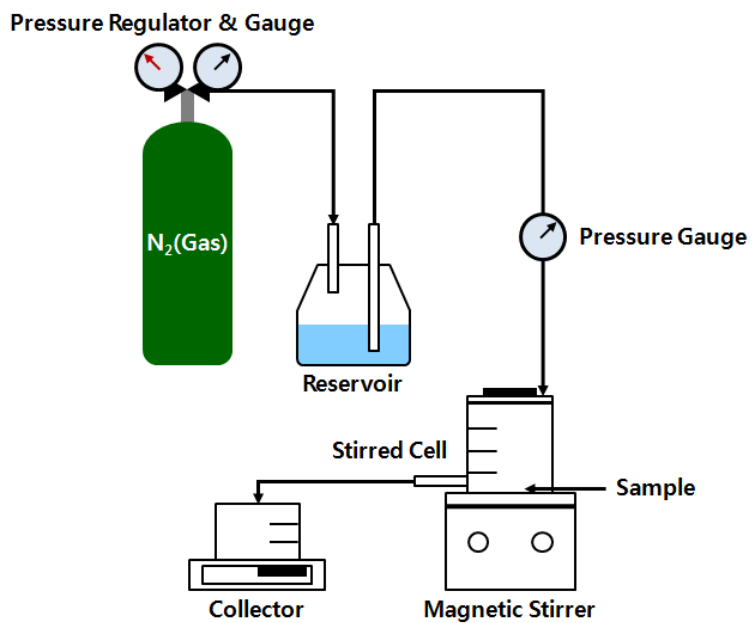


Figure 6.2 Schematic diagram of full filtration experiment.

6.2. Results and Discussion

6.2.1. Characteristics of arsenic sorption

The effect of reaction time (initial concentration = 10 mg/L) on the removal of arsenite and arsenate solution by carbon nanotube/iron oxide magnetic nanocomposites or oxidized carbon nanotube were presented in Figure 6.3 (a) As(III) and (b) As(V), respectively. In case of magnetic nanocomposites, the sorption capacity increased gradually with increasing reaction time until the equilibrium was reached. At 30°C, the sorption capacity of As(III) augmented to 4.84 mg/g at 30 min of reaction time and further increased to 7.10 mg/g at 240 min. While the As(V) sorption capacity was 5.96 mg/g at 30 min and increased to 9.55 mg/g at 240 min. The sorption capacity of oxidized carbon nanotube was negligible (under 0.22 mg/g at all time).

The arsenic removal by the carbon nanotube/iron oxide magnetic nanocomposites as a function of initial concentrations (reaction time = 6 h, solution pH = 7.0 for As(III) and 3.0 for As(V)) were provided in Figure 6.3 (c). Arsenic removal was more sensitive at lower concentration than higher concentration. At the lowest concentration of 4.98 mg/L, the sorption capacity of As(III) was 4.32 mg/g. The sorption capacity increased to 11.71 mg/g at the As(III) concentration of 38.39 mg/L and further increased to 16.52 mg/g at the highest concentration of 98.21 mg/L. Meanwhile, the sorption capacity of As(V) increased from 5.19 to 19.54 mg/g with increasing As(V) concentrations from 5.19 to 104.20 mg/L. At lower concentrations, the arsenic ions available in the solution are fewer in number than the sorption sites on

the magnetic nanocomposites, but there are fewer sorption sites at higher arsenic concentrations.

The effect of solution pH (arsenic concentration = 10 mg/L, reaction time = 6 h) on the removal capacity of As(III) and As(V) by carbon nanotube/iron oxide magnetic nanocomposites were presented in Figure 6.3 (d). Arsenic removal by magnetic nanocomposites was clearly affected by the solution pH. In the adsorption of As(V) to magnetic nanocomposites, the removal capacity remained relatively constant, above 9.0 mg/g for 1.70-2.78 and then dropped gradually to 3.69 mg/g at pH 7.88. In the adsorption of As(III) to magnetic nanocomposites, the removal capacity increased gradually from 4.25 mg/g to 6.95 mg/g between pH 1.55 and 6.84. The removal capacity of As(V) was higher than As(III) at acidic conditions, whereas the removal capacity of As(III) was higher at basic conditions. Similar results were revealed in the literature. Brechbuhl *et al.* (2012) showed that the sorption of As(III) was increased with pH increased, while the sorption of As(V) was decreased with pH increased in hematite. Same results were observed in synthetic pyrite (FeS_2) (Han *et al.*, (2013)).

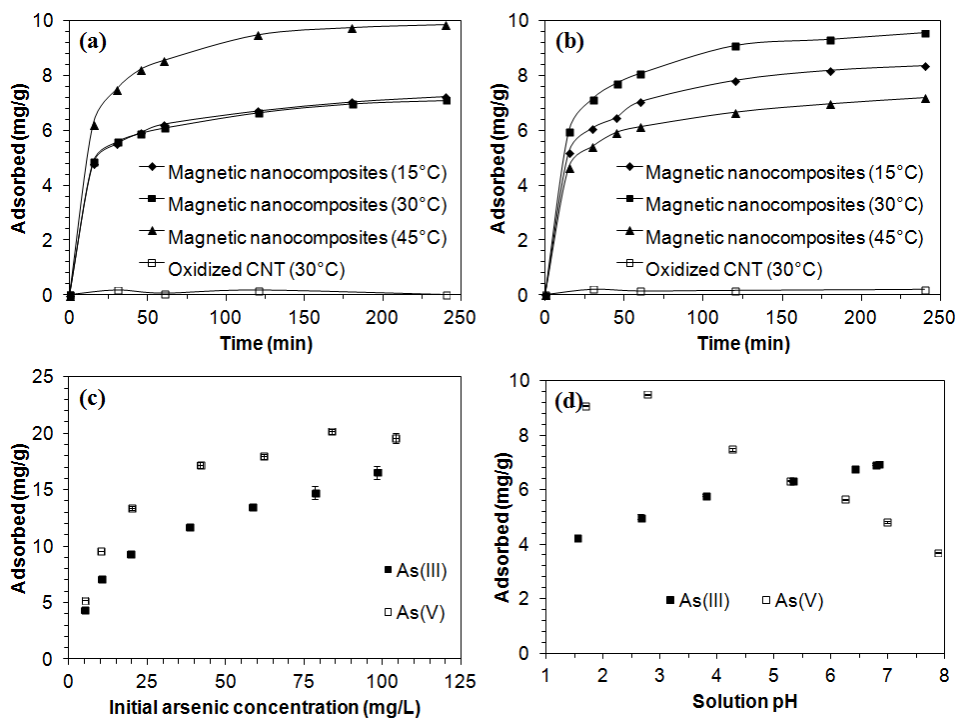


Figure 6.3 Arsenic adsorption to magnetic nanocomposites: (a) effect of reaction time for As(III); (b) effect of reaction time for As(V); (c) effect of initial selenium concentration; (d) effect of solution pH.

6.2.2. Adsorption kinetic, isotherm and thermodynamic analysis

The kinetic model analysis were presented in Figure 6.4. The kinetic model parameters for the pseudo first-order, pseudo second-order, and Elovich models were provided in Table 6.1. The coefficient of determination (R^2) and the value of Chi-square (χ^2) indicates that both the pseudo second-order model and the Elovich model were more suitable at describing the kinetic data than the pseudo first-order model. This indicates that chemisorption is involved in the adsorption of arsenic to carbon nanotube/iron oxide magnetic nanocomposites.

The intra-particle diffusion model applied to the data is shown in Figure 6.5, indicating that the plots were composed of two line segments. The first line in the plot indicates boundary layer adsorption, while the second line describes the intra-particle diffusion (Bajpai and Armo, 2009). The Intra-particle diffusion model parameters are provided in Table 6.2.

The equilibrium isotherms of arsenic in the carbon nanotube/iron oxide magnetic nanocomposites were illustrated in Figure 6.6. Equilibrium isotherm constants were summarized in Table 6.3. The correlation coefficients (R^2) and the value of Chi-square (χ^2) indicated that both the Freundlich isotherms and the Redlich–Peterson isotherms were more suitable at describing the equilibrium data than Langmuir isotherms. The adsorption capacity of Freundlich model (q_m) were 9.218 mg/g for As(III) and 14.595 mg/g for As(V), while the value of K_R/a_R were 5.259 mg/g for As(III) and 10.325 mg/g for As(V).

The thermodynamic analysis for arsenic sorption to magnetic

nanocomposites was presented in Figure 6.7. The thermodynamic parameters were provided in Table 6.4. The thermodynamic behavior of As(III) and As (V) was different. The positive value of ΔH^0 (56.930 kJ/mol) and ΔS^0 (204.511 J/K mol) for As(III) indicates the endothermic and randomness increased at the interface between solid and solution during the sorption process. The negative value of ΔH^0 (-78.501 kJ/mol) and ΔS^0 (-238.210 J/K mol) for As(V) indicates the exothermic and randomness decreased at the interface between solid and solution during the sorption process. The negative values of ΔG^0 (-2.000 ~ -9.861 kJ/mol) indicate that the arsenic sorption process was spontaneous.

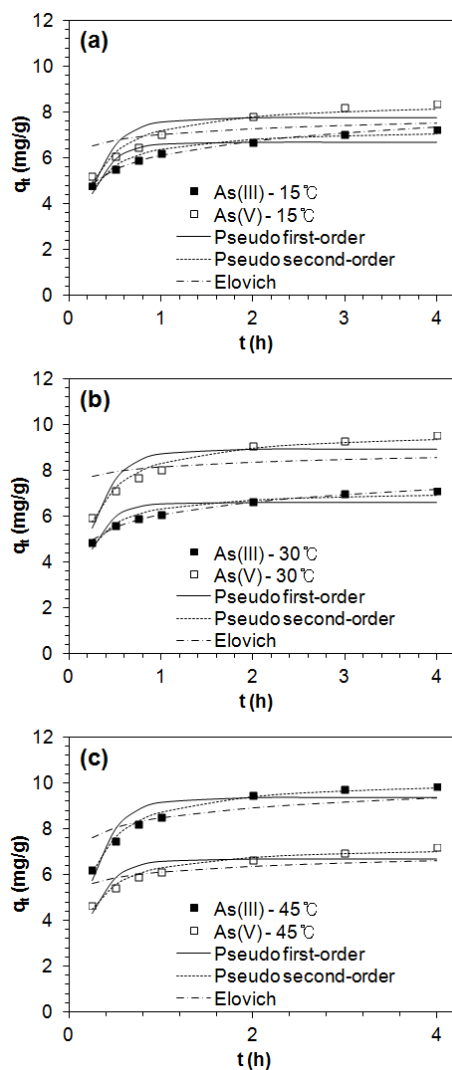


Figure 6.4 Kinetic model fits for arsenate and arsenite removal in the magnetic nanocomposites at various temperatures: (a) 15°C; (b) 30°C; (c) 45°C.

Table 6.1 Kinetic model parameters obtained from model fitting to experimental data

Pseudo first-order model	Temp. (°C)	q _e (mg/g)	k ₁ (/h)	R ²	χ ²	
As(III)	15	6.702	4.347	0.758	0.185	
	30	6.592	4.676	0.729	0.175	
	45	9.350	3.817	0.856	0.191	
As(V)	15	7.764	3.692	0.772	0.288	
	30	8.927	3.781	0.816	0.243	
	45	6.659	4.159	0.790	0.173	
Pseudo second-order model	Temp. (°C)	q _e (mg/g)	k ₂ (g/mg/h)	h (mg/g/h)	R ²	χ ²
As(III)	15	7.275	0.953	50.438	0.964	0.027
	30	7.127	1.075	54.604	0.956	0.028
	45	10.212	0.576	60.068	0.991	0.012
As(V)	15	8.519	0.646	46.882	0.958	0.054
	30	9.770	0.587	56.031	0.978	0.028
	45	7.245	0.903	47.398	0.973	0.022
Elovich kinetic model	Temp. (°C)	α (mg/g)	β (g/mg)	R ²	χ ²	
As(III)	15	9.04E+02	1.135	0.992	0.006	
	30	1.42E+03	1.230	0.993	0.005	
	45	3.74E+05	1.567	0.967	0.383	
As(V)	15	9.42E+07	2.756	0.991	0.581	
	30	3.99E+11	3.433	0.983	0.774	
	45	1.09E+07	2.819	0.988	0.302	

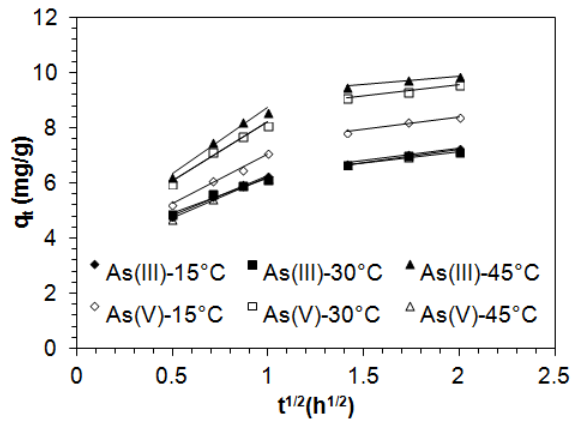


Figure 6.5 Intra-particle diffusion model for arsenate and arsenite removal in the magnetic nanocomposites.

Table 6.2 Intra-particle diffusion model parameters obtained from model fitting to experimental data

Temperature	$k_{i,1}$	I	R^2	$k_{i,2}$	I	R^2
	(mg/g/h ^{0.5})			(mg/g/h ^{0.5})		
15°C	2.874	3.405	0.991	0.906	5.447	0.992
As(III) 30°C	2.487	3.689	0.961	0.781	5.566	0.956
45°C	4.732	3.992	0.971	0.646	8.597	0.965
15°C	3.574	3.457	0.990	0.924	6.546	0.975
As(V) 30°C	4.213	3.982	0.972	0.802	7.940	0.995
45°C	3.019	3.211	0.978	0.910	5.379	0.998

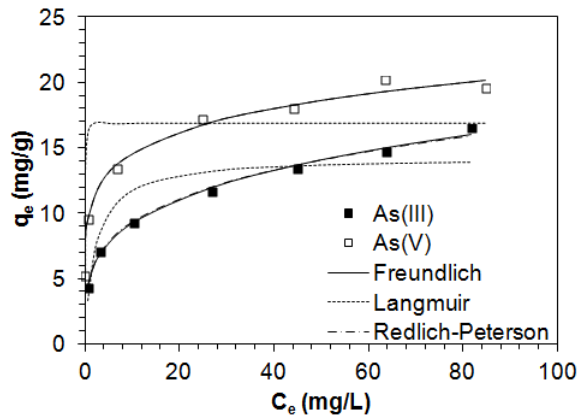


Figure 6.6 Equilibrium isotherm model fits for arsenate and arsenite removal in the magnetic nanocomposites.

Table 6.3 Equilibrium isotherm model parameters obtained from model fitting to experimental data

Freundlich	K_F	$1/n$	q_m	R^2	χ^2	
	(L/g)		(mg/g)			
As(III)	5.019	0.264	9.218	0.995	0.055	
As(V)	10.285	0.152	14.595	0.992	0.083	
Langmuir	Q_m	K_L	R^2	χ^2		
	(mg/g)	(L/mg)				
As(III)	14.263	0.462	0.836	1.736		
As(V)	16.847	41.212	0.602	4.620		
Redlich-Peterson	K_R	a_R	K_R/a_R	g	R^2	χ^2
	(L/g)	(L/mg)	(mg/g)			
As(III)	92.774	17.640	5.259	0.748	0.994	0.050
As(V)	35433.87	3431.78	10.325	0.849	0.992	0.086

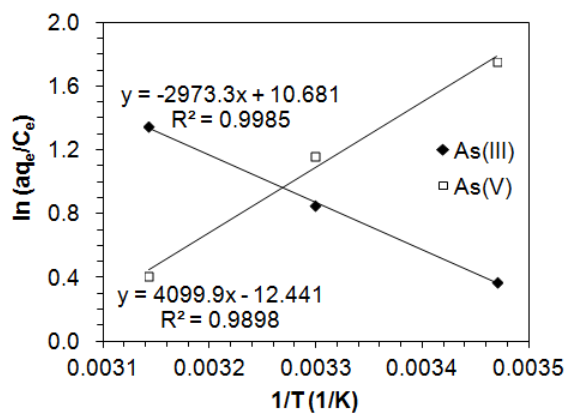


Figure 6.7 Thermodynamic analyses for arsenate and arsenite removal in the magnetic nanocomposites.

Table 6.4 Thermodynamic parameters for selenium adsorption to carbon nanotube/iron oxide magnetic nanocomposites

	Temperature (°C)	ΔH° (kJ/mol)	ΔS° (J/K mol)	ΔG° (kJ/mol)
As(III)	15	56.930	204.511	-2.000
	30			-5.067
	45			-8.135
As(V)	15	-78.501	-238.210	-9.861
	30			-6.288
	45			-2.715

6.2.3. Filtration study

The surface morphology of filter type magnetic nanocomposites was characterized by scanning electron micrographs (SEM) in Figure 6.8. and transmission electron micrographs (TEM). Figure 3.2 showed the SEM images of (a) oxidized carbon nanotube and (b) carbon nanotube/iron oxide magnetic nanocomposites. In contrast to the aligned type of oxidized carbon nanotube, the magnetic nanocomposites depicts the entangled with iron oxide nanoparticles. More detail microstructure of the multi-wall of carbon nanotube was revealed by the TEM image in Figure 3.3. Aerial view (Figure 3.3 (a)) confirmed the nanocomposites entire covered the filter surface. From cross section view (Figure 3.3 (b)), the thickness of the nanocomposites filter was about 62.45 μm . Color mapping was performed using energy dispersive X-ray spectrum (EDS) to visualize the spatial distribution of carbon, oxygen, and iron (Figure 6.9). The mapping image was shown all components well dispersed on filter surface.

The effect of pressure on the capacity of As(V) by carbon nanotube/iron oxide magnetic nanocomposites filter were presented in Figure 6.10 (a). The sorption capacity remained relatively constant, above 9.8 mg/g at 25 and 30 psi. But, the sorption capacity dropped to 7.24 mg/g at 35 psi. The effect of initial concentration of As(V) were shown in Figure 6.10 (b). The sorption capacity was increased with initial concentration.

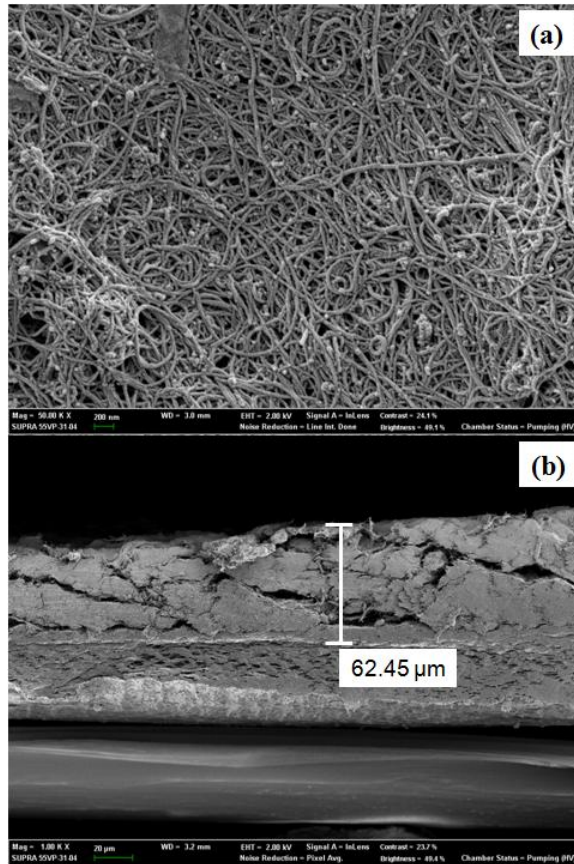


Figure 6.8 SEM image of filter type magnetic nanocomposites: (a) aerial view; (b) cross section view.

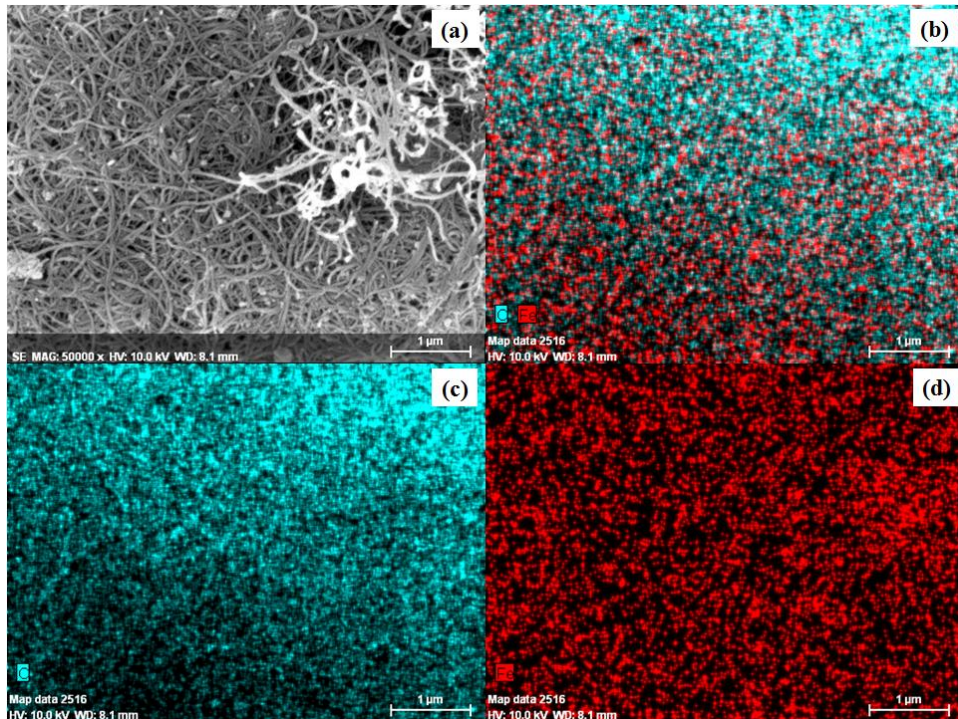


Figure 6.9 Color mapping of filter type magnetic nanocomposites: (a) SEM image of mapping point; (b) carbon (C) and iron (Fe) map; (c) carbon map; (d) iron map.

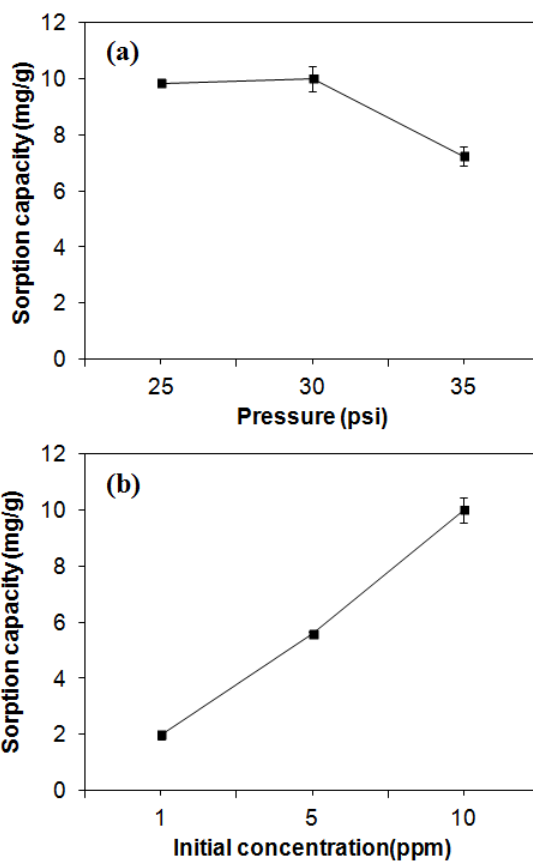


Figure 6.10 As(V) removal by filter type of carbon nanotube/iron oxide magnetic nanocomposites: (a) different pressure (As(V) concentration = 10ppm); (b) different initial As(V) concentration (pressure = 30 psi).

Chapter 7 Magnetic Alginate-Layered Double Hydroxide Composites for Phosphate Removal

Lee, CG; Kim, SB. 2013. Magnetic alginate-layered double hydroxide composites for phosphate removal. *Environmental Technology*, 34: 2749-2756.

The objective of this study was to investigate the phosphate removal using magnetic alginate-layered double hydroxide (LDHs) composites. The magnetic composites were prepared by entrapping synthetic magnetic iron oxide and calcined Mg-Al LDHs in polymer matrix (alginate). Results showed that the magnetic composites (2% magnetic iron oxide and 6% calcined Mg-Al LDHs) were effective in the removal of phosphate with the sorption capacity of 4.99 ± 0.06 mgP/g under given experimental conditions (adsorbent dose = 0.05 g in 30 ml solution; initial phosphate concentration = 10 mgP/l; reaction time = 24 h). Both magnetic iron oxide and calcined Mg-Al LDHs have the ability to adsorb phosphate with the latter having much higher sorption capacity. In the magnetic composites, calcined Mg-Al LDHs functions as a phosphate adsorbent while magnetic iron oxide provides both magnetic and sorption properties. Results also demonstrated that phosphate sorption to the magnetic composites reached equilibrium at 24 h. The maximum phosphate sorption capacity was determined to be 38.583 mgP/g. In addition, phosphate removal was not much sensitive to initial solution pH between 4.1 and 10.2. Only 9% of the phosphate sorption capacity was reduced as the solution pH increased from 4.1 to 10.2. This study demonstrated that magnetic alginate-LDHs composites could be used for phosphate removal in combination with magnetic separation.

7.1. Materials and Methods

7.1.1 Phosphate removal experiments

Phosphate removal by the magnetic composites was conducted under batch conditions. The desired phosphate solution was prepared by diluting the stock solution (1000 mgP/l), which was made from potassium dichromate (KH_2PO_4). All batch experiments were performed in triplicate using 50 ml polypropylene conical tubes. Batch experiments were conducted to examine phosphate removal in the magnetic composites composed of different contents of magnetic iron oxide and calcined Mg-Al LDHs (8%-0%, 6%-2%, 4%-4%, 2%-6%, 0%-8%). The experiments were conducted at an initial phosphate concentration of 10 mgP/l with a composite dose of 0.05 g in 30 ml solution. As a background electrolyte, 20 mM potassium nitrate (KNO_3) was used in the experiments. The tubes were shaken at 25°C and 100 rpm using a shaking incubator (Daihan Science, Korea). Then, the magnetic composites were separated from the solution using a magnet (≈ 1.18 Tesla) 24 h-post reaction. The samples were collected and filtered through a 0.45- μm membrane filter. The phosphate was analyzed by the ascorbic acid method (APHA, 1995). Phosphate concentrations were measured at a wavelength of 880 nm using a UV-vis spectrophotometer (Helios, Thermo Scientific, Waltham, MA, USA).

Batch experiments were also performed at different reaction times (adsorbent dose = 0.05 g; initial phosphate concentration = 10 mgP/l). In the experiments, samples were collected at 2, 4, 8, 12, 18, 24 and 36 h post-reaction. Further batch experiments were conducted at different

concentrations of phosphate solution. The magnetic composites (0.05 g) were added to 30 mL of phosphate solution (initial concentration = 5–200 mgP/l). The samples were collected 24 h post-reaction. Batch experiments were conducted for repeated use of the magnetic composites for phosphate removal (adsorbent dose = 0.05 g; initial phosphate concentration = 10 mgP/l). Through magnetic separation, the magnetic composites were used repeatedly for phosphate removal. For each round of the test, the magnetic composites were removed from the solution at 24-h post reaction using a magnet, moved to deionized water for a 4-h stay, and then applied to new phosphate solution (concentration = 10 mgP/l). In the pH experiments, 0.1 M NaOH and 0.1 M HCl solutions were used to adjust the pH from 4.1 to 10.2. The pH was measured with a pH probe (9107BN, Thermo Scientific, USA).

7.2. Results and Discussion

7.2.1. Characteristics of phosphate sorption

Phosphate removal at various contents of magnetic iron oxide and calcined Mg-Al LDHs in the magnetic composites is presented in Figure 7.1. For experiments with no LDHs (8% magnetic iron oxide – 0% calcined LDHs), the sorption capacity of the magnetic composites was 3.71 ± 0.04 mgP/g. As the calcined LDHs content increased from 2% (6% magnetic iron oxide – 2% calcined LDHs) to 6% (2% magnetic iron oxide – 6% calcined LDHs), the sorption capacity was increased from 4.51 ± 0.06 to 4.99 ± 0.06 mgP/g. For experiments with calcined LDHs only (0% magnetic iron oxide – 8% calcined LDHs), the sorption capacity was 5.10 ± 0.02 mgP/g. Results indicate that both magnetic iron oxide and calcined Mg-Al LDHs have the ability to adsorb phosphate with the latter having much higher capacity. For further experiments, the magnetic composites with 2% magnetic iron oxide and 6% calcined LDHs was used. In the magnetic composites, calcined LDHs functions as a phosphate adsorbent while magnetic iron oxide provides both magnetic and sorption properties. During the experiments, phosphate ions in aqueous solution could diffuse into the magnetic composites through the pores of the composites. Then, phosphate ions could come in contact with the magnetic iron oxide and calcined LDHs particles and subsequently be removed from the aqueous phase to the solid phase.

The phosphate removal by the magnetic composite as a function of reaction time is provided in Figure 7.2. The phosphate concentrations

decreased gradually with increasing reaction time until the equilibrium was reached. At 2 h of reaction time, the phosphate concentration dropped to 6.84 mgP/L (initial concentration =10 mgP/L), and further decreased to 3.1 mgP/L at 12 h. The phosphate sorption reached equilibrium at 24 h of reaction time with phosphate concentration of 1.7 mgP/L. Meanwhile, the percent removal increased from 31.5% to 83.1% with increasing reaction time from 2 h to 24 h.

The phosphate removal by the magnetic composites as a function of initial phosphate concentration is provided in Figure 7.3. Phosphate removal was highly concentration dependent. At the lowest concentration of 5 mgP/L, the percent removal was 90%. The percent removal decreased to 40% at the phosphate concentration of 50 mgP/L and further decreased to 31% at the highest concentration of 200 mgP/L. Meanwhile, the sorption capacity increased from 2.71 to 34.51 mgP/g with increasing phosphate concentrations from 5 to 200 mgP/L. At lower concentrations, the phosphate ions available in the solution are fewer in number than the sorption sites on the magnetic composites, but there are fewer sorption sites at higher phosphate concentrations.

Phosphate removal upon repeated use of the magnetic composites is presented in Figure 7.4. In the first use, the sorption capacity was determined to be 4.70 mgP/g. In the second round, the sorption capacity was reduced to 2.54 mgP/g. The sorption capacity was reduced to 1.55 and 0.55 mgP/g in the third and fourth rounds, respectively.

The effect of initial solution pH on phosphate removal by the magnetic composites is presented in Table 7.1. The percent removal at pH 4.1 was $84.97 \pm 0.32\%$ and decreased slightly to $82.48 \pm 1.01\%$ at

pH 7.0. As the pH approached to 10.2, the percent removal reached at $77.24 \pm 0.58\%$. As the solution pH increased from 4.1 to 10.2, the percent removal decreased only 7.7%. The sorption capacity at pH 4.1 was 5.10 ± 0.02 mgP/g and decreased to 4.95 ± 0.06 mgP/g at pH 7.0. The sorption capacity further decreased to 4.63 ± 0.04 mgP/g at pH 10.2. Only 9% of the phosphate sorption capacity was reduced as the solution pH changed from 4.1 to 10.2. These results demonstrated that phosphate removal in the magnetic composites was not drastically changed between pH 4.1 and pH 10.2. This result could be related to the fact that the final (equilibrium) pH converged to 7.9–8.0 during the sorption experiments (see Table 7.1). Our results were similar with the report of Han *et al.* (2011) showing that the removal of phosphate in the alginate beads containing calcined Mg-Al LDHs was not sensitive to solution pH. They demonstrated that the percent removal of phosphate decreased slightly from 98.6% to 95.5% as solution pH increased from 4.9 to 8.9. However, Das *et al.* (2006) reported that phosphate removal in Mg-Al LDHs decreased sharply from 91.7% to 39.0% with increasing pH from 5.0 to 10.0. Ookubo *et al.* (1993) showed that phosphate removal in Mg-Al LDHs had an increasing tendency between 5.5 and 7.0 but a decreasing one between 7.0 and 9.5.

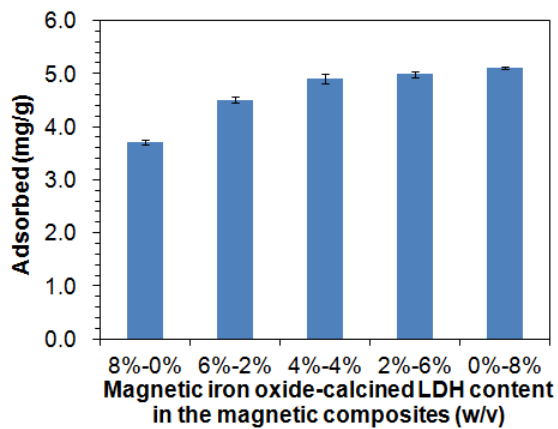


Figure 7.1 Phosphate removal at various contents of magnetic iron oxide-calcined Mg-Al LDHs in the magnetic composites (adsorbent dose = 0.05 g in 30 mL solution; initial phosphate concentration = 10 mgP/L)

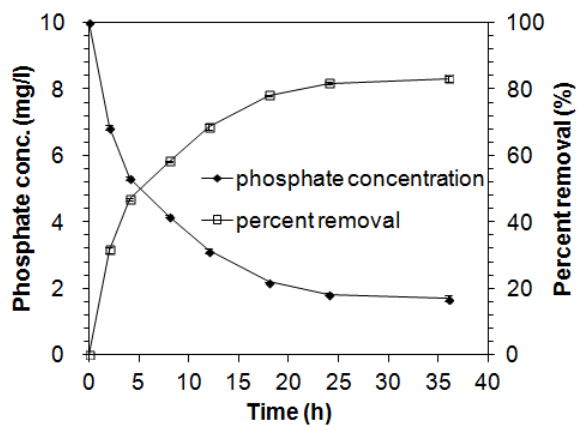


Figure 7.2 Phosphate removal by the magnetic composites as a function of reaction time (adsorbent dose = 0.05 g in 30 mL solution; initial phosphate concentration = 10 mg/l).

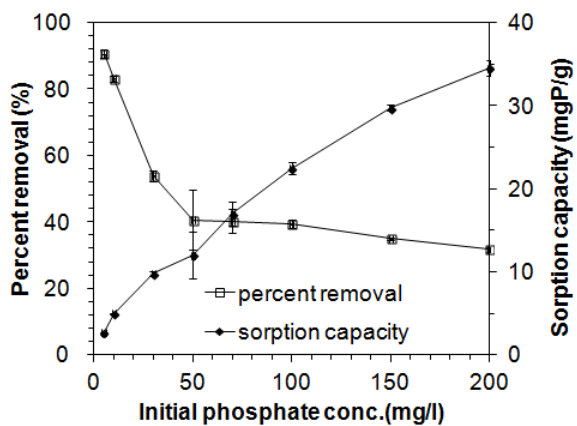


Figure 7.3 Phosphate removal by the magnetic composites as a function of initial phosphate concentration (adsorbent dose = 0.05 g in 30 mL solution; reaction time = 24 h).

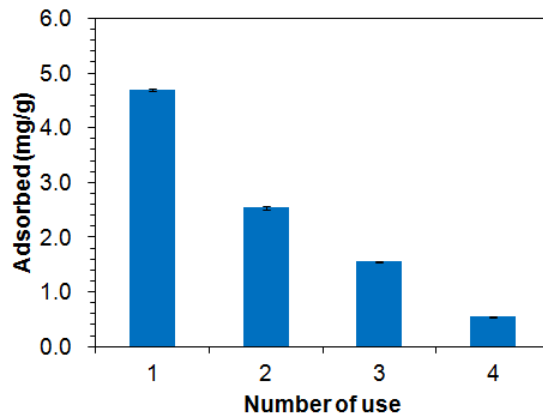


Figure 7.4 Phosphate removal upon repeated use of the magnetic composites (adsorbent dose = 0.05 g in 30 mL solution; initial phosphate concentration = 10 mgP/l).

Table 7.1 Phosphate removal by the magnetic composites at different initial solution pH (adsorbent dose = 0.05 g in 30 ml solution; initial phosphate concentration = 10 mg P/l)

Initial pH	4.1	4.9	5.9	7.0	7.7	9.0	10.2
Percent removal (%)	84.97 ± 0.32	82.92 ± 3.09	82.01 ± 1.88	82.48 ± 1.01	80.79 ± 0.38	80.04 ± 0.75	77.24 ± 0.58
Sorption capacity (mgP/g)	5.10 ± 0.02	4.98 ± 0.19	4.92 ± 0.11	4.95 ± 0.06	4.85 ± 0.02	4.80 ± 0.05	4.63 ± 0.04
Final pH	7.9	7.9	7.9	8.0	8.0	8.0	8.0

7.2.2. Adsorption kinetics and equilibrium isotherms

The kinetics of phosphate sorption in the magnetic composites is provided in Figure 7.5. The model parameters for the pseudo first-order, pseudo second-order, and Elovich models are presented in Table 7.2. In the pseudo first-order model, the value of q_e was 4.759 mgP/g while the value of k_1 was 0.218 1/h. In the pseudo second-order model, the value of q_e was 5.607 mgP/g while the value of k_2 was 0.044 g/mgP/h. The value of q_e from the pseudo second-order model was greater than that from the pseudo first-order model. The initial adsorption rate of second order process (h) was 1.372 mgP/g/h while the value of α (initial adsorption rate of Elovich model) was 3.115 mgP/g/h. The correlation coefficients (R^2) and the value of Chi-square (χ^2) indicated that the pseudo second-order model ($R^2 = 0.990$ and $\chi^2 = 0.021$) was most suitable at describing the kinetic data. This finding indicates that chemisorption is involved in the adsorption of phosphate to magnetic alginate-layered double hydroxide composites.

The intra-particle diffusion model applied to the data is shown in Figure 7.6, indicating that the plots were composed of two line segments. The first line in the plot indicates boundary layer adsorption, while the second line describes the intra-particle diffusion (Bajpai and Armo, 2009). The Intra-particle diffusion model parameters are provided in Table 7.3. The diffusion rate constant of the first line ($k_{i,1}$) was 1.048 mgP/g/h^{0.5} with the intercept value (I) of 0.537. The value of $k_{i,2}$ was 0.328 mgP/g/h^{0.5} with $I = 3.150$. The diffusion model was well fitted to the data, with coefficients of determination (R^2) of 0.982 (first

line) and 0.807 (second line).

The equilibrium isotherm of phosphate in the magnetic composites is illustrated in Figure 7.7. Equilibrium isotherm constants are summarized in Table 7.4. The correlation coefficients (R^2) and the value of Chi-square (χ^2) indicated that both the Freundlich and Redlich–Peterson isotherms were suitable for describing the equilibrium data. In Figure 7.7, the Redlich–Peterson model fit was superimposed on the Freundlich fit. The Redlich–Peterson model can be reduced to the Freundlich model when the first term in the denominator(=1) was negligible except for small value of $a_R C_e^g$. In the Freundlich model parameters (Table 7.4), the value of K_F was 3.118 L/g, which corresponded well to the value of K_R/a_R in the Redlich–Peterson model. The value of $1/n$ is equivalent to the value of $(1-g)$. The adsorption capacity of Freundlich model (q_m) was 38.583 mgP/g while the maximum adsorption capacity of Langmuir model was 29.017 mgP/g. The maximum adsorption capacity determined from our experiments was in the range of the phosphate removal capacity of zirconium mesostructures immobilized in alginate beads (26.95–51.74 mgP/g) reported by Yeon *et al.* (2008).

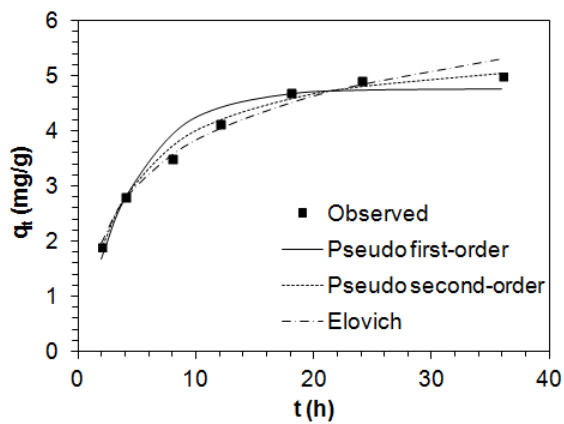


Figure 7.5 Kinetic model fits for phosphate removal in the magnetic composites.

Table 7.2 Kinetic model parameters obtained from model fitting to phosphate experimental data

Pseudo first-order model				
q_e (mg/g)	k_1 (1/h)	R^2	χ^2	
4.759	0.218	0.953	0.111	
Pseudo second-order model				
q_e (mg/g)	k_2 (g/mg/h)	h (mg/g/h)	R^2	χ^2
5.607	0.044	1.372	0.990	0.021
Elovich kinetic model				
α (mg/g/h)	β (g/mg)	R^2	χ^2	
3.115	0.863	0.981	0.034	

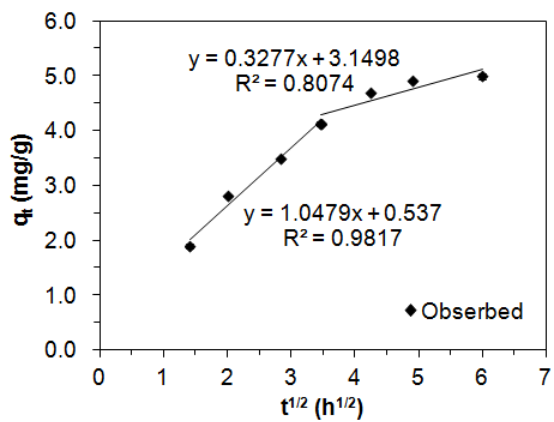


Figure 7.6 Intra-particle diffusion model for phosphate removal in the magnetic composites.

Table 7.3 Intra-particle diffusion model parameters obtained from model fitting to phosphate experimental data

$k_{i,1}$ (mg/g/h ^{0.5})	I	R ²	$k_{i,2}$ (mg/g/h ^{0.5})	I	R ²
1.048	0.537	0.982	0.328	3.150	0.807

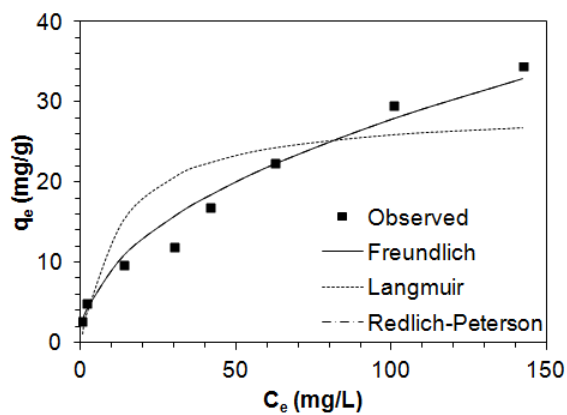


Figure 7.7 Equilibrium isotherm model fits for phosphate removal in the magnetic composites.

Table 7.4 Equilibrium isotherm model parameters obtained from model fitting to phosphate experimental data

Freundlich model					
K_F (L/g)	1/n	q_m (mg/g)	R^2	χ^2	
3.118	0.475	38.583	0.976	1.625	
Langmuir model					
Q_m (mg/g)	K_L (L/mg)	R^2	χ^2		
29.017	0.081	0.771	12.846		
Redlich-Peterson model					
K_R (L/g)	a_R (L/mg)	K_R/a_R (mg/g)	g	R^2	χ^2
9868.13	3163.94	3.119	0.525	0.976	1.625

Chapter 8 Removal of Chromate from Aqueous Solution Using Magnetic Alginate-Layered Double Hydroxide Composites

Lee, CG; Park, JA; Lee, I; Kang, JK; Yoon, SY; Kim, SB. 2013. Preparation of magnetic alginate-layered double hydroxide composite adsorbents and removal of Cr(VI) from aqueous solution. *Water Science & Technology: Water Supply*, 13: 846-853.

The aim of this study was to investigate the removal of Cr(VI) from aqueous solution using magnetic alginate-layered double hydroxide (LDHs) composites. Magnetic iron oxide and calcined Mg-Al LDHs powders were synthesized in the laboratory. The magnetic composites were prepared through immobilization of synthetic magnetic iron oxide and calcined Mg-Al LDHs powders into alginate matrix. The magnetic composites had a particle size of 1.5 ± 0.1 μm and showed magnetic properties under an external magnetic field. Results demonstrated that the magnetic composites were effective in the removal of Cr(VI). In the magnetic composites, calcined LDHs played a major role in the sorption of Cr(VI), whereas magnetic iron oxide provided the magnetic property along with a minor role in Cr(VI) sorption. Kinetic tests showed that Cr(VI) sorption to the magnetic composites reached equilibrium at 24 h. The maximum Cr(VI) removal capacity was 11.2 mg/g. Results also indicated that Cr(VI) removal was not sensitive to solution pH between 4.1 and 9.5. This study demonstrated the potential applications of magnetic alginate-LDHs composites for chromate removal from aqueous solution in combination with magnetic separation.

8.1. Materials and Methods

8.1.1 Chromate removal experiments

The desired Cr(VI) solution was prepared by diluting the stock Cr(VI) solution (1000 mg/L), which was made from potassium

dichromate ($\text{K}_2\text{Cr}_2\text{O}_7$). All batch experiments were performed in 50 mL polypropylene conical tubes. Batch experiments were conducted to examine Cr(VI) removal by the magnetic composites composed of different contents of calcined LDHs and magnetic iron oxide (8%–0%, 6%–2%, 4%–4%, 2%–6%). The experiments were conducted at an initial Cr(VI) concentration of 10 mg/L with a composite dose of 0.05 g in 30 mL solution. As a background electrolyte, 20 mM potassium nitrate (KNO_3) was used in the experiments. The tubes were shaken at 25 °C and 100 rpm using a shaking incubator (Daihan Science, Korea). Then, the magnetic composites were separated from the solution using a magnet (≈ 1.18 Tesla) 24 h-post reaction. The Cr(VI) concentration was measured using the diphenylcarbazide method.

Next, kinetic batch experiments were performed at the initial Cr(VI) concentration of 10 mg/L and a composite dose of 0.05 g in 30 mL solution. In the experiments, samples were collected at 2, 4, 8, 12, 24, 36 and 48 h post-reaction. Equilibrium batch experiments were conducted with different concentrations of Cr(VI) solution. Magnetic composite (0.05 g) was added to 30 mL of a chromate solution (initial concentration = 5–200 mg/L). The samples were collected 24 h post-reaction. In the pH experiments, 0.1 M NaOH and 0.1 M HCl solutions were used to adjust pH from 4.1 to 9.5. The pH was measured with a pH probe (9107BN, Thermo Scientific, USA). All experiments were performed in triplicate.

8.2. Results and Discussion

8.2.1. Characteristics of chromate sorption

Cr(VI) removal at various contents of calcined LDHs-magnetic iron oxide in the magnetic composites is shown in Figure 8.1. For experiments with no added iron oxide (8% calcined LDHs – 0% magnetic iron oxide, MC-80), the adsorption capacity of the composites (MC-80) was 2.17 mg/g. At an iron oxide content of 2% (6% calcined LDHs – 2% magnetic iron oxide, MC-62), the capacity of MC-62 was reduced to 1.50 mg/g. When the iron oxide content increased from 2 to 4% (4% calcined LDHs – 4% magnetic iron oxide, MC-44), the capacity of MC-44 decreased further to 1.31 mg/g. Another 2% increase in the iron oxide content from 4 to 6% (2% calcined LDHs – 6% magnetic iron oxide, MC-26) resulted in a decrease of the adsorption capacity of MC-26 to 0.98 mg/g. Results demonstrated that the Cr(VI) sorption capacity of the composites decreased with decreasing calcined LDHs (increasing magnetic iron oxide) content in the composites. Note that the sorption capacity of MC-26 was only 66% of the MC-62 capacity in given experimental conditions. This indicated that calcined LDHs played a major role in the sorption of Cr(VI), whereas magnetic iron oxide provided the magnetic property along with a minor role in Cr(VI) sorption. For further experiments, the composites with 6% calcined LDHs and 2% magnetic iron oxide were used.

Cr(VI) removal upon repeated use of the magnetic composites

(adsorbent dose = 0.05 g; initial Cr(VI) concentration = 10 mg/L) is presented in Figure 8.2. Through magnetic separation, the composites were used repeatedly for Cr(VI) removal. For each round of the test, the composites were removed from the solution at 24-h post reaction using a magnet, moved to deionized water for a 4-h stay, and then applied to a new Cr(VI) solution (concentration = 10 mg/L). In the first use, the Cr(VI) adsorption capacity was determined to be 1.61 mg/g. In the second round, the adsorption capacity was reduced to 0.61 mg/g. The adsorption capacity was reduced to 0.42 mg/g in the third round, and was absent in the fourth round.

In our experiments, chromate ions (HCrO_4^- , $\text{Cr}_2\text{O}_7^{2-}$) in aqueous solution could diffuse into the magnetic composites through the pores of the composites. Then, chromate ions could come in contact with the entrapped particles and subsequently be removed from the aqueous phase to the solid phase. In surface adsorption, the negatively-charged chromate could adsorb to the positively-charged brucite-like layer (Prasanna *et al.*, 2006). Chromate ions could replace the charge balancing anion (carbonate) in the interlayer region of LDHs via an anion exchange process (Goswamee *et al.*, 1998). Furthermore, chromate could intercalate into the interlayer during the reconstruction/rehydration of the calcined LDHs in an aqueous medium (Rhee *et al.*, 1997). In addition, a part of chromate ions could adsorb to magnetic iron oxide particles through electrostatic interaction and anion exchange (Hu *et al.*, 2005).

The Cr(VI) removal by the magnetic composite as a function of reaction time is provided in Figure 8.3. The Cr(VI) concentrations

decreased gradually with increasing reaction time until the equilibrium was reached. At 2 h of reaction time, the Cr(VI) concentration dropped to 8.8 mg/L (initial concentration =10 mg/L), and further decreased to 7.6 mg/L at 12 h. The chromate sorption reached equilibrium at 24 h of reaction time with Cr(VI) concentration of 7.5 mg/L. Meanwhile, the percent removal increased from 12.1% to 25.1% with increasing reaction time from 2 h to 24 h.

The Cr(VI) removal by the magnetic composites as a function of initial Cr(VI) concentration is provided in Figure 8.4. Cr(VI) removal was highly concentration dependent. At the lowest concentration of 5 mg/L, the percent removal was 37%. The percent removal decreased to 10% at the Cr(VI) concentration of 50 mg/L and further decreased to 6% at the highest concentration of 200 mg/L. Meanwhile, the sorption capacity increased from 1.11 to 7.33 mg/g with increasing Cr(VI) concentrations from 5 to 200 mg/L. At lower concentrations, the chromate ions available in the solution are fewer in number than the sorption sites on the magnetic composites, but there are fewer sorption sites at higher chromate concentrations.

The effect of initial solution pH on Cr(VI) removal by the composites is presented in Figure 8.5. Adsorption capacity was 1.65 mg/g at pH 4.1 and increased slightly to 1.82 mg/g at pH 5.8. As the solution pH further increased, the adsorption capacity decreased slightly and arrived at 1.56 mg/g at pH 9.5. These results demonstrated that Cr(VI) removal in the composites was not drastically changed in the pH range of 4.1–9.5. This could be related to the fact that the final (equilibrium) pH converged to 8.2–8.3 in the experiments. The effect of

initial solution pH was minimized due to a change of solution pH, and so the adsorption capacities of the composite at pH 4.1–9.5 were not significantly different. Our results were similar with those of a previous report (Rocher *et al.*, 2008) showing that the removal of organic dyes in magnetic alginate beads containing activated carbon was not affected by solution pH between 3 and 10. It was also reported that LDHs-alginate beads were not sensitive to pH 4.9–8.9 in the removal of phosphate (Han *et al.*, 2011).

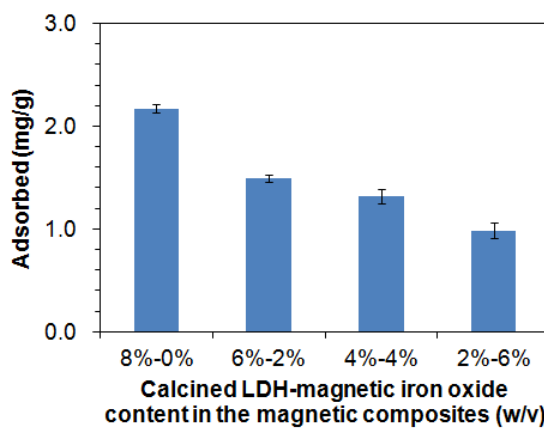


Figure 8.1 Chromate removal at various contents of calcined Mg-Al LDHs-magnetic iron oxide in the magnetic composites (adsorbent dose = 0.05 g in 30 mL solution; initial Cr(VI) concentration = 10 mg/L).

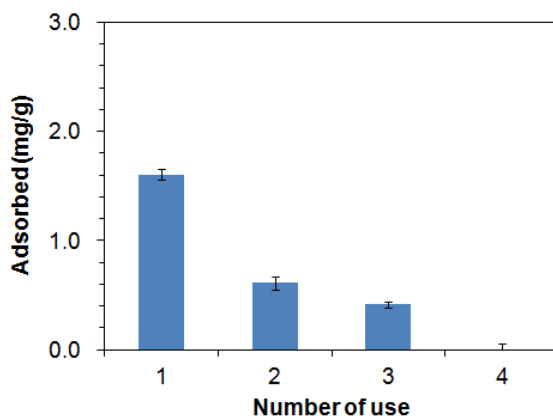


Figure 8.2 Chromate removal upon repeated use of the magnetic composites (adsorbent dose = 0.05 g; initial Cr(VI) concentration = 10 mg/L).

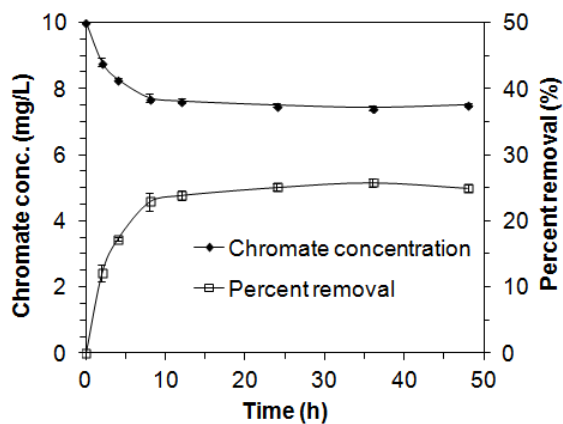


Figure 8.3 Chromate removal by the magnetic composites as a function of reaction time (adsorbent dose = 0.05 g in 30 mL solution; initial Cr(VI) concentration = 10 mg/L).

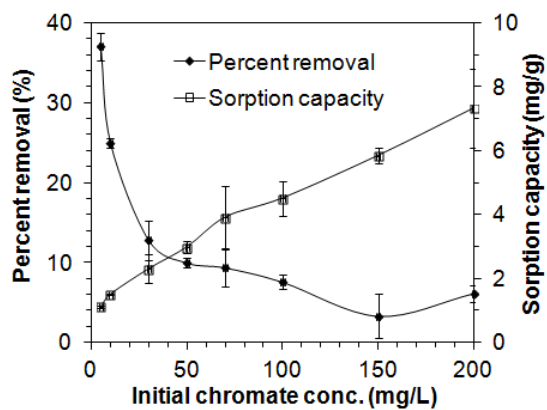


Figure 8.4 Chromate removal by the magnetic composites as a function of initial Cr(VI) concentration (adsorbent dose = 0.05 g in 30 mL solution; reaction time = 24 h).

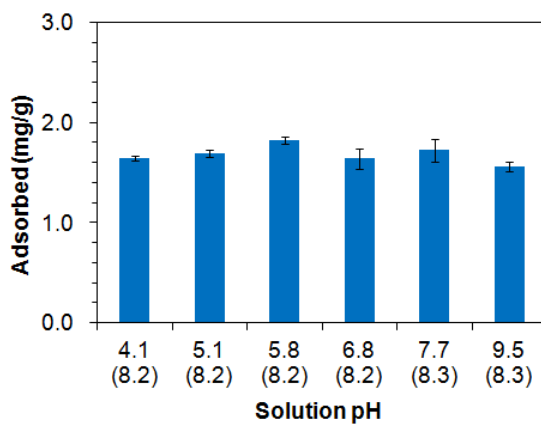


Figure 8.5 Effect of initial solution pH on chromate removal by the magnetic composites (adsorbent dose = 0.05 g; initial Cr(VI) concentration = 10 mg/L). The number in the parenthesis is final (equilibrium) pH.

8.2.2. Adsorption kinetics and equilibrium isotherms

The kinetics of Cr(VI) adsorption by the magnetic composites is provided in Figure 8.6. The model parameters for the pseudo first-order, pseudo second-order, and Elovich models are presented in Table 8.1. In the pseudo first-order model, the value of q_e was 1.503 mg/g while the value of k_1 was 0.311 1/h. In the pseudo second-order model, the value of q_e was 1.656 mg/g while the value of k_2 was 0.258 g/mgP/h. The initial adsorption rate of second order process (h) was 0.709 mgP/g/h while the value of α (initial adsorption rate of Elovich model) was 3.336 mgP/g/h. The correlation coefficients (R^2) and the value of Chi-square (χ^2) indicated that the pseudo first-order model ($R^2 = 0.991$ and $\chi^2 = 0.004$) was most suitable at describing the kinetic data.

An intra-particle diffusion model applied to the kinetic sorption data is shown in Figure 8.7, indicating that the plots were composed of two line segments. The diffusion model was well fitted to the data, with coefficients of determination (R^2) of 0.99 (first line) and 0.51 (second line). Values of k_i for the first and second lines were 0.46 and 0.02 mg/g/h^{1/2}, respectively (Table 8.2). The first line in the plot indicates boundary layer adsorption, while the second line describes the intra-particle diffusion (Bajpai and Armo, 2009).

The equilibrium isotherm of Cr(VI) sorption by the composites is illustrated in Figure 8.8. Equilibrium isotherm constants are summarized in Table 8.3. In the Freundlich model, the distribution coefficient (K_F) was 0.519 L/g while the Freundlich constant ($1/n$) was 0.490. The adsorption capacity of Freundlich model (q_m) was 6.962 mg/g. In the Langmuir model, the Langmuir constant (K_L) was 0.030

L/mg while the maximum removal capacity (Q_m) was 6.939 mg/g. The maximum adsorption capacity determined from our experiments was in the range of the chromate removal capacity for LDHs (9–160 mg/g) reported in the literature (Goh *et al.*, 2008). In Figure 8.8, the Redlich–Peterson model fit was superimposed on the Freundlich fit. The Redlich–Peterson model can be reduced to the Freundlich model when the first term in the denominator(=1) was negligible except for small value of $a_R C_e^g$. In the Redlich–Peterson model parameters (Table 8.3), the value of K_R/a_R was 0.519 mg/g, which corresponded well to the value of K_F in the Freundlich model. The value of g is equivalent to the value of $(1-1/n)$. The correlation coefficients (R^2) and the value of Chi-square (χ^2) indicated that both the Freundlich and Redlich–Peterson isotherms were suitable for describing the equilibrium data.

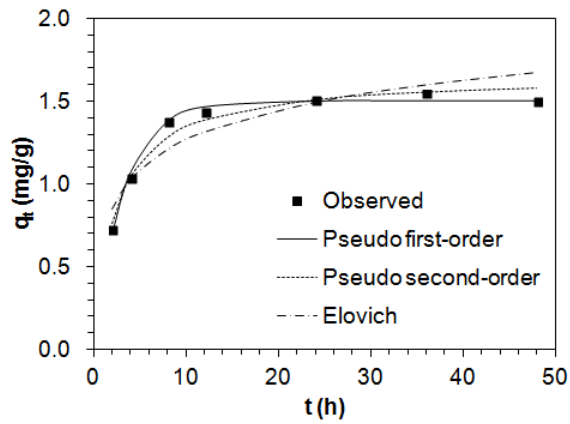


Figure 8.6 Kinetic model fits for chromate removal in the magnetic composites.

Table 8.1 Kinetic model parameters obtained from model fitting to phosphate experimental data

Pseudo first-order model				
q_e (mg/g)	k_1 (1/h)	R^2	χ^2	
1.503	0.311	0.991	0.004	
Pseudo second-order model				
q_e (mg/g)	k_2 (g/mg/h)	h (mg/g/h)	R^2	χ^2
1.656	0.258	0.709	0.966	0.015
Elovich kinetic model				
α (mg/g/h)	β (g/mg)	R^2	χ^2	
3.336	3.839	0.844	0.072	

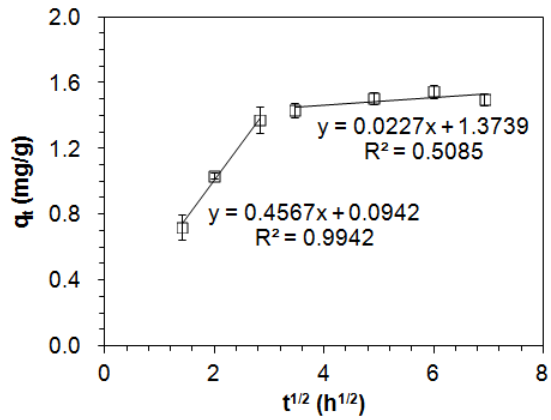


Figure 8.7 Intra-particle diffusion model for chromate removal in the magnetic composites.

Table 8.2 Intra-particle diffusion model parameters obtained from model fitting to phosphate experimental data

$k_{i,1}$ (mg/g/h ^{0.5})	I	R ²	$k_{i,2}$ (mg/g/h ^{0.5})	I	R ²
0.457	0.094	0.994	0.023	1.374	0.509

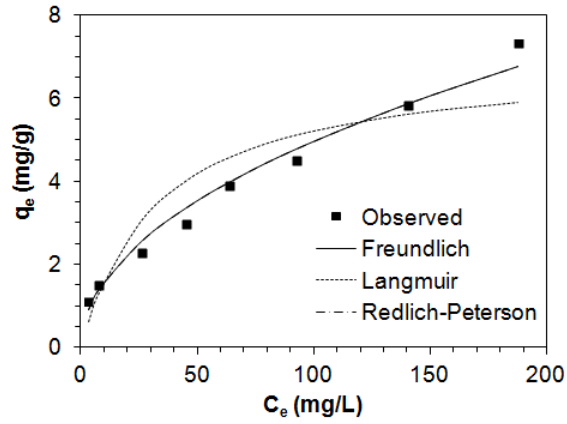


Figure 8.8 Equilibrium isotherm model fits for phosphate removal in the magnetic composites.

Table 8.3 Equilibrium isotherm model parameters obtained from model fitting to phosphate experimental data

Freundlich model					
K_F (L/g)	1/n	q_m (mg/g)	R^2	χ^2	
0.519	0.490	6.962	0.981	0.187	
Langmuir model					
Q_m (mg/g)	K_L (L/mg)	R^2	χ^2		
6.939	0.030	0.853	1.434		
Redlich-Peterson model					
K_R (L/g)	a_R (L/mg)	K_R/a_R (mg/g)	g	R^2	χ^2
3487.49	6725.81	0.519	0.510	0.981	0.187

Chapter 9 General Conclusions and Recommendations

9.1 General conclusions

This thesis was performed with two types of adsorbents in batch reactor systems. One was for selenium, chromium, and arsenic removal from solution using synthesized carbon nanotube / iron oxide magnetic nanocomposites and the other one was for removal of chromium and phosphorous using and magnetic alginate-layered double hydroxide composites. The synthesized adsorbents were characterized by analytical techniques such as SEM, TEM, nitrogen sorption, FTIR, pH_{PZC} , EDS, XRD, XRF, XPS, and VSM. Batch experiments were performed at different reaction time, initial concentration, solution pH, and temperature. Data were analyzed by kinetic adsorption model, kinetic diffusion model, isotherm model, and thermodynamic analysis.

1. In chapter 3, Carbon nanotube/ iron oxide magnetic nanocomposites were prepared using chemical co-precipitation of iron oxide nanoparticle on surface of carbon nanotube after oxidation. These analyses indicated that nano-sized iron oxide particles grown on the surface of oxidized carbon nanotube has diameters ranging from 6 to 17 nm, regularly. Specific surface area of magnetic nanocomposites was $119.09 \text{ m}^2/\text{g}$ with $0.4748 \text{ cm}^3/\text{g}$ of total pore volume and 5.1 of point of zero charge. XRD peaks showed that iron oxide nanoparticles were classified as a cubic iron oxide phase, i.e., maghemite and goethite. The magnetic nanocomposites can be easily separated from the aqueous solution within few seconds by permanent magnet. Magnetic alginate-layered double hydroxide

composites were prepared by entrapping powdered forms of both calcined Mg-Al LDHs and magnetic iron oxide in an alginate hydrogel. The magnetic composites had a particle size of 1.5 ± 0.1 μm and showed magnetic properties under an external magnetic field.

2. In chapter 4, the sorption capacity for selenite and selenate were 8.12 mg/g and 3.82 mg/g under given experimental conditions (initial concentration = 10 mg/L, reaction time = 240 min, temperature = 30°C), respectively. Se(IV) removal capacity remained relatively constant between pH 1.81 and 4.01 and then dropped gradually as pH increased. In case of Se(VI) was dropped gradually between pH 1.88 and 7.01. Pseudo second-order kinetic model and Redlich–Peterson isotherms were most suitable for describing the experimental data. Thermodynamic analysis indicates that the selenite sorption process was unfavorable and less feasible but selenate was spontaneous. XPS analysis revealed that selenite and selenate were reduced on the surface of magnetic nanocomposites, accompanied with iron oxidation.
3. In chapter 5, the sorption of chromate to the nanocomposites depended strongly on solution pH. The sorption capacity dropped gradually from 5.07 mg/g to 2.13 mg/g as pH increased 3.77 and 7.28. Pseudo second-order kinetic model and Redlich–Peterson isotherms were most suitable for describing the kinetic and equilibrium sorption, respectively. ΔG^0 for Cr(VI) sorption

was negative, indicating that the Cr(VI) sorption process was spontaneous. Sequencing extraction experiments showed that 57.8% of Cr(VI) was present in fraction of iron oxides (F3).

4. In chapter 6, the maximum sorption capacity for arsenite and arsenate were 16.52 mg/g and 20.16 mg/g, respectively. pH increases, the adsorption amount of selenite has increased but selenate has decreased. Pseudo second-order kinetic model and Freundlich isotherms were most suitable at describing the data. The sorption of As(III) was endothermic but As(V) was exothermic sorption. Arsenate was removed by magnetic nanocomposites in the adsorptive filtration process, effectively.
5. In chapter 7, the magnetic alginate-LDHs composites were effective in the removal of phosphate. Both magnetic iron oxide and calcined Mg-Al LDHs have the ability to adsorb phosphate with the latter having much higher sorption capacity for phosphate. Results also demonstrated that phosphate sorption to the magnetic composites reached equilibrium at 24 h. The maximum phosphate sorption capacity was determined to be 39.063 mgP/g. In addition, phosphate removal was not much sensitive to initial solution pH between 4.1 and 10.2. This study demonstrated that magnetic alginate-LDHs composites could be used for phosphate removal in combination with magnetic separation.
6. In chapter 8, the magnetic alginate-LDHs composites were

effective in the removal of Cr(VI). In the composites, calcined LDHs played a major role in the sorption of Cr(VI), whereas magnetic iron oxide provided the magnetic property along with a minor role in Cr(VI) sorption. Kinetic tests showed that Cr(VI) sorption to the composites reached equilibrium at 24 h. The maximum Cr(VI) removal capacity was determined to be 11.2 mg/g. Results also indicated that Cr(VI) removal was not sensitive to initial solution pH between 4.1 and 9.5. This study demonstrated potential applications of magnetic alginate-LDHs composites for chromate removal from aqueous solution in combination with magnetic separation.

The results of this dissertation provide the information about the synthetic method and the characteristic of the synthesized magnetic composites. It also helps to enhance the knowledge of application of the magnetic composites for water treatment especially for removal of selenium, chromium, arsenic, and phosphorous from aqueous solutions. The results attained from this study will contribute to the development of compatible water treatment technology for removing anionic contaminants. Water filtration with the carbon nanotube/iron oxide magnetic nanocomposites is cost effective, consumes low energy and causes no side effect. Point-of-use (POU) water treatment adapting this filtration system could be affordable for water treatment in rural communities where centralized water treatment and distribution system cannot be implemented. Magnetic separation technique of magnetic composites is easy and rapid, requiring simple device, and possible to

the automation. These techniques might be utilized for resource recovery from aqueous solution and/or waste water, valuable metals or nutrients that are recovered can be used as industrial raw material or agricultural fertilizer.

9.2. Recommendations

The following recommendations are made for the future researches on magnetic composites as adsorbents for water purification:

1. Dispersion of nanoparticles in synthesizing of nanocomposite material is the key factor influencing its efficiency for contaminant removal. Additional studies on the development of methods and machineries for nanoparticles dispersion such as dispersing agent and ultrasonic processor are required.
2. Combined with iron oxide nanoparticles, dispersivity of CNTs was improved and CNTs were easily fabricated as filter type. The efficiency of particulate removal by iron oxide nanoparticles doped CNTs can be enhanced. Further studies are necessary to truly understand the advantage of CNTs/iron oxide nanocomposites as compared to pristine carbon nanotube for water filtration at electromagnetic field.
3. Carbon nanotubes have superior physical strength as well as high removal capacity for various contaminants. CNTs can be affordable for water treatment system operated under high pressure and frequent chemical cleaning. Due to the regeneration of composites by chemical cleaning, the removal efficiency for long time operation should also be

investigated.

4. Currently, there are limited understanding of the human health and safety risks associated with nanomaterials. Dynamic light scattering (DLS) method is a physical technique for measuring the degree of light scattering as function of time that can be used to the size distribution of particles in solution. Intensive research for preventing outflow of nanomaterials using this technology is necessary.

REFERENCES

- Adamson, GCD; Polya, DA. 2007. Critical pathway analysis to determine key uncertainties in net impacts on disease burden in Bangladesh of arsenic mitigation involving the substitution of surfacewater for groundwater drinking water supplies. *Journal of Environmental Science and Health, Part A*, 42: 1909–1917.
- Adriano, DC. 2001. Trace elements in terrestrial environments: biogeochemistry, bioavailability, and risks of metals. *Springer-Verlag NY*, 2nd.
- Ahmad, SA; Sayed, MHS; Khan, MH; Karim, MN; Haque, MA; Bhuiyan, MSA; Rahman, MS; Faruquee, MH. 2007. Sociocultural aspects of arsenicosis in Bangladesh: community perspective. *Journal of Environmental Science and Health, Part A*, 2007, 42: 1945–1958.
- Ai, L; Li, M; Li, L. 2011. Adsorption of methylene blue from aqueous solution with activated carbon/cobalt ferrite/alginate composite beads: kinetics, isotherms, and thermodynamics. *Journal of Chemical and Engineering data*, 56: 3475–3483.
- Ai, L; Zhang, C; Liao, F; Wang, Y; Li, M; Meng, L; Jiang, J. 2011. Removal of methylene blue from aqueous solution with magnetite loaded multi-wall carbon nanotube: kinetic, isotherm and mechanism analysis. *Journal of Hazardous Materials*, 198: 282–290.
- Albert, M; Demesmay, C; Roeca, JL. 1995. Analysis of organic and non-organic arsenious or selenious compounds by capillary electrophoresis. *Fresenius Journal of Analytical Chemistry*, 351:426–432.
- Ambashta, RD; Sillanpää, M. 2010. Water purification using magnetic assistance: a review. *Journal of Hazardous Materials*, 180: 38–49.
- An, YJ; Lee, JK; Cho, S. 2007. Korean water quality standards for the protection of human health and aquatic life. *The 2nd International WEPA Forum (International Forum on Water Environmental Governance in Asia)*.
- APHA (American Public Health Association). 1995. Standard methods for the examination of water and wastewater. Washington, DC.
- Appel, C; Ma, LQ; Rhue, RD; Kennelley, E. 2003. Point of zero charge

determination in soils and minerals via traditional methods and detection of electroacoustic mobility. *Geoderma*, 113: 77-93.

- Arica, MY; Akyol, AB; Bayramoglu, G. 2008. Adsorption of trypsin onto magnetic ion-exchange beads of poly(glycidylmethacrylate-co-ethyleneglycoldimethacrylate). *Journal of Applied Polymer Science*, 107: 2810–2819.
- Badreddine, M; Legrouri, A; Barroug, A; De Roy, A; Besse, JP. 1999. Ion exchange of different phosphate ions into the zincaluminum-chloride layered double hydroxide. *Materials Letters*, 38: 391–395.
- Badruddoza, AZM; Tay, ASH; Tan, PY; Hidajat, K; Uddin, MS. 2011. Carboxymethylb-cyclodextrin conjugated magnetic nanoparticles as nano-adsorbents for removal of copper ions: synthesis and adsorption studies. *Journal of Hazardous Materials*, 185: 1177–1186.
- Bajpai, SK; Armo, MK. 2009. Equilibrium sorption of hexavalent chromium from aqueous solution using iron(III)-loaded chitosan-magnetite nanocomposites as novel sorbent. *Journal of Macromolecular Science, Part A* 46: 510-520.
- Balistrieri, LS; Chao, TT. 1990. Adsorption of selenium by amorphous iron oxyhydroxide and manganese dioxide. *Geochimica et Cosmochimica Acta*, 54: 739–751.
- Banert, T; Peuker, UA. 2007. Synthesis of magnetic beads for bio-separation using the solution method. *Chemical Engineering Communications*, 194: 707–719.
- Bang, S; Meng, X. 2004. A review of arsenic interactions with anions and iron hydroxides. *Environmental Engineering Research*, 9: 184–192.
- Bao, J; Liang, Y; Xu, Z; Si, L. 2003. Facile synthesis of hollow nickel submicrometer spheres. *Advanced Materials*, 15: 1832–1835.
- Bayramoglu, G; Arica, MY. 2007. Kinetics of mercury ions removal from synthetic aqueous solutions using by novel magnetic p(GMA-MMA-EGDMA) beads. *Journal of Hazardous Materials*, 144: 449–457.
- Bee, Agnes; Talbot, D; Abramson, S; Dupuis, V. 2011. Magnetic alginate beads for Pb(II) ions removal from wastewater. *Journal of Colloid and Interface Science*, 362: 486–492.

- Bhutani, MM; Mitra, AK; Kumari, R. 1992. Kinetic study of Cr(VI) sorption on MnO₂. *Journal of Radioanalytical and Nuclear Chemistry*, 157: 75–86.
- Bielicka, A; Bojanowska, I; Wiśniewski, A. 2005. Sequential extraction of chromium from galvanic wastewater sludge. *Polish Journal of Environmental Studies*, 14: 145–148.
- Brechbühl, Y; Christl, I; Elzinga, EJ; Kretzschmar, R. 2012. Competitive sorption of carbonate and arsenic to hematite: combined ATR-FTIR and batch experiments. *Journal of Colloid and Interface Science*, 377: 313–321.
- Briggs, D; Seah, MP. 1983. Practical surface analysis. *John Wiley and Sons*, New York.
- Carriazo, D; del Arco, M; Martín, C; Rives, V. 2007. A comparative study between chloride and calcined carbonate hydrotalcites as adsorbents for Cr(VI). *Applied Clay Science*, 37: 231–239.
- Cavani, F; Trifirb, F; Vaccari, A. 1991. Hydrotalcite-type anionic clays: preparation, properties and applications. *Catalysis Today*, 11: 173–301.
- Chan, CCP; Gallard, H; Majewski, P. 2012. Fabrication of amine-functionalized magnetite nanoparticles for water treatment processes. *Journal of Nanoparticle Research*, 14: 1-11.
- Chang, PR; Zheng, P; Liu, B; Anderson, DP; Yu, J; Ma, X. 2011. Characterization of magnetic soluble starch-functionalized carbon nanotubes and its application for the adsorption of the dyes. *Journal of Hazardous Materials*, 186: 2144–2150.
- Charlet, L; Scheinost, AC; Tournassat, C; Grenechee, JM; Ge'hin, A; Ferná'ndez-Martí'nez, A; Coudert, S; Tisserand, D; Brendle, J. 2007. Electron transfer at the mineral/water interface: selenium reduction by ferrous iron sorbed on clay. *Geochimica et Cosmochimica Acta*, 71: 5731–5749.
- Chen, C; Hu, J; Shao, D; Li, J; Wang, X. 2009. Adsorption behavior of multiwall carbon nanotube/iron oxide magnetic composites for Ni(II) and Sr(II). *Journal of Hazardous Materials*, 164: 923–928.
- Chen, C; Hu, J; Xu, D; Tan, X; Meng, Y; Wang, X. 2008. Surface complexation modeling of Sr(II) and Eu(III) adsorption onto oxidized multiwall carbon nanotubes. *Journal of Colloid and Interface Science*, 323: 33–41.

- Chen, C; Wang, X. 2006. Adsorption of Ni(II) from Aqueous Solution Using Oxidized Multiwall Carbon Nanotubes. *Industrial and Engineering Chemistry Research*, 45: 9144–9149.
- Chen, CL; Wang, XK; Nagatsu, M. 2009. Europium adsorption on multiwall carbon nanotube/iron oxide magnetic composite in the presence of polyacrylic acid. *Environmental Science and Technology*, 43: 2362–2367.
- Chen, M; Jiang, W; Wang, F; Shen, P; Ma, P; Gu, J; Mao, J; Li, F. 2013. Synthesis of highly hydrophobic floating magnetic polymer nanocomposites for the removal of oils from water surface. *Applied Surface Science*, 286: 249–256.
- Chen, R; Chai, L; Li, Q; Shi, Y; Wang, Y; Mohammad, A. 2013. Preparation and characterization of magnetic Fe₃O₄/CNT nanoparticles by RPO method to enhance the efficient removal of Cr(VI). *Environmental Science and Pollution Research*, 20:7175–7185.
- Chen, YL; Qian, H; Wu, F; Zhou, J. 2011. Clearance and recovery of Cd(II) from aqueous solution by magnetic separation technology. *Chemosphere*, 83: 1214–1219.
- Chitrakar, R; Tezuka, S; Sonoda, A; Sakane, K; Ooi, K; Hirotsu, T. 2005. Adsorption of phosphate from seawater on calcined MgMn-layered double hydroxides. *Journal of Colloid and Interface Science*, 290: 45–51.
- Chowdhury, SR; Yanful, EK. 2010. Arsenic and chromium removal by mixed magnetite–maghemite nanoparticles and the effect of phosphate on removal. *Journal of Environmental Management*, 91: 2238–2247.
- Coca, M; Mato, S; González-Benito, G; Ángel Urueña, M; García-Cubero, MT. 2010. Use of weak cation exchange resin Lewatit S 8528 as alternative to strong ion exchange resins for calcium salt removal. *Journal of Food Engineering*, 97: 569–573.
- Da Silva, FV; Yamaguchi, NU; Lovato, GA; Da Silva, FA; Reis, MHM; De Amorim, MTPS; Tavares, CRG; Bergamasco, R. 2012. Effects of coconut granular activated carbon pretreatment on membrane filtration in a gravitational driven process to improve drinking water quality. *Environmental Technology*, 33: 711–716.
- Das, J; Patra, BS; Baliarsingh, N; Parida, KM. 2006. Adsorption of phosphate by layered double hydroxides in aqueous solutions. *Applied Clay Science*,

32: 252–260.

- Denkbas, EB; Kilicay, E; Birlikseven, C; Ozturk, E. 2002. Magnetic chitosan microspheres: preparation and characterization. *Reactive and Functional Polymers*, 50: 225–232.
- Dobrowolski, R; Otto, M. 2013. Preparation and evaluation of Fe-loaded activated carbon for enrichment of selenium for analytical and environmental purposes. *Chemosphere*, 90: 683–690.
- Dong, CK; Li, X; Zhang, Y; Qi, JY; Yuan, YF. 2009. Fe₃O₄ nanoparticles decorated multi-walled carbon nanotubes and their sorption properties. *Chemical Research in Chinese Universities*, 25: 936–940.
- Donia, AM; Atia, AA; Elwakeel, KZ. 2008. Selective separation of mercury(II) using magnetic chitosan resin modified with Schiff's base derived from thiourea and glutaraldehyde. *Journal of Hazardous Materials*, 151: 372–379.
- Dudek, B; Kuśtrowski, P; Białas, A; Natkański, P; Piwowarska, Z; Chmielarz, L; Kozak, M; Michalik, M. 2012. Influence of textural and structural properties of Mg-Al and Mg-Zn-Al containing hydrotalcite derived oxides on Cr(VI) adsorption capacity. *Materials Chemistry and Physics*, 132: 929–936.
- Environment and work place health report. 2009. Water treatment devices for removal for taste odour and chemicals. Water Quality, Department of Health Canada.
- Fan, L; Luo, C; LV, Z; Lu, F; Qiu, H. 2011. Removal of Ag⁺ from water environment using a novel magnetic thiourea-chitosan imprinted Ag⁺. *Journal of Hazardous Materials*, 194: 193–201.
- Flanagan, SV; Meng, X; Zheng, Y. 2013. Increasing acceptance of chlorination for household water treatment: observations from Bangladesh. *Waterlines*, 32: 125–134.
- Foo, KY; Hameed, BH. 2010. Insights into the modeling of adsorption isotherm systems. *Chemical Engineering Journal*, 156: 2–10.
- Fox, KR. 1989. Field experience with point-of-use treatment systems for arsenic removal. *Journal / American Water Works Association*, 81: 94–101.
- Gauden, PA; Terzyk AP; Rychlicki, G; Kowalczyk, P; Lota, K; Raymundo-

- Pinero, E; Frackowiak, E; Béguin, F. 2006. Thermodynamic properties of benzene adsorbed in activated carbons and multi-walled carbon nanotubes. *Chemical Physics Letters*, 421: 409–414.
- Genz, A; Kornmüller, A; Jekel, M. 2004. Advanced phosphorus removal from membrane filtrates by adsorption on activated aluminium oxide and granulated ferric hydroxide. *Water Research*, 38: 3523–3530.
- Gimenez, J; Martinez, M; de Pablo, J; Rovira, M; Duro, L. 2007. Arsenic sorption onto natural hematite, magnetite, and goethite. *Journal of Hazardous Materials*, 141: 575–580.
- Goesmann, H.; Feldmann, C. 2010. Nanoparticulate functional materials. *Angewandte Chemie International Edition*, 49: 1362–1395.
- Goh, KH; Lim, TT. 2010. Influences of co-existing species on the sorption of toxic oxyanions from aqueous solution by nanocrystalline Mg/Al layered double hydroxide. *Journal of Hazardous Materials*, 180: 401–408.
- Goh, KH; Lim, TT; Banas, A; Dong, Z. 2010. Sorption characteristics and mechanisms of oxyanions and oxyhalides having different molecular properties on Mg/Al layered double hydroxide nanoparticles. *Journal of Hazardous Materials*, 179: 818–827.
- Goh, KH; Lim, TT; Dong, Z. 2008. Application of layered double hydroxides for removal of oxyanions: a review. *Water Research*, 42: 1343-1368.
- Gong, JL; Wang, B; Zeng, GM; Yang, CP; Niu, CG; Niu, QY; Zhou, WJ; Liang, Y. 2009. Removal of cationic dyes from aqueous solution using magnetic multi-wall carbon nanotube nanocomposite as adsorbent. *Journal of Hazardous Materials*, 164: 1517–1522.
- Goswamee, RL; Sengupta, P; Bhattacharyya, KG; Dutta, DK. 1998. Adsorption of Cr(VI) in layered double hydroxides. *Applied Clay Science*, 13: 21–34.
- Goswami, A; Purkait, MK. 2011. Kinetic and equilibrium study for the fluoride adsorption using pyrophyllite. *Separation Science and Technology*, 46: 1797–1807.
- Greenleaf, JE; Lin, JC; Sengupta, AK. 2006. Two novel applications of ion exchange fibers: Arsenic removal and chemical-free softening of hard water. *Environmental Progress*, 25: 300–311.

- Gregorio-Jauregui, KM; Pineda, MG; Rivera-Salinas, JE; Hurtado, G; Saade, H; Martinez, JL; Ilyina, A; Lopez, RG. 2012. One-step method for preparation of magnetic nanoparticles coated with chitosan. *Journal of Nanomaterials*, 2012: 1–8.
- Guan, Y; Jiang, C; Hu, C; Jia, L. 2010. Preparation of multi-walled carbon nanotubes functionalized magnetic particles by sol–gel technology and its application in extraction of estrogens. *Talanta*, 83: 337–343.
- Gupta, SS; Bhattacharyya, KG. 2011. Kinetics of adsorption of metal ions on inorganic materials: a review. *Advances in Colloid and Interface Science*, 162: 39–58.
- Gupta, VK; Agarwal, S; Saleh, TA. 2011. Chromium removal by combining the magnetic properties of iron oxide with adsorption properties of carbon nanotubes. *Water Research*, 45: 2207–2212.
- Gupta, VK; Agarwal, S; Saleh, TA. 2011. Synthesis and characterization of alumina-coated carbon nanotubes and their application for lead removal. *Journal of Hazardous Materials*, 185: 17–23.
- Halsey, G. 1948. Physical adsorption on non-uniform surfaces. *Journal of Chemical Physics*, 16: 931–937.
- Han, DS; Batchelor, B; Abdel-Wahab, A. 2013. XPS analysis of sorption of selenium(IV) and selenium(VI) to mackinawite (FeS). *Environmental Progress and Sustainable Energy*, 32: 84–93.
- Han, DS; Song, JK; Batchelor, B; Abdel-Wahab, A. 2013. Removal of arsenite(As(III)) and arsenate(As(V)) by synthetic pyrite (FeS₂): synthesis, effect of contact time, and sorption/desorption envelopes. *Journal of Colloid and Interface Science*, 392: 311–318.
- Han, YU; Lee, WS; Lee, CG; Park, SJ; Kim, KW; Kim, SB. 2011. Entrapment of Mg-Al layered double hydroxide in calcium alginate beads for phosphate removal from aqueous solution. *Desalination and Water Treatment*, 36: 178–186.
- Hansen, JE. 2005. A slippery slope: “How much global warming constitutes dangerous anthropogenic interference”?. *Climatic Change*, 68: 269–279.
- Hayashi, H; Kanie, K; Shinoda, K; Muramatsu, A; Suzuki, S; Sasaki, H. 2009. pH-dependence of selenate removal from liquid phase by reductive Fe(II)–Fe(III) hydroxysulfate compound, green rust. *Chemosphere*, 76: 638–643.

- Hu, J; Chen, C; Zhu, X; Wang, X. 2009. Removal of chromium from aqueous solution by using oxidized multiwalled carbon nanotubes. *Journal of Hazardous Materials*, 162: 1542–1550.
- Hu, J; Chen, G; Lo, IMC. 2005. Removal and recovery of Cr(VI) from wastewater by maghemite nanoparticles. *Water Research*, 39: 4528–4536.
- Hu, J; Lo, IMC; Chen, G. 2007. Performance and mechanism of chromate(VI) adsorption by δ -FeOOH-coated maghemite (γ -Fe₂O₃) nanoparticles. *Separation and Purification Technology*, 58: 76-82.
- Hu, J; Shao, D; Chen, C; Sheng, G; Li, J; Wang, X; Nagatsu, M. 2010. Plasma-Induced Grafting of Cyclodextrin onto Multiwall Carbon Nanotube/Iron Oxides for Adsorbent Application. *The Journal of Physical Chemistry B*, 114: 6779–6785.
- Hu, J; Shao, D; Chen, C; Sheng, G; Ren, X; Wang, X. 2011. Removal of 1-naphthylamine from aqueous solution by multiwall carbon nanotubes/iron oxides/cyclodextrin composite. *Journal of Hazardous Materials*, 185: 463–471.
- Hu, J; Yang, S; Wang, X. 2012. Adsorption of Cu(II) on β -cyclodextrin modified multiwall carbon nanotube/iron oxides in the absence/presence of fulvic acid. *Journal of Chemical Technology and Biotechnology*, 87: 673–681.
- Hu, J; Zhao, D; Wang, X. 2011. Removal of Pb(II) and Cu(II) from aqueous solution using multiwalled carbon nanotubes/iron oxide magnetic composites. *Water Science and Technology*, 63:917–923.
- Hu, L; Hach, D; Chaumont, D; Brachais, CH; Couvercelle, JP. 2008. One step grafting of monomethoxy poly(ethylene glycol) during synthesis of maghemite nanoparticles in aqueous medium. *Colloids and Surfaces A: Physicochemical and Engineering Aspects*, 330: 1-7.
- Hu, X; Liu, B; Deng, Y; Chen, H; Luo, S; Sun, C; Yang, P; Yang, S. 2011. Adsorption and heterogeneous Fenton degradation of 17 α -methyltestosterone on nano Fe₃O₄/MWCNTs in aqueous solution. *Applied Catalysis B: Environmental*, 107: 274–283.
- Huang, JC; Suárez, MC; Yang, SI; Lin, ZQ; Terry, N. 2013. Development of a constructed wetland water treatment system for selenium removal: incorporation of an algal treatment component. *Environmental Science and Technology*, 47: 10518–10525.

- Idris, A; Hassan, N; Rashid, R; Ngomsik, AF. 2011. Kinetic and regeneration studies of photocatalytic magnetic separable beads for chromium (VI) reduction under sunlight. *Journal of Hazardous Materials*, 186: 629–635.
- Idris, A; Ismail, NSM; Hassan, N; Misran, E; Ngomsik, AF. 2012. Synthesis of magnetic alginate beads based on maghemite nanoparticles for Pb(II) removal in aqueous solution. *Journal of Industrial and Engineering Chemistry*, 18: 1582–1589.
- Idris, A; Misran, E; Hassan, N; Jalil, AA; Seng, CE. 2012. Modified PVA-alginate encapsulated photocatalyst ferro photo gels for Cr(VI) reduction. *Journal of Hazardous Materials*, 227-228: 309–316.
- Iijima S. 1991. Helical microtubules of graphitic carbon. *Nature*, 354: 56–58.
- Ji, L; Zhou, L; Bai, X; Shao, Y; Zhao, G; Qu, Y; Wang, Cong; Li, Y. 2012. Facile synthesis of multiwall carbon nanotubes/iron oxides for removal of tetrabromobisphenol A and Pb(II). *Journal of Materials Chemistry*, 22: 15853–15862.
- Jiang, R; Yao, J; Zhu, H; Fu, Y; G, Y; Xiao, L; Zeng, G. 2013. Effective decolorization of congo red in aqueous solution by adsorption and photocatalysis using novel magnetic alginate/ γ -Fe₂O₃/CdS nanocomposite. *Desalination and Water Treatment*. In press.
- Jiang, W; Chen, X; Niu, Y; Pan, B. 2012. Spherical polystyrene-supported nano-Fe₃O₄ of high capacity and low-field separation for arsenate removal from water. *Journal of Hazardous Materials*, 243: 319–325.
- Jordan, N; Müller, K; Franzen, C; Brendler, V. 2013. Temperature impact on the sorption of selenium(VI) onto anatase. *Journal of Colloid and Interface Science*, 390: 170–175.
- Kanezaki, E. 1998. A thermally induced metastable solid phase of Mg/Al-layered double hydroxides by means of in situ high temperature powder X-ray diffraction. *Journal of Materials Science Letters*, 17: 371–374.
- Khajeh, M; Laurent, S; Dastafkan, K. 2013. Nanoadsorbents: classification, preparation, and applications (with emphasis on aqueous media). *Chemical Reviews*, 113: 7728–7768.
- Kim, IT; Nunnery, GA; Jacob, K; Schwartz, J; Liu, X; Tannenbaum, R. 2010. Synthesis, characterization, and alignment of magnetic carbon nanotubes tethered with maghemite nanoparticles. *Journal of Physical Chemistry C*,

114: 6944-6951.

- Kim, IT; Tannenbaum, A; Tannenbaum, R. 2011. Anisotropic conductivity of magnetic carbon nanotubes embedded in epoxy matrices. *Carbon*, 49: 54–61.
- Kim, JH; Kim, JH; Bokare, V; Kim, EJ; Chang, YY; Chang, YS. 2012. Enhanced removal of chromate from aqueous solution by sequential adsorption-reduction on mesoporous iron-iron oxide nanocomposites. *Journal of Nanoparticle Research*, 14: 1010.
- Kim, SS; Min, JH; Lee, JK; Baik, MH; Choi, JW; Shin, HS. 2012. Effects of pH and anions on the sorption of selenium ions onto magnetite. *Journal of Environmental Radioactivity*, 104: 1–6.
- Koilraj, P; Kannan, S. 2009. Phosphate uptake behavior of ZnAlZr ternary layered double hydroxides through surface precipitation. *Journal of Colloid and Interface Science*, 341: 289–297.
- Kruawal, K; Sacher, F; Werner, A; Muller, J; Knepper, TP. 2005. Chemical water quality in Thailand and its impacts on drinking water production in Thailand. *Science of the Total Environment*, 340: 57–70.
- Kurniawan, TA; Lo, WH. 2009. Removal of refractory compounds from stabilized landfill leachate using an integrated H₂O₂ oxidation and granular activated carbon (GAC) adsorption treatment. *Water Research*, 43: 4079–4091.
- Kurniawan, TA; Sillanpää, MET; Sillanpää, M. 2012. Nanoadsorbents for remediation of aquatic environment: local and practical solutions for global water pollution problems. *Critical Reviews in Environmental Science and Technology*, 42:1233–1295.
- Labaran, BA; Vohra, MS. 2013. Photocatalytic removal of selenite and selenate species: effect of EDTA and other process variables. *Environmental Technology*, in press.
- Lee, CG; Kim, SB. 2013. Magnetic alginate-layered double hydroxide composites for phosphate removal. *Environmental Technology*, 34: 2749–2756.
- Lee, SB; Boo, JH. 1990. Principles and application of x-ray photoelectron spectroscopy. *Journal of the Korean Institute of Surface Engineering*, 23: 183–193.

- Lee, SY; Park, SJ. 2012. Influence of the pore size in multi-walled carbon nanotubes on the hydrogen storage behaviors. *Journal of Solid State Chemistry*, 194: 307–312.
- Li, H; Bi, S; Liu, L; Dong, W; Wang, X. 2011. Separation and accumulation of Cu(II), Zn(II) and Cr(VI) from aqueous solution by magnetic chitosan modified with diethylenetriamine. *Desalination*, 278: 397–404.
- Li, H; Li, Z; Liu, T; Xiao, X; Peng, Z; Deng, L. 2008. A novel technology for biosorption and recovery hexavalent chromium in wastewater by bio-functional magnetic beads. *Bioresource Technology*, 99: 6271–6279.
- Li, J; Chen, C; Zhao, Y; Hu, J; Shao, D; Wang, X. 2013. Synthesis of water-dispersible Fe₃O₄@ β -cyclodextrin by plasma-induced grafting technique for pollutant treatment. *Chemical Engineering Journal*, 229: 296–303.
- Li, X; Qi, Y; Li, Y; Zhang, Y; He, X; Wang, Y. 2013. Novel magnetic beads based on sodium alginate gel crosslinked by zirconium(IV) and their effective removal for Pb²⁺ in aqueous solutions by using a batch and continuous systems. *Bioresource Technology*, 142: 611–619.
- Li, XM; Xu, G; Liu, Y; He, T. 2011. Magnetic Fe₃O₄ nanoparticles: synthesis and application in water treatment. *Nanoscience and Nanotechnology-Asia*, 1: 14–24.
- Li, XQ; Cao, J; Zhang, WX. 2008. Stoichiometry of Cr(VI) immobilization using nanoscale zerovalent iron (nZVI): a study with high-resolution X-ray photoelectron spectroscopy (HR-XPS). *Industrial & Engineering Chemistry Research*, 47: 2131-2139.
- Li, YH; Wang, S; Wei, J; Zhang, X; Xu, C; Luan, Z; Wu, D; Wei, B. 2002. Lead adsorption on carbon nanotubes. *Chemical Physics Letters*, 357: 263–266.
- Lito, PF; Aniceto, JPS; Silva, CM. 2012. Removal of anionic pollutants from waters and wastewaters and materials perspective for their selective sorption. *Water, Air, and Soil Pollution*, 223:6133–6155.
- Lo, HM; Kurniawan, TA; Sillanpää, MET; Pai, TZ; Liu, MH; Banks, CJ; Wang, SC; Chiang, CF; Lin, KC; Liu, WF; Cheng, PH; Chen, JK; Chiu, HY; Wu, HY. 2010. Modeling biogas production from organic fractions of MSW co-digested with MSWI incinerator ashes in anaerobic bioreactors. *Bioresource Technology*, 101: 6329–6335.
- Long, RQ; Yang, RT. 2001. Carbon Nanotubes as Superior Sorbent for Dioxin

- Removal. *Journal of the American Chemical Society*, 123: 2058–2059.
- Loyo, RL; Nikitenko, SI; Scheinost, AC; Simonoff, M.. 2008. Immobilization of selenite on Fe₃O₄ and Fe/Fe₃C ultrasmall particles. *Environmental Science and Technology*, 42: 2451–2456.
- Lu, C; Chiu, H. 2008. Chemical modification of multiwalled carbon nanotubes for sorption of Zn²⁺ from aqueous solution. *Chemical Engineering Journal*, 139: 462–468.
- Lu, C; Su, F; Hu, S. 2008. Surface modification of carbon nanotubes for enhancing BTEX adsorption from aqueous solutions. *Applied Surface Science*, 254: 7035–7041.
- Lu, S; Chen, L; Dong, Y; Chen, Y. 2011. Adsorption of Eu(III) on iron oxide/multiwalled carbon nanotube magnetic composites. *Journal of Radioanalytical and Nuclear Chemistry*, 288: 587–593.
- Ma, J; Zhu, Z; Chen, B; Yang, M; Zhou, H; Li, C; Yu, F; Chen, J. 2013. One-pot, large-scale synthesis of magnetic activated carbon nanotubes and their applications for arsenic removal. *Journal of Materials Chemistry A*, 1: 4662–4666.
- Martinez, M; Gimenez, J; de Pablo, J; Rovira, M; Duro, L. 2006. Sorption of selenium(IV) and selenium(VI) onto magnetite. *Applied Surface Science*, 252: 3767–3773.
- Mayo, JT; Yavuz, C; Yean, S; Cong, L; Shipley, H; Yu, W; Falkner, J; Kan, A; Tomson, M; Colvin, VL. 2007. The effect of nanocrystalline magnetite size on arsenic removal. *Science and Technology of Advanced Materials*, 8: 71–75.
- Meng, F; Chae, SR; Drews, A; Kraume, M; Shin, HS; Yang, F. 2009. Recent advances in membrane bioreactors (MBRs): membrane fouling and membrane material. *Water Research*, 43: 1489–1512.
- Müller, C; Preußner-Kunze, A; Wagner, K; Franzreb, M. 2011. Gonadotropin purification from horse serum applying magnetic beads. *Biotechnology Journal*, 6: 392–395.
- Muller, M; Anke, M; Hartmann, E; Lilling, H. 1995. The occurrence of heavy metals (Cd, Pb, Ni) in drinking water. *Toxicology Letters*, 78: 58.
- Mullet, M; Boursiquot, S; Ehrhardt, JJ. 2004. Removal of hexavalent

chromium from solutions by mackinawite, tetragonal FeS. *Colloids and Surfaces A: Physicochem. Eng. Aspects*, 244: 77-85.

Naveau, A; Monteil-Rivera, F; Guillon, E; Dumonceau, J. 2007. Interactions of Aqueous selenium (-II) and (IV) with metallic sulfide surfaces, *Environmental Science and Technology*, 41: 5376–5382.

Ngomsik, AF; Bee, A; Siaugue, JM; Cabuil, V; Cote, G. 2006. Nickel adsorption by magnetic alginate microcapsules containing an extractant. *Water Research*, 40: 1848–1856.

Ngomsik, AF; Bee, A; Siaugue, JM; Talbot, D; Cabuil, V; Cote, G. 2009. Co(II) removal by magnetic alginate beads containing Cyanex 272[®]. *Journal of Hazardous Materials*, 166: 1043–1049.

NIST. 2013. X-ray Photoelectron spectroscopy database (<http://srdata.nist.gov/xps/>)

NNI. 2008. Nanotechnology: big things from a tiny. (<http://www.nano.gov/>).

Ntim, SA; Mitra, S. 2011. Removal of trace arsenic to meet drinking water standards using iron oxide coated multiwall carbon nanotubes. *Journal of Chemical and Engineering Data*, 56: 2077–2083.

Olegario, JT; Yee, N; Miller, M; Sczepaniak, J; Manning, B. 2010. Reduction of Se(VI) to Se(-II) by zerovalent iron nanoparticle suspensions. *Journal of Nanoparticle Research*, 12: 2057–2068.

Oliveira, M; Machado, AV; Nogueira R. 2012. Phosphorus removal from eutrophic waters with an aluminium hybrid nanocomposite. *Water, Air, and Soil Pollution*, 223: 4831–4840.

Ookubo, A; Ooi, K; Hayashi, H. Preparation and phosphate ion-exchange properties of a hydrotalcite-like compound. *Langmuir*, 9: 1418-1422.

Ozturk, N; Gunay, ME; Akgol, S; Denizli, A. 2007. Silane-modified magnetic beads: application to immunoglobulin-G separation. *Biotechnology Progress*, 23: 1149–1156.

Pan, S; Shen, H; Xu, Q; Luo, J; Hu, M. 2012. Surface mercapto engineered magnetic Fe₃O₄ nanoadsorbent for the removal of mercury from aqueous solutions. *Journal of Colloid and Interface Science*, 365: 204–212.

Peng, X; Li, Y; Luan, Z; Di, Z; Wang, H; Tian, B; Jia, Z. 2003. Adsorption of 1,2-dichlorobenzene from water to carbon nanotubes. *Chemical Physics*

Letters, 376: 154–158.

- Peng, X; Luan, Z; Di, Z; Zhang, Z; Zhu, C. 2005. Carbon nanotubes-iron oxides magnetic composites as adsorbent for removal of Pb(II) and Cu(II) from water. *Carbon*, 43: 855–894.
- Peng, X; Xu, F; Zhang, W; Wang, J; Zeng, C; Niu, M; Chmielewska, E. 2014. Magnetic Fe₃O₄@silica-xanthan gum composites for aqueous removal and recovery of Pb²⁺. *Colloids and Surfaces A: Physicochemical and Engineering Aspects*, 443: 27–36.
- Pianta, R; Boller, M; Urfer, D; Chappaz, A; Gmunder, A. 2000. Costs of conventional vs. membrane treatment for karstic spring water. *Desalination*, 131: 245–255.
- Pradeep, T; Anshup. 2009. Noble metal nanoparticles for water purification: a critical review. *Thin Solid Films*, 517: 6441–6478.
- Prasanna, SV; Kamath PV. 2008. Chromate uptake characteristics of the pristine layered double hydroxides of Mg with Al. *Solid State Sciences*, 10: 260–266.
- Prasanna, SV; Rao RAP; Kamath, PV. 2006. Layered double hydroxides as potential chromate scavengers. *Journal of Colloid and Interface Science*, 304: 292–299.
- Qu, S; Huang, F; Yu, S; Chen, G; Kong, J. 2008. Magnetic removal of dyes from aqueous solution using multi-walled carbon nanotubes filled with Fe₂O₃ particles. *Journal of Hazardous Materials*, 160: 643–647.
- Rao, PG; Lu, C; Su, F. 2007. Sorption of divalent metal ions from aqueous solutions by carbon nanotubes: a review. *Separation and Purification Technology*, 58: 224–231.
- Ren, X; Yang, S; Shao, D; Tan, X. 2013. Retention of Pb(II) by a low-cost magnetic composite prepared by environmentally friendly plasma technique. *Separation Science and Technology*, 48: 1211–1219.
- Rhee, SW; Kang, MJ; Kim H; Moon, CH. 1997. Removal of aquatic chromate ion involving rehydration reaction of calcined layered double hydroxide (Mg-Al-CO₃). *Environmental Technology*, 18: 231–236.
- Richard, FC; Bourg, ACM. 1991. Aqueous geochemistry of chromium: a review. *Water Research*, 25: 807–816.

- Roche, V; Siaugue, JM; Cabuil, V; Bee, A. 2008. Removal of organic dyes by magnetic alginate beads. *Water Research*, 42: 1290–1298.
- Rovira, M; Gimenez, J; Martinez, M; Martinez-Llado, X; de Pablo, J; Marti, V; Duro, L. 2008. Sorption of selenium(IV) and selenium(VI) onto natural iron oxides: goethite and hematite. *Journal of Hazardous Materials*, 150: 279–284.
- RSC. 2007. Sustainable water: chemical science priorities. (<http://www.rsc.org>).
- Sanlier, SH; Ak, G; Yilmaz, H; Ozbakir, G; Cagliyan, O. 2013. Removal of textile dye, direct red 23, with glutaraldehyde cross-linked magnetic chitosan beads. *Preparative Biochemistry and Biotechnology*, 43: 163–176.
- Sasaki, K; Blowes, DW; Ptacek, CJ. 2008. Spectroscopic study of precipitates formed during removal of selenium from mine drainage spiked with selenate using permeable reactive materials. *Geochemical Journal*, 42: 283–294.
- Sayin, S; Ozcan, F; Yilmaz, M. 2013. Two novel calixarene functionalized iron oxide magnetite nanoparticles as a platform for magnetic separation in the liquid–liquid/solid–liquid extraction of oxyanions. *Materials Science and Engineering: C*, 33: 2433–2439.
- Scheinost, AC; Charlet, L. 2008. Selenite reduction by mackinawite, magnetite and siderite: XAS characterization of nanosized redox products. *Environmental Science and Technology*, 42: 1984–1989.
- Seida, Y; Nakano, Y. 2002. Removal of phosphate by layered double hydroxides containing iron. *Water Research*, 36: 1306–1312.
- Senel, S; Uzun, L; Kara, A; Denizli, A. 2008. Heavy metal removal from synthetic solutions with magnetic beads under magnetic field. *Journal of Macromolecular Science, Part A: Pure and Applied Chemistry*, 45: 635–642.
- Sharma, S K; Petrushevski, B; Amy, G. 2011. Chromium removal from water: a review. *Journal of Water Supply: Research and Technology*, 171: 811–840.
- Shibasaki, N; Lei, P; Kamata, A. 2007. Evaluation of deep groundwater development for arsenic mitigation in western Bangladesh. *Journal of Environmental Science and Health, Part A*, 42: 1919–1932.

- Siegbahn, K; Nordling, C; Fahlman, A; Nordberg, R; Hamrin, K; Hedman, J; Johansson, G; Bergmark, T; Karlsson, SE; Lindgren, I; Lindberg, B. 1967. ESCA: atomic, molecular and solid state structure studied by means of electron spectroscopy. *Nova Acta Regiae Societatis Scientiarum Upsaliensis, Ser IT, Vol. 20.*
- Sillanpaa, M; Kurniawan, TA; Lo, WH. 2011. Degradation of chelating agents in aqueous solution using advanced oxidation process. *Chemosphere*, 83: 1443–1460.
- Sun, SH; Murray, CB; Weller, D; Folks, L; Moser, A. 2000. Monodisperse FePt nanoparticles and ferromagnetic FePt nanocrystal superlattices, *Science*, 287: 1989–1992.
- Sun, Z; Liu, Z; Wang, Y; Han, B; Du, J; Zhang, J. 2005. Fabrication and characterization of magnetic carbon nanotube composites. *Journal of Materials Chemistry*, 15: 4497-4501.
- Tan, X; Fang, M; Chen, C; Yu, S; Wang, X. 2008. Counterion effects of nickel and sodium dodecylbenzene sulfonate adsorption to multiwalled carbon nanotubes in aqueous solution. *Carbon*, 46: 1741–1750.
- Tang, SCN; Lo, IMC. 2013. Magnetic nanoparticles: essential factors for sustainable environmental applications. *Water Research*, 47: 2613–2632.
- Tessier, A; Campbell, PGC; Bisson, M. 1979. Sequential extraction procedure for the speciation of particulate trace metals. *Analytical Chemistry*, 51: 844–851.
- Thomson, BM; Cotter, TJ; Chwirka, JD. 2003. Design and operation of point-of-use treatment system for arsenic removal. *Journal of Environmental Engineering*, 129: 561–564.
- Tran, HV; Tran, LD, Nguyen, TN. 2010. Preparation of chitosan/magnetite composite beads and their application for removal of Pb(II) and Ni(II) from aqueous solution. *Materials Science and Engineering C*, 30: 304–310.
- Tuzen, M; Sari, A. 2010. Biosorption of selenium from aqueous solution by green algae (*Cladophora hutchinsiae*) biomass: equilibrium, thermodynamic and kinetic studies. *Chemical Engineering Journal*, 158: 200–206.
- Tzou, YM; Wang, SL; Hsu, LC; Chang RR; Lin, C. 2007. Deintercalation of Li/Al LDH and its application to recover adsorbed chromate from used

- adsorbent. *Applied Clay Science*, 37: 107–114.
- Upadhyayula, VKK; Deng, S; Mitchell, MC; Smith, GB. 2009. Application of carbon nanotube technology for removal of contaminants in drinking water: a review. *Science of the Total Environment*, 408: 1–13.
- Uzun, L; Kara, A; Osman, B; Yilmaz, E; Besirli, N; Denizli, A. 2009. Removal of heavy-metal ions by magnetic beads containing triazole chelating groups. *Journal of Applied Polymer Science*, 114: 2246–2253.
- Velickovic, Z; Vukovic, GD; Marinkovic, AD; Moldovan, MS; Peric-Grujic, AA; Uskokovic, PS; Ristic, MD. 2012. Adsorption of arsenate on iron(III) oxide coated ethylenediamine functionalized multiwall carbon nanotubes. *Chemical Engineering Journal*, 181-182: 174–181.
- Volynsky, AB; Stakheev, AY; Telegina, NS; Senin, VG; Kustov, LM; Wennrich, R. 2001. Low-temperature transformations of sodium sulfate and sodium selenite in the presence of pre-reduced palladium modifier in graphite furnaces for electrothermal atomic absorption spectrometry. *Spectrochimica Acta Part B*, 56: 1387–1396.
- Wakur, Y; Persulesy, AE; Ikeda, T; Ebina, T; Onodera, Y; Suzuki, TM. 2005. Separation and enrichment of arsenic(V) with composite resin beads containing magnetite crystals. *Analytical Sciences*, 21: 433–435.
- Wan, J; Cai, W; Feng, J; Meng, X; Liu, E. 2007. In situ decoration of carbon nanotubes with nearly monodisperse magnetite nanoparticles in liquid polyols, *Journal of Materials Chemistry*, 17: 1188–1192.
- Wang, FQ; Li, P; Zhang, JP; Wang, AQ; Wei, Q. 2010. A novel pH-sensitive magnetic alginate-chitosan beads for albendazole delivery. *Drug Development and Industrial Pharmacy*, 36: 867–877.
- Wang, H; Lin, KY; Jing, B; Krylova, G; Sigmon, GE; McGinn, P; Zhu, Y; Na, C. 2013. Removal of oil droplets from contaminated water using magnetic carbon nanotubes. *Water Research*, 47: 4198–4205.
- Wang, H; Yan, N; Li, Y; Zhou, X; Chen, J; Yu, B; Gong, M; Chen, Q. 2012. Fe nanoparticle-functionalized multi-walled carbon nanotubes: one-pot synthesis and their applications in magnetic removal of heavy metal ions. *Journal of Materials Chemistry*, 22: 9230–9236.
- Wang, Q; Li, J; Chen, C; Ren, X; Hu, J; Wang, X. 2011. Removal of cobalt from aqueous solution by magnetic multiwalled carbon nanotube/iron

- oxide composites. *Chemical Engineering Journal*, 174: 126–133.
- Wang, SG; Gong, WX; Liu, XW; Yao, YW; Gao, BY; Yue, QY. 2007. Removal of lead(II) from aqueous solution by adsorption onto manganese oxide-coated carbon nanotubes. *Separation and Purification Technology*, 58: 17–23.
- Wang, X; Zhao, C; Zhao, P; Dou, P; Ding, Y; Xu, P. 2009. Gellan gel beads containing magnetic nanoparticles: an effective biosorbent for the removal of heavy metals from aqueous system. *Bioresource Technology*, 100: 2301–2304.
- Wang, XS; Zhu, L; Lu, HJ. 2011. Surface chemical properties and adsorption of Cu (II) on nanoscale magnetite in aqueous solutions. *Desalination*, 276: 154–160.
- Wang, Y; Han, T; Xu, Z; Bao, G; Zhu, T. 2005. Optimization of phosphorus removal from secondary effluent using simplex method in Tianjin, China. *Journal of Hazardous Materials*, 121: 183–186.
- Wei, H; Xu, L; Ren, J; Jia, L. 2012. Adsorption of bilirubin to magnetic multi-walled carbon nanotubes as a potential application in bound solute dialysis. *Colloids and Surfaces A: Physicochemical and Engineering Aspects*, 405: 38–44.
- Wei, X; Bhojappa, S; Lin, LS; Viadero, RC. 2012. Performance of nano-magnetite for removal of selenium from aqueous solutions. *Environmental Engineering Science*, 29: 526–532.
- Wu, D; Zhang, L; Wang, L; Zhu, B; Fan, L. 2011. Adsorption of lanthanum by magnetic alginate-chitosan gel beads. *Journal of Chemical Technology and Biotechnology*, 86: 345–352.
- Wu, W; He, Q; Jiang, C. 2008. Magnetic iron oxide nanoparticles: synthesis and surface functionalization strategies. *Nanoscale Research Letters*, 3: 397–415.
- Xiao, Y; Liang, H; Wang, Z. 2013. MnFe₂O₄/chitosan nanocomposites as a recyclable adsorbent for the removal of hexavalent chromium. *Materials Research Bulletin*, 48: 3910–3915.
- Xiong, J; He, Z; Mahmood, Q; Liu, D; Yang, X; Islam, E. 2008. Phosphate removal from solution using steel slag through magnetic separation. *Journal of Hazardous Materials*, 152: 211–215.

- Xu, Y; Rosa, A; Liu, X; Su, D. 2011. Characterization and use of functionalized carbon nanotubes for the adsorption of heavy metal anions. *New Carbon Materials*, 26: 57–62.
- Yang, X; Li, J; Wen, T; Ren, X; Huang, Y; Wang, X. 2013. Adsorption of naphthalene and its derivatives on magnetic graphene composites and the mechanism investigation. *Colloids and Surfaces A: Physicochemical and Engineering Aspects*, 422: 118–125.
- Yao, W; Shen, C; Lu, Y. 2013. Fe₃O₄@C@polyaniline trilaminar core–shell composite microspheres as separable adsorbent for organic dye. *Composites Science and Technology*, 87: 8–13.
- Yavuz, CT; Prakash, A; Mayo, JT; Colvin, VL. 2009. Magnetic separations: from steel plants to biotechnology. *Chemical Engineering Science*, 64: 2510–2521.
- Yeon, KH; Park, H; Lee, SH; Park, YM; Lee, SH; Iwamoto, M. 2008. Zirconium mesostructures immobilized in calcium alginate for phosphate removal. *Korean Journal of Chemical Engineering*, 25: 1040–1046.
- Yoon, SY; Lee, CG; Park, JA; Kim, JH; Kim, SB; Lee, SH; Choi, JW. 2014. Kinetic, equilibrium and thermodynamic studies for phosphate adsorption to magnetic iron oxide nanoparticles. *Chemical Engineering Journal*, 236: 341–347.
- Zeng, S; Cao, Y; Sang, W; Li, T; Gan, N; Zheng, L. 2012. Enrichment of polychlorinated biphenyls from aqueous solutions using Fe₃O₄ grafted multiwalled carbon nanotubes with poly dimethyl diallyl ammonium chloride. *International Journal of Molecular Sciences*, 13: 6382–6398.
- Zhang, B; Zhang, H; Li, X; Lei, X; Li, C; Yin, D; Fan, X; Zhang, Q. 2013. Synthesis of BSA/Fe₃O₄ magnetic composite microspheres for adsorption of antibiotics. *Materials Science and Engineering C*, 33: 4401–4408.
- Zhang, L; Liu, N; Yang, L; Lin, Q. 2009. Sorption behavior of nano-TiO₂ for the removal of selenium ions from aqueous solution. *Journal of Hazardous Materials*, 170: 1197–1203.
- Zhang, L; Wu, D; Zhu, B; Yang, Y; Wang, L. 2011. Adsorption and selective separation of neodymium with magnetic alginate microcapsules containing the extractant 2-ethylhexyl phosphonic acid mono-2-ethylhexyl ester. *Journal of Chemical and Engineering Data*, 56: 2280–2289.

- Zhang, N; Lin, LS; Gang, D. 2008. Adsorptive selenite removal from water using iron-coated GAC adsorbents. *Water Research*, 42: 3809–3816.
- Zheng, S; Chen, J; Jiang, X; Li, X. 2011. A comprehensive assessment on commercially-available standard anion resins for tertiary treatment of municipal wastewater. *Chemical Engineering Journal*, 169: 194–199.
- Zhitkovich, A. 2011. Chromium in drinking water: sources, metabolism, and cancer risks. *Chemical Research in Toxicology*, 24: 1617–1629.
- Zhu, HY; Jiang, R; Xiao, L; Zeng, GM. 2010. Preparation, characterization, adsorption kinetics and thermodynamics of novel magnetic chitosan enwrapping nanosized $\gamma\text{-Fe}_2\text{O}_3$ and multi-walled carbon nanotubes with enhanced adsorption properties for methyl orange. *Bioresource Technology*, 101: 5063–5069.

NOMENCLATURE

BE	binding energy
BET	Brunauer-Emmett-Teller
BJH	Barrett-Joyner-Halenda
BTEX	benzene toluene ethylbenzene xylene
CNTs	carbon nanotubes
DLS	dynamic light scattering
DMSO	dimethyl sulfoxide
EDS	energy dispersive x-ray spectrometry
ESCA	electron spectroscopy for chemical analysis
FTIR	fourier transform infrared
FWHM	full width at half maximum
HGMS	high-gradient magnetic separation
HK	Horvath-Kawazoe
ICP-AES	inductively coupled plasma-atomic emission spectroscopy
JCPDS	joint committee on powder diffraction standards
LDHs	layered double hydroxides
MOE	korean ministry of environment
MWCNTs	multi-walled carbon nanotubes
NF	nanofiltration
NNI	national nanotechnology initiative
POU	point-of-use
PTFE	polytetrafluoroethylene
RO	reverse osmosis
RSC	royal society of chemistry
SEM	scanning electron microscopy
SWCNTs	single-walled carbon nanotubes
TEM	transmission electron microscopy
US EPA	united states environmental protection agency
VSM	vibrating sample magnetometer
WHO	world health organization
XPS	x-ray photoelectron spectroscopy
XRD	x-ray diffractometer
XRF	x-ray fluorescence spectrometer
ZVI	zero valence iron

국 문 초 록

본 논문에서는 자성 복합체를 합성하여 특성을 분석해 보았으며, 흡착제로써 수중 셀레늄, 크롬, 비소 및 인 제거에 적용해 보았다. 본 연구에서 제시하는 자성 복합체에는 탄소 나노튜브/산화철 자성 나노복합체와 자성 알긴산-층상이중수산화물 복합체를 포함한다.

탄소 나노튜브/산화철 자성 나노복합체는 탄소 나노튜브 표면에 산화철 나노입자를 화학적으로 공침하여 제조하였다. 합성된 자성 나노 복합체를 주사전자현미경(SEM), 투과전자현미경(TEM), 질소 흡·탈착, 푸리에 변환 적외선분광기(FIR), 영전위점(pH_{PZC}), 에너지 분산형 X-선 분광기(EDS), X-선 회절 분석기(XRD), X-선 광전자 분석기(XPS), 그리고 진동 시료 자력계(VSM)와 같은 다양한 분석 기술을 통해 분석해 보았다. 나노 복합체에 의한 오염물질 제거는 회분 실험과 전량 여과 실험을 통해 확인하였다. 흡착 특성은 동역학 모델과 평형 모델, 그리고 열역학적 분석을 이용하여 분석하고 정량화 하였다.

분석 결과 산화된 탄소 나노튜브 표면에 나노 크기의 산화철 입자가 6에서 17 nm 범위로 균일하게 성장해 있는 것으로 나타났다. XRD 피크는 산화철 나노입자가 입방형 산화철 형태인 자석철과 침철석임을 나타냈다. 자성 나노복합체는 38.37 emu/g의 포화 자력과 15.66 Oe의 보자력을 가지고 있으며, 영구 자석에 의해 쉽게 분리될 수 있다.

주어진 실험 조건(함유량 = 1g/L, 초기 농도 = 10 mg/L, 반응 시간 = 4 h, 온도 = 30° C)에서 탄소 나노튜브/산화철 자성 나노 복합체의 흡착 용량은 비산염 9.55 mg/g, 아셀렌산염 8.12 mg/g,

아비산염 7.10 mg/g, 크롬산염 5.93 mg/g, 그리고 셀렌산염 3.82 mg/g 순으로 감소했다. 분석 결과 유사 2차 모델이 동역학 실험 설명에 최적인 것으로 나타났다. 평형 실험의 경우, 프로인드리히 등온식과 레들리히-피터슨 등온식이 잘 맞았다. XPS 분석 결과 셀렌산염과 아셀렌산염은 자성 복합체 표면에서 철의 산화와 함께 환원되는 것으로 나타났다. 연속 추출 실험은 57.8%의 크롬(VI)이 철산화물 부분(F3)에 존재함을 보였다. 비산염은 흡착 여과 공정에서 자성 복합체에 의해 효과적으로 제거되었다.

자성 알기산-층상이중수산화물 복합체는 분말 형태의 하소된 마그네슘-알루미늄 층상이중수산화물(LDH)과 자성 산화철을 알긴산하이드로겔로 포획하여 제조하였다. 자성 복합체는 1.5 ± 0.1 mm의 입자 크기를 가지며 외부 자기장에 따라 자성 특성을 나타내었다. 자성 복합체(2% 자성 산화철과 6% 하소 마그네슘-알루미늄 층상이중수산화물)의 흡착 용량은 주어진 조건(흡착제 함유량 = 3.0 mL 용액에 0.05 g, 초기 농도 = 10 mg/L, 반응 시간 = 24 h)에서 인산염에 대해 4.99 mg/g 그리고 크롬산염에 대해 1.61 mg/g이었다. 자성 복합체는 자력 분리에 의해 재사용 될 수 있다.

본 연구를 통해 자성 복합체가 수중 셀레늄, 크롬, 비소, 그리고 인 제거에 효과적인 것으로 밝혀졌다. 이러한 결과로부터 본 연구에서 개발된 자성 복합체가 첨단 수처리 시스템에 적용될 수 있을 것으로 보여진다.

주요어 : 흡착제, 비소 제거, 탄소 나노튜브, 크롬 제거, 산화철 나노입자, 층상 이중 수산화물, 자성 복합체, 인 제거, 셀레늄 제거

학 번 : 2008-30335